Kanak P. S. Parmar

Oil dispersions of nano-layered silicates in an external electric field: An experimental study

Thesis for the degree doctor philosophiae

Trondheim, November 2006

Norwegian University of Science and Technology
Faculty of Natural Sciences and Technology
Department of Physics

NTNU
Innovation and Creativity

NTNU
Norwegian University of Science and Technology

Thesis for the degree doctor philosophiae

Faculty of Natural Sciences and Technology
Department of Physics

ISBN 82-471-8215-7 (printed version)
ISBN 82-471-8214-9 (electronic version)
ISSN 1503-8181

Doctoral theses at NTNU, 2006:218

Printed by NTNU-trykk

Papers included in this thesis:

Paper 1:- J.O. Fossum, Y. Méheust, K.P.S. Parmar, K.D. Knudsen, K.J. Måløy and D. M. Fonseca, "*Intercalation-enhanced electric polarization and chain formation of nano- layered particles*",
Europhys. Lett. **74** (3), pp. 438-444 (***2006***).

Paper 2:- K.P.S. Parmar, Y. Méheust, J.O. Fossum, K.D. Knudsen and D.M. Fonseca, "*The porous space inside bundles of polarized phyllo-silicate crystallites – A SAXS study*",
Submitted to J. Appl. Cryst.

Paper 3:- K.P.S. Parmar, Y. Méheust and J.O. Fossum, K.D. Knudsen and D.M. Fo-nseca, "*Packing and voids in electro-rheological structures of polarized clay particles*",
Submitted to J. App. Phys.

Paper 4:- K.P.S. Parmar, Y. Méheust and J.O. Fossum, "*Electrorheological suspensions of laponite in oil: rheometry studies under steady shear*",
Submitted to Langmuir.

Paper 5:- K.P.S. Parmar, Y. Méheust and J.O. Fossum, **"***Electrorheology of synthetic Na-Fluorohectorite clay particles suspended in oil: rheometry studies under steady shear***",**
Manuscript to be submitted.

Paper 6:- D.M. Fonseca, Y. Méheust, J.O. Fossum, K.D. Knudsen, K.J. Måløy and K. P.S. Parmar, "*Nematic ordering of platelet-shaped nanosilicate colloids in saline solu-tions*",
Submitted to J. Appl. Cryst.

Other manuscript by author not included in this thesis:

Paper 7:- Y. Méheust, K.P.S. Parmar and J.O. Fossum, "*Orientational distribution of nano-layered clay particles inside electrorheological chains: a WAXS study*",
Manuscript to be submitted.

Acknowledgements

First, I would like to thank my advisor Professor Jon Otto Fossum, who became like a good friend over the past four years and introduced me to soft and complex matter, and in particular to the world of clay mineral systems. I am forever in his debt for giving me access to his time and to all the resources within his laboratories. I would like to thank Dr. Yves Méheust for all of his advice and help, in particular for his invaluable contributions to the X-ray data analysis appropriate for our systems, for his help in writing papers, and for discussing the true means of clay mineral systems during my early development work. I am deeply grateful to Mr. D. M. Fonseca who stood by my side countless times, helping during the synchrotron experiments. I would also like to thank Professor Kenneth Dahl Knudsen who has a large impact on my work due to his scattering expertise. Also, I would like to thank the staff people at the SNBL and DUBBLE beamlines at ESRF for their help during the synchrotron X-ray experiments.

Secondly, I would like to thank all of the graduate and postdoctoral students that worked alongside me for their help in numerous situations where I just didn't have the technical expertise to go the distance alone.

Finally, I would like to thank my sweet wife Amita and my parents for their moral support during my four year of research work.

Kanak P.S. Pamar
Trondheim, Norway
August; 2006

List of Abbreviations and Symbols

q	Magnitude of scattering vector
λ	Wavelength of X-ray radiation
2θ	Scattering angle
η	Viscosity of suspensions or fluids
η_0	Viscosity of suspending medium
e^-	Unit electronic charge
Å	Angstrom
τ	Shear stress
τ_0	Yield stress
l	Size of aggregates
φ	Azimuthal angle
$\Phi;\ \Phi_{max}$	Volume fraction of particles
a	Size of spherical particles
$D;\ D_m;\ D_s$	Fractal dimensions of aggregated particles i.e. a positive non integer
d_{hkl}	Spacing between [*hkl*] crystalline planes
η_{pl}	Plastic or high shear rate viscosity
$\dot{\gamma}$	Shear rate
d_{001}	First Bragg position
^0C	Degree centigrade
E	Magnitude of an electric field
kV	Kilovolts
$I(q)$	Scattered X-ray Intensity
$P(q)$	Form Factor
$S(q)$	Structure Factor
mPa	Milli pascal
mPas	Milli pascal second
μm	Micrometer
nm	Nanometer
mm	Millimeter
ml	Milliliter
CSS	Control shear stress
DTA	Differential thermal analysis
EG	Ethylene glycol
EXAFS	Extend3ed X-ray absorption fine spectroscopy
HRTEM	High-resolution transmission electron microscopy
IRS	Infrared spectroscopy
SAXS	Small angle X-ray scattering
SANS	Small angle neutron scattering
SEM	Scanning electron microscopy

TEM	Transmission electron microscopy
WAXS	Wide angle X-ray scattering

List of Figures

Abstract

The work in this thesis concerned with the experimental study of structural morphologies and rheological properties of chains and/or- column like-structures of electrorheological (ER) fluids of 2:1 synthetic nano-layered silicate clay minerals, whose particles are polydisperse (lateral size~ few nm to a few μm and longitudinal size~ 1 nm to 0.1 μm). The structural morphology of chains and/-or column like structures were mapped out by two different types of Synchrotron X-ray scattering experiments namely, Wide Angle X-ray Scattering (WAXS) and Small Angle X-ray scattering (SAXS). The rheological properties of ER fluids are measured using a Physica MCR 300 rotational rheometer equipped with co-axial cylindrical geometry.

Novel synchrotron wide angle X-ray scattering (WAXS) experiments presented here, show that individual clay particle (stack of nano-layered clay platelets) polarize along its lateral direction indicating that intercalated or attached ions or water molecules play a role in its electric polarization. The preferred orientational distribution of polarized clay particles along the direction of applied electric field and characteristic shape of their orientational distribution functions is found to depend on the nature of intercalated cations and are well described by a Gaussian function and more accurately by means of a Mayer-Saupe function of the type that is generally used to described nematic liquid crystalline ordering. Further, a small increases (~0.05 Å) in distance between the nano-layered clay platelets were observed in an applied electric field (~1 kV/mm).

Small Angle X-Ray scattering (SAXS) experiments show the porous nature of the clay particles assembly inside the chains and/-or column like-structures. The anisotropic SAXS patterns were analyzed in terms of their iso-intensity lines and one dimensional profiles have been computed along their principal directions. Along the principal directions, power law behaviors are observed with crossovers corresponding to the average particle thickness and to typical pore sizes. The exponents of power laws indicated the dominating role of surface scattering of clay particles and provides pictures of their assembly inside the chains and/-or columns like-structures, consistent with configurations inferred from WAXS experiments.

Rheological measurements on ER fluids of dehydrated polydisperse smectites particles show that the induced polarizations of smectites clay particles in applied electric fields (dc) are controlled by their conductivity mismatch to that of suspending liquid (silicone oil), thus confirming that migration of surface charge on the clay particles surface and possible movement of intercalated cations play a major role in their polarizations in external electric fields, consistent with the results of the WAXS experiments. In absence of external electric fields, the steady state shear behaviors of ER fluids are Newtonian-fluid and in presence of external electric fields (~kV/mm) the behavior becomes Bingham-like solid. The dynamic yield stresses of these ER fluids (Bingham-like solids) and static yield stress of undisrupted ER fluids are drastically affected by the magnitude of applied electric field and the volume fraction of the investigated clay particles.

Contents

1. Overview

Soft matter systems [1-2] have complex structural and dynamic properties intermediate between those of crystals and fluids. Examples of soft matter systems are liquid crystals, with their well-known orientational order; colloids; polymer solutions; foams and gels etc. Among these, colloids play a prominent role as they can be both prepared and characterized in a controlled way and moreover they can be regarded as the simplest prototype of soft matter systems: the length scale separation between the molecular solvent and the mesoscopic particles is unique and complete.

The effective interactions between the colloidal particles can be tailored and controlled in presence of external stimuli such as by changing the salt concentration in the solvent, or applying external fields [1-2]. Such fields can be a shear flow, electric- and magnetic- as well as laser optical- fields and topographical fields such as confining geometry. Many physical aspects of colloidal soft matter systems are currently well mapped out and well understood [1-2] but important questions in external fields and additional confining geometries remain to be understood. Exciting questions concern collective many-body effects induced by cooperation and self-organization of many particles. A striking advantage of colloidal dispersions lies in the fact that these questions can be studied simultaneously by using different complementary methods: experiment, simulation, and theory.

The motivation of present thesis is to study Electro Rheological (ER) fluids of nano-layered clay particles in an external dc electric field that can induce qualitatively novel effects into their structural and dynamic properties. ER fluids [42-49] are colloidal suspensions consisting high dielectric or conductive particles in a non-conducting liquid, whose flow can be completely jammed and the suspensions can become solid-like in presence of dc or ac external electric fields. This jamming occurs due to fast aggregation of electrically polarized particles into chains-or-columns like structures in the suspension.

In this thesis work, an experimental study has been carried out on the structural- and rheological- behavior of ER fluids of synthetic 2:1 phyllosilicates (smectites) clay mineral particles in an applied dc external electric field (~kV/mm). Direct observations of the dynamics of structural formation in ER fluids have been observed in an optical microscope. The structural morphology of chains-or-columns like structures have been mapped out by using synchrotron X-ray scattering experiments, directly providing information about size and shape distributions, orientational and spatial ordering, and dynamics of the population of smectite particles. In addition, rheological properties i.e. viscosity, shear stress, yield stress etc. of various concentrations of ER fluids were investigated by shear-rheological experiments.

1.1. Organization of the introductory section

The first part of the thesis gives a very brief introduction to the field. The necessary scientific background is presented in Sec.2. The physical and chemical

characteristic of the crystal structure of most relevant clay minerals used to prepare ER fluids are given. A general background of X-ray scattering theories is introduced, and the valuable information obtained from these techniques is described. The rheological behavior of clay mineral suspensions is introduced, and possible theoretical models are summarized. A general introduction to the electrorheological fluids is presented, and some of the most relevant theories and models of particle polarization and particle-particle interactions in external electric field are introduced.

In Sec.3 experiments are summarized, the materials used to prepare the ER fluids and experimental techniques X-ray scattering and rheology are described. Finally, Sec.4 contains an introduction to the papers included in this thesis.

2. Scientific Background

We are very much familiar with the name “clay” and in common terms it is a group of fine-grained silicate minerals i.e. with a particle size (smaller than 2 μm). In the simplest terms, the silicate minerals can be considered made of two basic structural units which are the tetrahedral and the octahedral layers respectively. Many of the silicate minerals can be pictured as the configurations made by joining such tetrahedral and octahedral layers to themselves and to each other in three dimensions [3-4].

Clay minerals [3-9] are phyllosilicates or sheet silicates or layered silicates, whose primary particles are platelet shape. Each clay platelet is ~1 *nm* thick (c-direction) and its lateral size (a- and- b direction) can vary from few tenths of *nm* up to ~ a few μm. Thus clay platelets are in general highly anisotropic in their shape and polydisperse in their size. The “unit cell” structure of a single clay platelet is made of tetrahedral sheets and octahedral sheets joining face-to-face configuration in three dimensions respectively. The ratio of tetrahedral sheets to octahedral sheets in the structural representation of unit cell divide clay minerals into group [6-9] of 1:1 clay minerals such as kaolinite, serpentine, halloysite etc. and 2:1 clay minerals such as montmorillonite, vermiculite, illite, laponite, hectorite etc. In this thesis mostly 2:1 clay minerals have been studied.

The crystal structure of a 2:1 clay platelet consists of an octahedral sheet sandwiched between two inverted silicate tetrahedral sheets as illustrated in Figure 1. A 2:1 clay mineral is classified as di-octahedral when two thirds of the octahedral sites are occupied by cations in its unit cell, whereas if all the octahedral sites are filled with cations it is classified as tri-octahedral [6-9]. The isomorphic substitution by low charge cations species, primary in the octahedral sheet and too a less extent into the tetrahedral sheet, creates a permanent negative surface or layer charge on a clay platelet structure which is why clay particles form stacks with charge balancing cations between their interlayer space, thus clay particles are often called “nano-layered silicates”. The longitudinal distance between two adjacent clay platelets in a “crystalline grain” is known as the basal spacing (d_{001}), a characteristic property of each type of clay mineral [7-9]. Also, a clay platelet always carries a small positive charge on their edges due to "unsatisfied" broken bonds due to finite growth of the clay platelet crystal structure. The edge charge of

platelets is pH dependent of a solvent in which they are dispersed. The overall magnitude of platelets surface charge divides 2:1 clay minerals into groups of talc-pyrophillite, smectite, vermiculite, mica and brittle mica [6-9]. The members of each group are distinguished by the type and location, of cations in the tetrahedral- and octahedral- sheets respectively [8-9].

Particles of smectites are "crystalline grains" which are stacks of several clay platelets residing on top of each other with intercalated charge balancing cations. Smectite clay platelets have a moderate charge density varying from 0.4 e^- to 1.2 e^- per unit cell [6-10] compared to other 2.1 clay minerals. The moderate surface charge on the smectite clay platelets allows the exchange of intercalated cation with other cations, and this exchange is measured with quantity called cation exchange capacity (CEC) which is define as a quantity of positively charged ions (cations) that can accommodate on its negatively charged surface and expressed as milliequivalent (meq) per 100 g of clay [4, 7, 25]. Further, such a moderate surface charge also allow the penetration of water- or other polar- molecules in the interlayer space between platelet, thus causing smectites grains to swell. In the dry state, smectite clay particles are aggregates of several "crystalline grains" joined edge-to-face-edge configurations as illustrated in Figure 1.2, but when grains are exposed to humid conditions or also in vapors of ethylene glycol (EG), the basal spacing (d_{001}) increases between the adjacent platelets. The EG swelling is a standard test to identify the smectites in a mixture of clay minerals [7-9, 11].

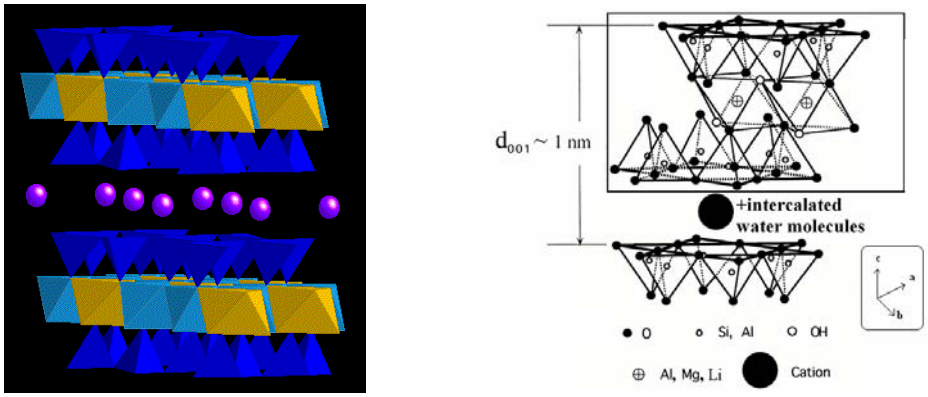

(a) **(b)**

Figure 1.1:- Three dimensional crystal Structure of a 2:1 Phyllosilicate clay. **(a):** Platelets (thickness ~1 *nm*) are formed by an octahedral sheet sandwiched between two tetrahedral sheets with intercalated charge-balancing cations. **(b):** Structural units of smectites (platelets of thickness ~1 *nm*) are held together in longitudinal direction (c-direction). In smectites the amount of water or other polar molecules changes the c-dimension (d_{001} i.e., the basal spacing) which can vary from ~1 *nm* (dry state) to infinite [8-9].

The natural clay montmorillonite is the most familiar and common member of the smectite group. It is a di-octahedral smectite with general chemical formula, $M_y^+ .nH_2O\ (Al_{4-y}\ Mg_y)\ Si_8O_{20}\ (OH)_4$, where M (M = Na^+, Ca^{2+}, Mg^{2+}, etc) is the charge balancing interlayer cation. Besides the interlayer cations, the interlayer space of montmorillonite can absorb large amounts of water vapor 0- up to ~ 4 water layers in successive steps, thus changing the basal spacing (c-direction) from ~1 *nm* to 2.14 *nm* [12]. In the tri-octahedral smectite group, hectorite with a general chemical formula $M_y^+ .nH_2O\ (Li_y\ Mg_{6-y})\ Si_8O_{20}(OH)_4$, is the most common clay mineral, in which some fraction of Mg^{2+} has been replaced by Li^+ in the octahedral sheet only. The fraction y of Li^+ determines the overall layer charge of hectorite. Laponite is a synthetic tri-octahedric smectite with well- defined "crystalline grains", stacks of relatively monodisperse platelets (a single laponite platelet is a disc of thickness~1 *nm*, diameter~30 *nm*) with intercalated Na^+ as a charge balancing cation [10]. If all the OH^- groups of synthetic hectorite clay are replaced by Fluorine (F^-) ions the clay is called Fluorohectorite [10, 13-14]. This clay represents an extreme in layer charge (1.2 e^- /unit cell) within the smectite group and can absorb 0-to-3 water layer in successive steps, in its interlayer space depending on the environmental temperature or humidity conditions [13-14]. Due to this very high surface charge "crystalline grains" of fluorohectorite contains on average about 80~100 platelets [13]. In general the size of smectites clay minerals grains range from few *nm* upto a few μm, depending upon how their platelets structures are chemically synthesized.

Depending on the surface charge density of platelets, crystalline grain of smectites suspended in a good solvent liquid (i.e., distilled water) can take a large amount of solvent molecules between the interlayer spaces of platelets or even the platelets can be fully separate i.e. basal spacing goes to infinite for example in laponite clay that represents the lowest layer charge density (0.4 e^- per unit cell) in smectite group [4, 10]. On the other hand the fluorohectorite clay that represents the highest layer charge density (1.2 e^- per unit cell) its platelets remains staked in its crystalline grains even if this clay is fully suspended in a good solvent like distilled water [12-13]

Thus smectite suspensions can shows different structural and dynamical properties depending on the length scale of observation. Depending on the characteristic features and desired resolution of the structural study, different characterization techniques [4, 7-9, 25] such as HRTEM, SEM, DTA, WAXS, IRS and EXAFS may be used to obtain structural information at an atomic resolution. If the relevant structural features are at a subatomic level from a few tenths up to about 100 nm, SAXS and SANS are the most widely used techniques [15-17]. These techniques provide statistical and overall information averaged in a volume of the order of 1 mm^3. Very local structural analysis can in many cases be performed by TEM technique which is a useful complement for scattering investigations.

2.1. X-Ray Scattering Technique:-

The Bragg law of X-ray diffraction or scattering [8-9, 19] provides information about the crystalline nature (periodic arrangement of atoms or ions) and amorphous

or disordered nature (non-periodic arrangement of atoms or ions), of materials. In the case of elastic scattering, the scattered intensity, *I(q)*, from a material is experimentally often described in terms of the scattering vector, *q*, whose magnitude is given by

$$q = \frac{4\pi}{\lambda} \sin\left(2\theta/2\right) \tag{1.1}$$

where λ is the wavelength of incident radiation, 2θ is the scattering angle (angle between the directions of the scattered and transmitted beams). For the constructive interference of scattered X-rays, the well known Bragg's law of scattering (as illustrated in Figure 1.3) is given as

$$2d_{hkl} \sin\left(2\theta/2\right) = n\lambda \tag{1.2}$$

where "d_{hkl}" is the spacing between any two [*hkl*] planes of the crystal. Bragg reflections can occur only for wavelengths $\lambda \leq 2d_{hkl}$. It is important to notice that the Bragg law is the consequence of the periodicity of the atoms of ions in a lattice. The Bragg law does not refer to the composition of the basis associated with every lattice points. This is purely geometrical law. However, the composition of the basis determines the relative intensity of the various order of diffraction (denoted by *n* in equation (1.2)) from the given set of parallel planes. The "d_{hkl}" values of any crystalline material are related to physical configuration of its entities i.e. atoms, ions or molecules that has made its physical structure. The various sets of planes [*hkl*] in three dimensions will have various spacing values "d_{hkl}".

For a three dimensional interplanar spacing "d_{hkl}", measured perpendicular to the planes is a function both of the plane indices [*hkl*] and the lattice constants [8-9]. The exact relation depends on the crystal system involved.
Comparing equations (1.1) and (1.2) one gets

$$q_{hkl} = \frac{2\pi}{d_{hkl}} \tag{1.3}$$

Through combined use of above equations, quickly and rapidly, it is possible to determine the spacing "d_{hkl}" between any two of the crystalline plane. The Bragg law is derived for certain ideal conditions and diffraction is only a special kind of scattering. A more precise definition used in optics distinguishes between scattering and diffraction: scattering generally implies interaction of waves (or photons) with spatially uncoordinated (unordered) atoms; diffraction on the other hand occurs when the object or part of the object is made up of ordered atoms. These atoms, being neatly arranged, "scatter" the waves or photons in a coordinated way (i.e., in specific direction(s)). A single atom scatters an incident beam of X-rays in all direction in space but a large number of atoms or ions arranged in a perfectly periodic lattice scatter (diffracts) X-ray in relatively few

directions. It is so precisely because the periodic arrangement of atoms or ions causes destructive interference of the scattered rays in all directions except those predicted by Bragg law, where constructive interference (reinforcement) occurs.

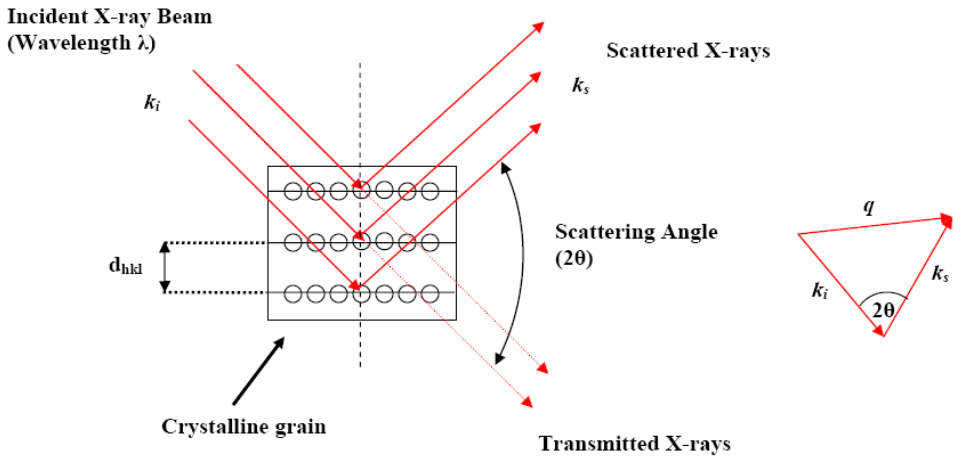

Figure 1.3:- Schematic representations of Bragg scattering from a particular family of lattice planes separated by distance d. $\boldsymbol{k_i}$ and $\boldsymbol{k_s}$ are the wave vector of incident and scattered rays and are shown only for neighboring planes. The path difference is $2d \sin(\theta)$.

If the crystal contains some imperfections, the measurable diffraction can occur at non-Bragg angles (i.e. the Bragg peaks are not delta-functions anymore) because the crystal imperfection results in the partial absence of one or more conditions necessary for perfect destructive interference at these angles. These imperfection are generally slight compared to the over-all regularity of the lattice which cause that the diffracted beams are confined to very narrow angular ranges centered on the angles predicted by the Bragg law for ideal condition resulting in line broadening.

The relation between constructive interference and structural periodicity can be well illustrated by a comparison of X-ray scattering by crystalline solids, liquids and gases (Figure 1.4). The curve of scattered intensity $I(q)$ vs. 2θ for crystalline solid is nearly zero everywhere except at certain angle where sharp maxima occur - diffracted beams. Both amorphous solids and liquids have structures characterized by an almost complete lack of periodicity and tendency to order in the sense that the atoms or ions are fairly tightly packed together. The atoms in amorphous structure show just statistical preference for a particular interatomic distance; resulting X-ray diffractogram exhibits only one or two broad maxima. But in gases there is no periodicity and the atoms are arranged perfectly random and their relative positions change all the time. The corresponding scattering curve shows no maxima just a regular decrease of intensity with increasing scattering angle.

2.1.1. X-ray Powder Diffraction:-

The powder diffraction method of X-ray diffraction [8-9, 19] is one of the most useful of all diffraction methods, which can yield a great deal of structural information about the material under investigation. Essentially the method employs the diffraction of monochromatic X-rays by a powder specimen. "Powder" can mean either real powder bound together or any specimen in polycrystalline form. This is a great advantage as the polycrystalline materials can be examined without special preparation. In powder sample or fine polycrystalline sample, there are many small crystallites randomly oriented so there are always some crystals with planes favorably oriented to yield the diffraction in particular angle determined by the Bragg condition (equation 1.2). By scanning the sample in wide angle different planes of different crystals will satisfy the reflection condition and the diffraction pattern or lines (peaks) will occurs and can be recorded.

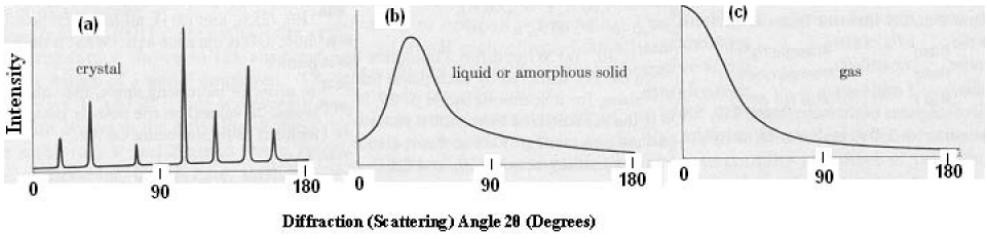

Figure 1.4: Comparison of X-ray scattering curve for crystalline, amorphous structure and gas (schematic). The vertical scales are different and such curves are called diffractogram.

The diffracted intensity as a function of the measuring angle 2θ is called a diffractogram as illustrated Figure 1.4. The method assumes that the amount of the crystallites is large and truly randomly oriented. If not, i.e. the sample has some kind of preferred orientation or the crystalline grains are large, the observed intensity of the diffraction lines may radically differ from the calculated one. It is relatively easy to prepare powder specimens where ideal perfect randomness is closely approached but virtually all solid polycrystalline materials either produced or natural will exhibit some preferred orientation of the grains. The shape and size of the unit cell determines the angular position of the diffraction lines [8-9]. The arrangement of the atoms within the unit cell determines the relative intensity of the lines (via structural factor, f). Since the structure determines the diffraction pattern, it should be possible to go in the other direction and deduce the structure from the diffraction pattern. However, there is not any direct way to achieve this. Given a structure, the diffraction pattern can be calculated, but the reverse problem, directly calculating the structure from the experimental diffraction pattern is in general impossible because the phase transformation factor is not precisely known.

Any calculation of the intensity of diffraction must begin with the structure factor $|f|^2$ that is proportional to the square of the number of electrons n_e^2 in an atom

at low scattering angles i.e. $q \rightarrow 0$. The rest of the calculation varies with the diffraction method involved. There are six factors affecting the relative intensity of the diffraction lines in a powder pattern: The (1) Structure factor, (2) Lorenz Polarization factor, (3) Absorption factor, (4) Temperature factor, and (5) Multiplicity factor.

The Lorenz Polarization factor is combination of two geometrical factors: 1) the polarization factor connected with the elastic scattering of X-ray by a single electron and the polarization of the incident X-ray radiation and 2) the Lorenz factor, a particular trigonometric factor influencing the intensity of the reflected beam for various diffraction angles. This factor accounts for the fact that crystallites can still diffract strongly at angles that diverge from the Bragg angle [8-9].

The diffracted intensity is also affected by the absorption factor i.e., absorption in the specimen itself. The temperature factor is due to fact that the atoms are not fixed in particular points but undergo the thermal vibration about that points. This is true even for absolute zero temperature, and the amplitude of the vibration increases as the temperature increases. This leads to decrease of the amplitude of the diffraction lines with increasing temperature. This factor also depends on the diffraction angle. The multiplicity factor is connected with the fact that there are different planes with the same spacing. Since all the planes have the same spacing, the beams diffracted by all of them form the part of the same line. This relative proportion of planes contributing to the same reflection enters the intensity calculation. The multiplicity factor m can be defined as the number of different planes having the same spacing.

Taking into account all above-mentioned factors the relative intensity $I(\theta)$ of the powder pattern line in diffractogram is given by

$$I(\theta) \approx |f|^2 \, m \left(\frac{1-\cos^2 2\theta}{\sin^2 \theta \cos \theta} \right) \exp(-2M) \qquad (1.4)$$

where the term in brackets is the combined Lorenz-polarization term, and exp(-2M) is lattice vibration factor also known as the "Debye-Waller factor". The absorption factor has not been included in this equation. For the comparison of the intensity of the adjacent (neighboring) lines on the pattern at the same temperature, the scattering angle dependence of the temperature factor can be neglected due to weak q dependence.

The most common use of Bragg X-ray diffraction is to measure crystalline and amorphous structures on the atomic scale, but clearly, many morphologies are of importance that has characteristic sizes much larger than the atomic scale. The Bragg's law predicts that information pertaining to such nano- to colloidal-scale structures would be seen below scattering angle $2\theta < 6°$ in the diffractogram. Depending upon the length scale of observation that corresponds to regimes of scattering angle 2θ, two kind of X-ray scattering can be distinguished as illustrated in Figure 1.5. A wide angle X-ray scattering (WAXS) corresponds to the scattering angle $2\theta > 6^0$ i.e. diffraction at small-scale structures and a small angle X-ray

scattering (SAXS) corresponds to the scattering angle $2\theta < 6^0$ i.e. diffraction at large-scale structures.

Atomic scale structures are often characterized either by high degree of order, i.e. crystals, or disorder as in molecular liquids or molecular glasses, and relatively simple and uniform building blocks, i.e. atoms or molecules. On the nano-scale, the building blocks of matter are rarely well organized and are composed of rather complex and non-uniform building blocks. Resulting feature in X-ray scattering or diffraction are thus sharp diffraction peaks from crystals in the XRD or WAXS range, and comparatively nondescript diffuse broad patterns in the SAXS *q*-range.

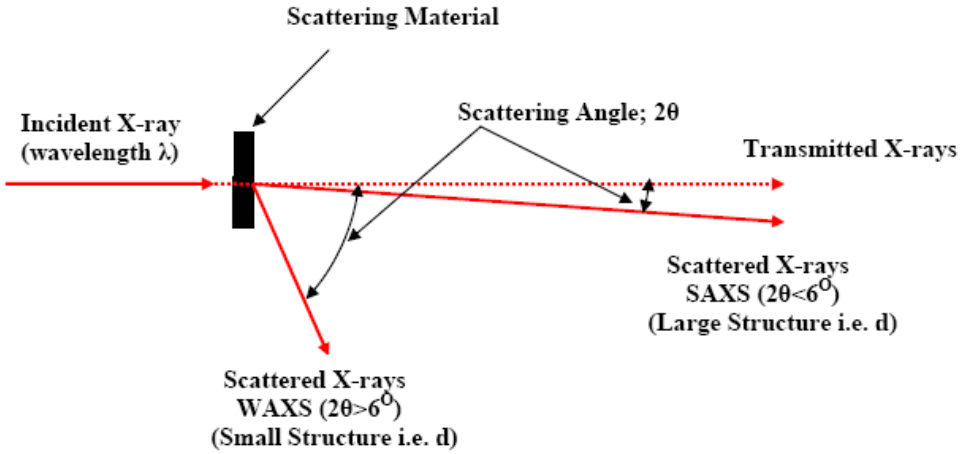

Figure 1.5:- Schematic representation of an X-ray scattering experiment. Based on scattering angle 2θ, two types of Bragg scattering can be define namely WAXS (scattering of small structures) and SAXS (scattering of large structures).

2.1.2. Wide Angle X-ray Scattering (WAXS):-

Wide angle X-ray scattering ($2\theta > 6^0$) is the most important tool for qualitative (individual clay minerals) and quantitative (mixed clay minerals) analysis of clay minerals (1:1 or 2:1). Due to the unique chemical composition of phyllosilicate minerals the qualitative analysis can be quickly done by checking the position of the Bragg peaks i.e. [*hkl*] reflections [7-9]. In the limit of zero *q*, the widths of Bragg peaks are inversely proportional to the number of unit cells which is a finite number for a clay size particle and hence the finite width of Bragg peaks (see Figure 1.4) will corresponds roughly to the average crystalline size [7-9]. The broadening of the peaks can be considered mainly to be due to the size or thickness of entire clay particle [8-9], and possible lattice strain or disorder of its interplanar lattice spacing (*d*), that generally lead to a *q*-dependence to the width of Bragg peaks [14].

Expanding clay minerals like smectites can easily be identified from a mixture of several clay minerals by solvation/adsorption of test of EG [7-11]. The shift in the Bragg peaks under dry/humid environment can be used to identify the coexistence

of a single type (integral 0, 1 and 2 etc.) of water layer [7-9, 12-14] and or random intercalation of water layers [18] in smectites. Further the position of Bragg peaks (030 and 060) can be used to distinguish di-octahedral or tri-octahedral nature of smectites [7-9].

Quantitative analysis of clay minerals through WAXS is more difficult to carry out than qualitative analysis as a very good sample preparation is needed [6-9, 17]. The reflections of mixed-layer clay minerals are usually found between those of the pure clay minerals. The location of the reflections reveals the ratio of the components [8-9]. For example ethylene glycol (EG) solvated illite/smectite interstratified minerals, the (001/002) reflection is located between the 1 *nm* reflection of illite and the ~1.6 *nm* reflection of the EG-smectite [8-9]. The location of the reflection of the mixed layer mineral permits an estimation of the illite/smectite ratio. An even more precise estimation is based on the difference in 2^0, 2θ between the (001)/(002) and (002)/(003) reflections, since the difference increases with increasing illite content.

2.1.3. Small Angle X-ray Scattering (SAXS):-

For small angle X-ray scattering ($2\theta<6^0$) the Lorenz-polarization factor (see equation 1.4) is ~1. For disordered systems the multiplicity factor is 1 and the structure factor often does not reflect any periodic order of atoms or ions in systems, so only a form factor $P(q)$ that depends on the size and shape of involving nano-scale structure contribute to the scattering, i.e. regions of differing electron density. For X-ray diffraction the atomic scattering factor $|f|^2$ is proportional to the square of the number of electrons in an atom at low scattering angles i.e. $q\rightarrow 0$. Additionally, the intensity of the scattering is proportional to the number of scattering elements in the scattering volume. In general, a scattered intensity in SAXS is controlled by the size and shape of nano-scale structures, their tendency to aggregate, the porosity of correlated aggregated nano-scale structures, the magnitude of their specific surface area, and more generally by the inhomogeneties characterizing the nano-scale structures of the systems [15-16, 21-25, 31-41].

The SAXS regime describes two main features that are observed in a log-log plot of scattered intensity *I(q)* versus *q* (see equation 1.5). First, typical scattering patterns display power-law decays in intensity reflecting power-law scaling features of many materials. Secondly, power-law decays begin and end at exponential regimes that appear as knees in a log-log plot. These exponential "knees" reflect a preferred Bragg condition resulting from a characteristics size of particles for the knee regime.

Many scattering patterns in the small-angle regime show a decay of intensity *I(q)* versus *q*. For a correlated system that might have some structure factor i.e. positional or orientational correlation between its nano-scale structures, the scattered intensity also given by the expression [15-16, 31-41]

$$I(q) \propto P(q)S(q) \approx q^{-D} \qquad (1.5)$$

where q is given by equation (1.1); the exponent D reflects the physical nature of structures for example their porous nature [31, 34, 37] or surface roughness [36, 40-41]; $P(q)$ is the form (or scattering) factor of particles which depends upon their size and shape and describes the scattered intensity function from a single primary particle; and $S(q)$ is the structure factor which account for the interaction between the particles i.e. spatial correlation between them. At very high q-values, for a very dilute systems of particles that only have short-range spatial correlation, $S(q)$ becomes unity over the whole q-range and the scattering intensity $I(q)$ (equation 1.5) then only depends on the quantity $P(q)$ which is known for many shapes such as spheres, thin platelet, rigid-rod etc.[20].

For porous media, the scattering profiles i.e. $I(q)$ versus q, often exhibit power laws on a wide q-range (equation 1.5) and have been observed in particular for aggregates of colloids [32-34] and various types of rocks [39-41]. Such power law scattering curves have been explained in terms of fractal properties of the scattering medium, from models in which aggregated particles (for example, ruguous spheres) form a porous medium with geometrical properties that relate to the concept of fractals.

Two kinds of fractals, mass fractals and surface fractals can be distinguished [21]. If we consider mass fractals, or more generally systems in which the aggregated particles are positioned at a distance R, with respect to one another, so that their two-point correlation function has the form

$$g(r) \propto R^{D_m - 3} \tag{1.6}$$

where D_m is a fractal dimension. For such correlation function a power law scattering profile (equation 1.5) with an exponent $D=D_m$ is observed for q-values in the range $1/l \leq q \leq 1/a$, here a is the typical size of an aggregated particle, and l is the size of the whole system, i.e., the largest length accessible length scale [35 40]. Since by definition D_m is in the range [1; 3], the exponent observed in the scattering data is in the range [−3; −1].

If we probe length scales smaller than the particle size a, the scattering becomes sensitive to the roughness of the aggregated particles. If this roughness qualifies the particle for being considered a surface fractal with a dimension D_s, or more generally if the area is a power law of the horizontal size with an exponent D_s on a given range of scales, then the scattering profiles exhibit a power law behavior with an exponent $-(6 - D_s)$ on that range of scales [21-22]. Here by definition D_s is in the range [2; 3], and the scattering curve exponent is in the range [− 4; −3], with the well-known Porod law limit −4 being reached for smooth particles [41].

So in conclusion, in systems of aggregated rough particles, two power law behaviors can be observed, one with an exponent between −4 and −3 at large q-values, and one with an exponent between −3 and −2 at intermediate q- values corresponding to length scales larger than the particle size. The scattering properties of porous media possessing long range correlations in their mass geometry or in the roughness of their pores are generally more difficult in the case of polydispersity of the aggregated particles, or, equivalently, a wide distribution for the pore sizes. In this case, an exponent $D < -3$ can arise both from surface

scattering form rough pore walls, or from bulk scattering from a porous medium with a wide pore size distribution [40].

2.2. Rheology:-

In many applications, clay minerals are suspended in an aqueous or a non-aqueous liquid [24-27]. These clay suspensions are very much sensitive to mechanical perturbations (such as shear) and shows a large number of internal degrees of freedom, weak interactions between the clay particles and a delicate balance between entropic and enthalpic contributions to equilibrium structures, that are sensitive to external boundary conditions [24-25]. Different descriptive modes of clay particle associations can occur in a good solvent (for example in distilled water, pH=7) such as face-to-face (F-F), edge-to-edge (EE), and edge-to-face (E-F) [4, 7, 25].

Rheological parameters (viscosity, shear stress, viscoelastic modulii etc.) of clay suspensions [26-27] measured under different equilibrium conditions may exhibit a variety of behaviors (Figure 1.6). *Newtonian* (constant viscosity) or *Non-Newtonian* (Shear-thickening [26-27] and Shear-thinning of viscosity) behavior is common to clay suspensions which may or may not have a yield stress (τ_y) i.e. a stress which must be exceeded to start the flow of that clay suspension [25-27].

To characterize the flow curves (shear stress vs. shear rate) of suspensions or fluids under equilibrium conditions, many phenomenological and empirical models can be used to fit the data [28-29]. There are several models explaining the flow behavior of suspensions or fluids over a certain limited value of shear rate. A power law model can be used to describe the flow behavior (shear thinning or shear thickening) of very dilute aqueous clay suspensions. Aqueous clay suspensions possessing relatively high clay concentration have been described traditionally in accordance to the *Bingham* theory of plastic flow. In an ideal *Bingham* model [28-29] the shear stress (τ) expression is given by equation

$$\tau = \tau_y + \eta_{pl}\,\dot{\gamma}; \quad \dot{\gamma} = 0 \text{ for } \tau < \tau_y \tag{1.7}$$

where (τ_y) is the *Bingham* dynamics yield stress and η_{pl} is the plastic viscosity approaches to solvent viscosity at very high shear rate value. The *Bingham* model assumes that a fluid is an *elastic* solid at low shear stress and a *Newtonian* fluid above τ_y. Other models have been considered in describing the rheological behavior of clay suspensions, such as the *Casson* model and the *Herschel-Bulkley* model [27-28]. In all these cases the suspension has an initial yield stress at low shear rates, and afterwards presents pseudoplastic or 'shear-thinning' type behavior at higher shear rates.

Various factors affect the flow behavior of clay suspensions. Naturally, the volume fraction of clay particles (Φ) will bring about an increase of all rheological properties. The rheological behavior of multiphase systems within the linear dilute region (Φ<0.05) is relatively well described [27]. For dilute suspensions of spherical particles or clay particles in *Newtonian* liquids, the *Einstein* model for relative viscosity can be used. Within the higher concentration range, where the particle

interaction must be taken into account, the *Einstein's* model can not be used, and higher order terms of particle volume fraction (Φ) must be taken into accounted. The theoretical relation for viscosity, η, of concentrated suspensions of monodisperse spherical particles in a Newtonian-liquid of viscosity η_0 are often approximated by the Batchelor [26-28] or Krieger-Dougherty [26-28] relations, which are

$$\eta = \eta_0 \left(1 - \frac{\Phi}{\Phi_{max}} \right)^{-2.5\ \Phi_{max}} \tag{1.8}$$

and

$$\eta = \eta_0 \left(1 + 2.5\ \Phi + 6.2\ \Phi^2 \right) \tag{1.9}$$

respectively. Here Φ_{max} is the maximum volume packing fraction of particles. These relations account for the interactions between the particles themselves and between particles and the surrounding liquid. This result from the observation that the source of the viscosity in a fluid is the energy dissipation and when colloidal particles in a shear field begin to rotate, further energy dissipation occurs and the viscosity increase, thus a colloidal suspension of rod-like or plate-like particles will have higher viscosity compared to the same volume fraction of spherical particles [28]. Due to the polydispersity in size, high anisotropy in shape and heterogeneous charge distribution of clay particles, the coefficients of expression (1.8) will have significantly different values for different regime of Φ, if used for aqueous or non-aqueous concentrated clay suspensions. Because of high surface charge and anisotropic particle shape, dispersions of clay show a very strong *non-Newtonian* rheological behavior [24-25].

One empirical equation which has been found to account for the viscosity of monodisperse and polydisperse sphere suspensions [68-69], in a range of particle fraction up to 50% is:

$$\eta = \eta_0 \left(1 + \frac{0.75}{\frac{\Phi_{max}}{\Phi} - 1} \right)^2 \tag{1.10}$$

The relations (1.8-1.10) can in general be used to describe the viscosity of moderately-concentrated colloidal suspensions of isotropic, monodisperse, and non-charged particles [23-25], although relation (1.10) has been found to be an appropriate description for concentrated suspensions of kaolinite clay (a 1:1 clay) [69], whose particles are anisotropic and polydisperse [4, 6-7].

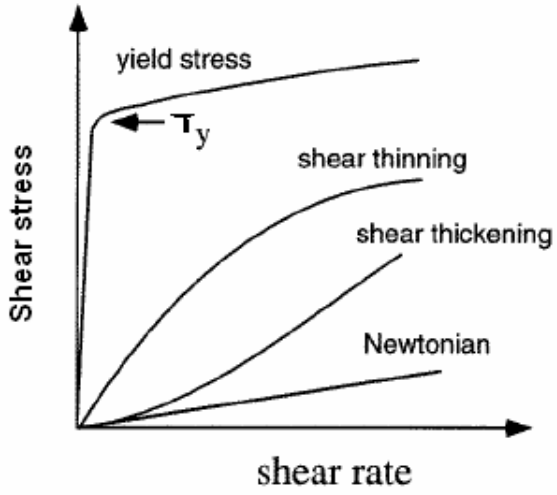

Figure 1.6:-- Identification of flow curves of fluids. The shear stress versus shear rate curves of fluids is the representation of their microstructures i.e. interactions between the particles. τ_y is the yield stress of fluids that's depends on its microstructure.

Some of the aqueous clay suspensions show thixotropy effects which means that their rheological properties depend on the time of shearing [24-27]. Furthermore, concentrated aqueous clay suspensions show a yield stress, i.e. below this stress they show infinite viscosities and beyond this stress they start to flow again. Recently the physical interpretation of the concept of yield stress was elaborated by Bonn et.al. [30]. Weakly flocculated aqueous suspensions of a bentonite (i.e. a natural clay) with particle concentration ~4%, and colloidal glasses of laponite clay at above 3% of particles concentration in distilled water, have been studied [30]. It has been shown that above a certain critical stress, these flocculated aqueous suspensions and gels (i.e. colloidal glasses) start flowing abruptly and subsequently accelerate leading to avalanches that are associated with a bifurcation in their rheological behavior. For small stresses below the yield stress, the viscosity of such flocculated aqueous suspensions and gels increases in time and they eventually stops flowing. For larger stresses slightly above the yield stress, the viscosity of flocculated aqueous suspensions and gels decreases continuously in time; the flow accelerates. Thus the viscosity jumps discontinuously to infinity at the critical yield stress. A simple physical model [30] was proposed to explain this avalanche effect based on the competition between the aging of particle microstructure (restructuring to its initial configurations) in flocculated aqueous suspensions or gels and a shear force (destruction of this microstructure), thus successfully explaining the experimental rheological results i.e. the viscosity bifurcation.

We have attempted the same experimental approach [30], to observe whether our ER fluids can show such a bifurcation behavior, with or without an applied electric field. We have found that it's not possible to observe such bifurcation phenomena [30] in our ER fluids due to experimental limitations: There may be several possible

causes for this, either related to the experimental geometry (see Sec.1.11), or related to the behavior of polarized particles (i.e., their orientations (see paper 1)) that form the chain or- column like-structures in few seconds (see paper 1 and paper 4). Experimental geometry: A slip of attached particles to the rotating cylinder may occur [30], as there is always an optimum value for matching the roughness of particles surfaces to that of rotating geometry. Polarized particles: structural "repair"-time is possibly much faster than the shear stress time-resolution of our instrument.

2.3. Electrorheology:-

The rheological properties (viscosity, shear stress, shear modulus etc.) of colloidal suspensions (high dielectric or conductive particles dispersed in low conductivity fluid) can be drastically modified in the presence of an external electric field of sufficient magnitude (~kV/mm). This kind of effect is known as the "ElectroRheological (ER) effect" and has been observed for several colloidal dispersions [42-49]. In a sufficient magnitude of applied electric field (~kV/mm), the colloidal particles acquire induced polarization and the interactions between polarized particles lead them to form chains-or-columns like structures between the two confining electrodes as illustrated in Figure 1.7. To maintain the flow, a shearing force (yield stress) is needed whose magnitude is roughly proportional to the square of the magnitude of applied field. This structuring occurs only when a sufficient electric field is applied, so this phenomenon is associated to the electrically induced forces between the dispersed particles.

In general, ER fluids are colloidal dispersions of polarizable (or conductive) particulate material in insulating liquids. The most attracting features of ER fluids are that their rheological properties (viscosity, yield stress, shear modulus, etc.) which can be reversibly altered by several orders of magnitude in presence of a moderate external electric field (~kV/mm). The rheological properties of ER fluids depend upon several experimental parameters such as the volume fraction of particles, the nature of the applied electric field (i.e. frequency (AC) and magnitude), the nature of the suspended particle (i.e. dielectric constant or conductivity, size and shape) and nature of liquid medium (viscosity, dielectric constant and conductivity). The other parameters which can make a significant contribution to ER effect are considerable amounts of additives absorbed by particles like surfactants or water or moisture. [50-53, 55-56]. Viscous and conductive heating of the ER fluid cause the eventual loss of water and result in a loss of ER activity on the electric fields [55]. Additionally, the presence of water leads to dielectric breakdown, corrosion and high power consumption for ER systems containing a substantial quantity of water [56].

As mechanical properties (yield stress) of ER fluids can be easily controlled within a wide range, almost from a pure liquid to a solid-like behavior, so an ER fluid could be used as an electric and mechanical interface. This property of ER fluids has stimulated a great deal of scientific interests both in academic and industrial areas. Based on the ER effect several possible industrial applications have been proposed. Examples includes clutches, brakes, damping devices,

actuators, fuel injection valves, hydraulic valves, bearing dampers, seismic damping frame structures etc. In addition, an ER fluid could also be used for a photonic crystal, light shutter, mechanical polisher, display, ink jet printer etc. [43-46].

In a shearing force, and at zero applied fields; ER Fluids usually behave like Newtonian fluids (constant viscosity and no preyield stress); whereas with in an applied field it is described by a well defined yield stress which must be exceed in order to start the flow. Beyond this yield stress ER Fluids tends to be shear thinning (i.e. the viscosity decreases) as the shear rate increases [58]. The typical behavior of an ER fluid under the influence of external electric field (E) is that of a *Bingham-like* fluid (equation (1.7)) for which the plastic viscosity η_{pl} now depends on magnitude of the applied electric field and the shear rate [58].

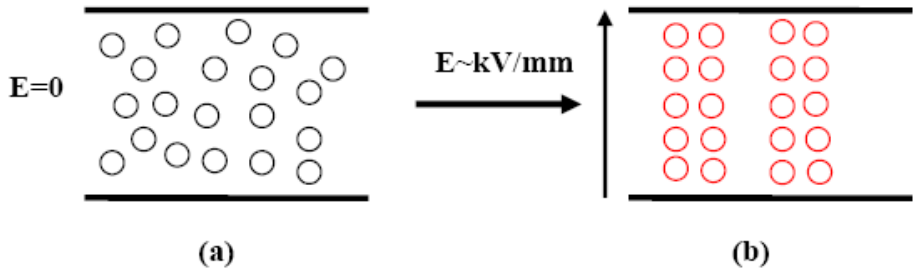

Figure 1.7:- Schematic illustration of an electrorheological effect between the electrodes (two parallel dark lines) **(a):** randomly dispersed particles, E ~ 0 **(b):** Chains-or-columns like structures of particles, E ~ kV/mm.

When increasing the magnitude of an external electric field the yield stress of ER Fluids increases dramatically while the plastic viscosity remains essentially unchanged. Experimentally and theoretically it is found that the values of yield stresses are critically dependent on volume fraction of particles (Φ) and the magnitude of the applied electric field (E_0), and generally obey the following relation

$$\tau\left(E_0\right) \propto \Phi^{\Delta} E_0^{\alpha} \tag{1.11}$$

where exponent $1 \leq \alpha \leq 2$ commonly observed.

The polarization theory [44, 48-49] based on mismatch of dielectric permittivity between the particles to the suspending liquid predict the exponents as $\alpha=2$; $\Delta=1$. In this theory the response of particles and the suspending liquids are assumed to be linear with the applied electric field. For ideal dielectric particles, the attractive dipolar force F between the two particles is given by

$$F \propto \varepsilon_f \left(kE_0\right)^2 \tag{1.12}$$

where $k=(\varepsilon_p-\varepsilon_f)/(\varepsilon_p-2\varepsilon_f)$ is the dielectric mismatch parameter, and ε_p and ε_f the real components of the dielectric permittivities of the particles and suspending liquid respectively, and E_0 is the applied electric field. The shear modulus would increase linearly with the dielectric constant ratio $\varepsilon_p/\varepsilon_f$ [44], indicating that a high particle dielectric constant would give a strong ER effect. A material with an extremely high dielectric constant mismatch, like barium titanate suspensions (ε_p = 2000, depending on its crystallization state), has however been found to be inactive under application of a dc field, and active after adsorbing a small amount of water or being stimulated by an ac field, thus suggesting that the polarization model is not appropriate to describe this system [45-46]. In general, an important drawback of the polarization model is that it can not describe important ER experimental observations, such as the dependence on the electric field frequency or the dependence on the particle conductivity. Multipole- and many body- effects are usually added to the simplest polarization model (in equation 1.10) in order to account for interactions at relatively high particle volume fractions, i.e. when highly polarizable particles are close to one another [42, 48-49, 55]

The conductivity σ of the particles and the fluid has subsequently been included in the polarization model by replacing ε with the complex permittivity. The conduction model [54, 57, 60-61] considers that the ER effect with a dc electric field and a low frequency ac is induced by the mismatch of the conductivity of the particles $\sigma_p(E_0)$ and suspending liquid $\sigma_f(0)$, and given by the ratio $\Gamma=\sigma_p(E_0)/\sigma_f(0)$. In case of particle conductivity much greater than the conductivity of suspending liquid, a voltage drop occurs in the regions between two neighboring particles and hence produces very strong field strength there. The conductivity of the suspending medium $\sigma_f(E_0)$ is non-linear field dependent. Accounting for this non-linear conductivity effect of the suspending liquid, a non-linear conduction theory [59] has been proposed for the polarization of conductive particles. Both the conduction theory $\sigma_f(0)$, and the non-linear conduction theories, $\sigma_f(E_0)$, are based on the mismatch of conductivity of particles to the suspending liquid, and predict exponent-values [48,58] $1\leq\alpha< 2$ for high-to-low-to-moderate electric fields, $\Delta<1$ at both low- and high- volume fractions of particles, and $\Delta>1$ at intermediate volume fractions of particles [48, 58-63].

The conduction- and non linear- conduction models successfully may explain some ER phenomena that can not be explain by using the polarization model. The conduction models may predict the current density, the yield stress and the temperature dependence of ER fluids. However conduction models can only be used for the situation, where the suspension microstructure has been fully formed. The conduction models only consider the particle-particle interactions in a static microstructure after an electric field has been applied. Therefore these can not give an explanation of dynamic phenomena, such as the response time of an ER fluid. More important, some experimental results provide evidence against these mechanisms [45-46, 64]. The shortcoming of the polarization and conduction models is that all of them are static and do not take dynamic process occurring in ER fluids.

In order to explain and model dynamic events in ER fluids, as well as the effects of the conductivity on both the electric field induced particle aggregation process and the interfacial polarization process, a qualitative theory was derived by

Khusid and Acrivos [62], and it is much more powerful than the polarization and the conduction models. In this theory [62] some discrepancies with experimental results still exist. This is because two presumptions made, firstly no intrinsic dielectric dispersion of particles and suspending liquid is assumed, and secondly the variation of the applied electric field is assumed to be very slow compared with the polarization rate. These two assumptions are not always valid in ER fluids. There are other models available [45-49], however, none of them, including the polarization and conduction models, can explain all the current ER findings. They all suffer from a severe limitation: They cannot predict the yield stress based on the physical properties of ER fluids components and on the operating conditions of field strength, temperature, frequency, etc. They thus can not provide a clear clue or implication on how to formulate good ER fluids.

The dielectric loss model based on interfacial polarization of particle has been proposed [45-46] in order to understand the ER mechanism on the basis of all experimental findings [45-46]. Two dynamic processes are emphasized in this model. The first step is the particle polarization process, in which the particle dielectric permittivity is dominant. The second step is particle rotation, i.e. the polarized particles have the capability to align along the direction of the electric field. The second step is determined by the particle dielectric loss [45-46] that re-orientate the ER particle along the direction of an electric field, causing the formation of chains-or-columns like structures between two electrodes. The possible reason is that the ER particle has a comparatively high dielectric loss tangent [45-46, 64], ~0.1 at 1000 Hz, which can generate a large amount of bounded surface charge. The ER particle can even rotate under a weak electric field [64]. The ER particle turning under an electric field has ever been detected by using X-ray diffraction [65-67].

3. Experimental Techniques

In the present thesis work, structural and rheological properties of electrorheological fluids of synthetic smectites clay were studied. The types of clay were fluorohectorites, laponite, and a natural quick clay from the Trondheim Tiller area (Norway). Two types of silicone oils were used as suspending liquids.

3.1. Synthetic Fluorohectorite Clay: -

Synthetic smectite clay Na-fluorohectorite was purchased form Corning Inc. (New York) in powder form. This clay have the chemical formula $Na_{0.6}$ ($Mg_{2.4}$ $Li_{0.6}$) $Si_4O_{10}F_2$ per half unit cell, where Na is an interlayer exchangeable cation [13-14]. Three fluorohectorite clay powders, with different interlayer cations sodium (Na^+), nickel (Ni^{2+}) and iron (Fe^{3+}) are prepared through an ion exchange method. The corresponding cations salts (chlorides) of interlayer cations were dissolved in distilled water (pH=7) and added in an amount approximately five times the cation exchange capacity (122 milliequivalent per 100 gram of clay) [10] to promote saturation. After thorough mixing, the corresponding fluorohectorite clays were dialyzed against distilled water until a negative chloride test {mixing Cl^- with 1M $AgNO_3$ will results a white color precipitate AgCl} was obtained. After dialysis the

Na-fluorohectorite, Ni-fluorohectorite and Fe-fluorohectorite clay were first dried at 100 ^{0}C for ~10 hours and then grinded in powder form with the help of a mortar and spatula.

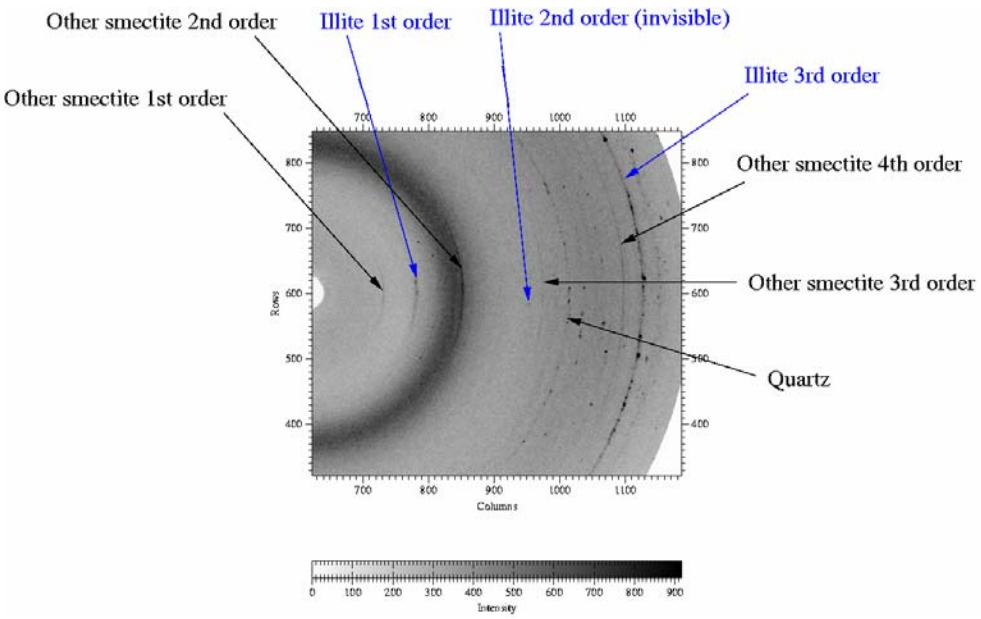

Figure 1.8:- A two-dimensional WAXS pattern of natural quick clay from Tiller area in Trondheim (Norway).

3.2. Natural Quick Clay: -

This clay was collected from 10 meter depth at the Tiller area in Trondheim (Norway). The clay was grinded in fine powder form with a mortar and spatula. Some amount of this powder was placed in distilled water containing vessel and a size fraction less than ~10 μm was separated according to Stokes Law of particle settling under gravity [1-2]. The obtained amount was heated at 100 ^{0}C for ~10 hours and again finely grinded in powder form. Thus the natural quick clay particles are polydisperse and particles size range from few *nm* to ~10 μm. A qualitative WAXS analysis (2θ<32^0), shows that this natural quick clay mineral contains smectites with other considerable amounts of impurities such as quartz, mica/illite etc. [67] as illustrated in Figure 1.8.

3.3. Synthetic Laponite Clay: -

The synthetic clay Laponite RD was purchased from Laporte, Ltd., in powder from. According to supplier, this clay have the chemical formula $Na_{-0.7}$ ($Mg_{-2.4}$ $Li_{-0.7}$) Si_8O_{20} $(OH)_4$ per half unit cell, where Na is an interlayer exchangeable cation

The clay was washed to remove any excess water soluble impurities and then dried at 130 ^{0}C and grinded in powder form with the help of a mortar and spatula.

3.4. Silicone Oil: -

The silicone oils used in the present study were Rotitherm M150 (specific density 0.976 and viscosity 100 mPa-s at 25 ^{0}C) silicone oil and Dow Corning 200 Fluid (specific density 0.976 and viscosity 100 mPa-s at 25 ^{0}C). The dielectric constant of silicone oil is 2.5 and it is a relatively non-conducting liquid with a dc conductivity of an order of ~10^{-12} Siemen per meter [60].

3.5. Preparation of Clays in Oil: -

Two types of ER fluids were prepared:

(1) For studying the structural morphology (X-ray scattering) only ER fluids of fluorohectorite and natural quick clay were prepared. The appropriate amounts of finely grounded clay powder (fluorohectorites and natural quick clay) were directly mixed with silicone oil in separate glass tubes at ambient temperature. Thereafter each of the glass tube was sealed and vigorously hand shaken for about 5 minute. Under these conditions fluorohectorite and natural quick clay particles were well dispersed in silicone oil.

(2) For the rheological investigations completely dried fluorohectorites and laponite clay were used to prepare the ER fluids. To remove any trace of water contents that was structurally attached to clay particles, the appropriate amounts of finely grounded fluorohectorite and laponite powder were heated at a fixed high temperature (~130 ^{O}C) and then mixed immediately with silicone oil in separate glass tubes. These glass tubes were sealed and let cooled down to room temperature. Thereafter each glass tube was vigorously hand shaken for about 5 minutes and then placed in an ultrasonic bath for 30 minutes at 25 ^{O}C. Under these conditions, the fluorohectorite and laponite clay particles were dispersed in silicone oil.

3.6. Microscopy and Microscopy cell: -

The experimental setup for microscopic observation is shown in Figure 1.9. The ER samples were placed between two copper electrodes. Voltages on copper electrodes were applied through combination of power supplies. The applied high voltages on copper electrodes were read on a multi-meter. The microscopic sample cell is rectangular made from two parallel copper electrodes of equal thickness of 1 mm, and separated by uniform gap of 1 mm. The copper electrodes are glued on to a transparent quartz glass slide which makes the bottom part of the cell. The top part of the cell is open. The two other wall of the sample cell is made from a non-conducting plastic material, which also serve as 1 mm spacers in between the copper electrodes.

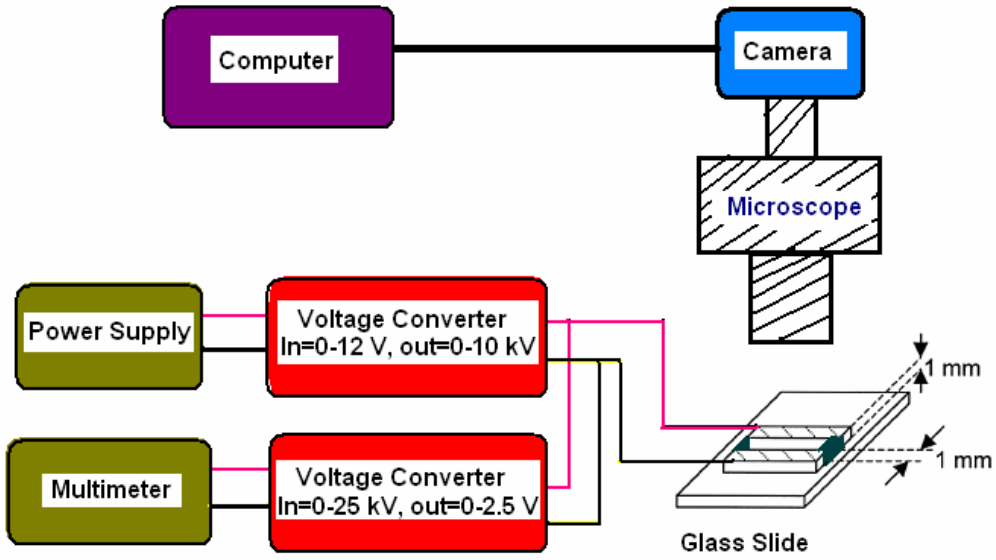

Figure 1.9:- Systematic illustration of microscopy. The samples were placed between two copper electrodes.

The sample cell is horizontally mounted on a Zeiss Stemi 2000C stereomicroscope attached to a Digital Microscope Camera connected to a desktop computer. A small volume (<1 ml) of ER fluids can be placed between the copper electrode from the open part of the cell. The bottom part of the cell is illuminated by visible light and the dynamics/changes in ER fluids on the top part while applying the electric field on copper electrodes can be recorded by a Digital Microscope Camera connected to a computer.

3.7. X-ray Scattering Techniques and Scattering Cell: -

Synchrotron wide angle X-ray scattering (WAXS) were carried out at the Swiss-Norwegian Beamline (SNBL) beamline (BM01A), and the synchrotron small angle X-ray scattering (SAXS) experiments were carried out at the Dutch-Belgian beamline (BM-26) at European Synchrotron Radiation Facility (ESRF, Grenoble, France) in ambient temperature. After and during applying electric fields scattered X-rays were collected from a two-dimensional detector placed behind the sample with respect to the incident horizontal X-ray beam, and data can be analyzed with respect to scattering vector q. Figure 1.10 shows the experimental setup of X-ray scattering experiments and ER scattering cell used. The angle φ is the azimuthal angle.

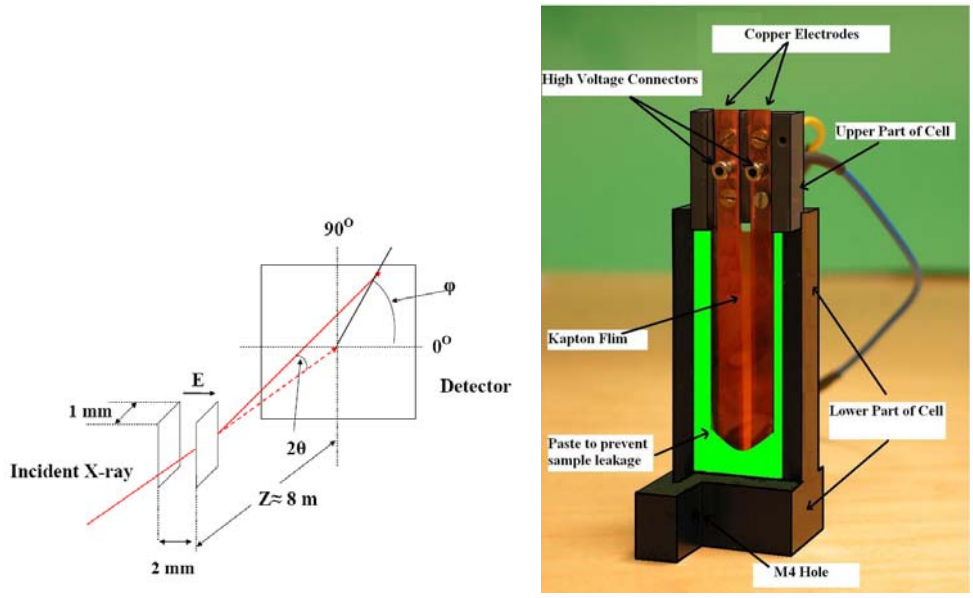

(a) **(b)**

Figure 1.10:- (a): X-ray Scattering geometry and **(b):** the ER scattering Cell. The ER fluids were placed between the electrodes and X-ray was incident perpendicular to the applied electric field.

The ER scattering cell is made form two parts: The upper part (detachable) is made of a non-conducting plastic material on which two copper electrodes (50×5×1 mm) were fixed with a uniform spacing (2 mm) between them. The lower part of cell is also made from a non-conducting plastic material, a thin kapton film (thickness 0.08 mm) and an easily removable paste preventing the leakage of ER fluids. The top part was open, bottom part was closed and both (front and back) sides were sealed by gluing a standard thin kapton film (thickness 0.08 mm).

The upper part of cell contain two parallel and identical 1 mm thick copper electrodes separated by a gap of 2 mm was inserted from the top and attached to the sample cell. M4 is the whole for a screw that help to mount the sample cell on X-ray setup. ER fluids (< 2 ml) can be poured (between the electrodes) from the top part.

3.8. Rheology Setup and Rheological Measurements: -

Rheological experiments were carried out at the Laboratory for Soft and Complex Matter Studies at Department of Physics NTNU Trondheim, Norway using a controlled shear stress (CSS) Physica Rheometer (MCR 300). The rheological setup is illustrated in Figure 1.11. This rheometer equipped with a coaxial cylinder cell (CC ERD/27), the outer cylinder was fixed and has a diameter ($2R_o$) 14.46 mm and the inner is rotating (Ω, steady state angular velocity) and has a diameter ($2R_i$) 13.33 mm respectively. The immersion length (h) was 40 mm and

sample volume was 19.35 ml. The rheological parameters (shear rate etc.) were set through the software US200. The dc voltages (kV) were supplied through a high voltage power supply (HCN -7E 12500) capable of delivering the voltage from 0-12.5 kV.

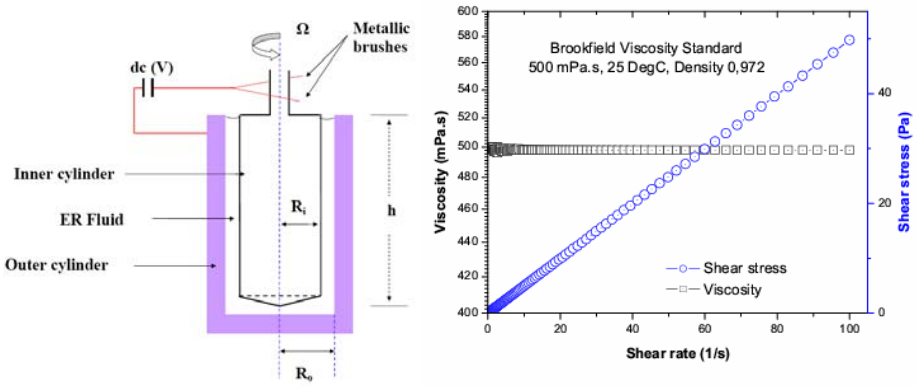

(a) **(b)**

Figure 1.11:- (a) Geometry of coaxial rotational rheometer and, **(b)** the measured flow- and viscosity- curve of a Brookfield Standard Fluid (η=500 mPa.s at 25°C).

The temperature of sample was controlled by a water circulating bath (Viscotherm VT2). Before performing rheological measurement on ER fluids, the rheometer was first adjusted for low viscosity measurement (~1.0 mPas) i.e., torque measurement below ~10^{-6} Newton-meter, by adjusting the motor speed (Ω) of at three constant rotations: 0.03, 0.06 and 0.09 per minute. Further more, the inner cylinder of rheometer is grounded for high voltage by two metallic brushes touching it. These two metallic brushes affect the measurement, so their overall contribution must be subtracted for measurement i.e., viscosity less than 500 mPas and shear stress ~5 Pa. The effect of the brushes is illustrated in Fig 1.12. It is clearly seen that the grounding brushes affect the viscosity curve of distilled water (viscosity~1mPas at 25 ^{0}C).

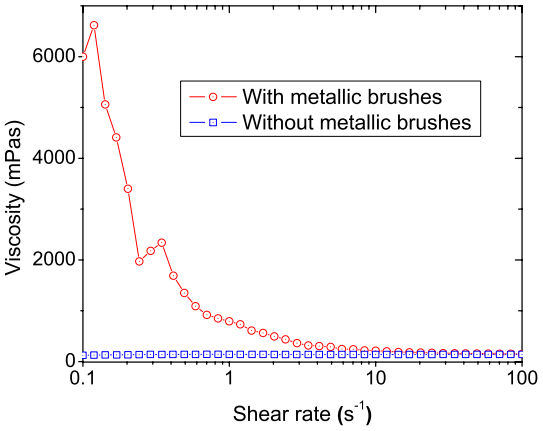

Figure 1.12 Measured viscosity-curve of distilled water (viscosity = 1.0 mPa.s at 25°C). The measurements are at 25°C, with and without the metallic brushes (see Figure 1.11 (a)).

The rheometer was calibrated using standard Newtonian fluids of known viscosities. Brookfield Viscosity Standards (viscosity = 100, 200, 500 mPa.s at 25°C) fluids were used for calibration. One of the calibration tests is illustrated in Figure 1.11 (b), where the measured viscosity is 498±4 mPa-s.

4. Brief introduction to the papers and contribution of author (Kanak P.S. Pamar)

First six papers (1-6) are presented in this thesis. The first five papers are devoted to experimental study of structural morphologies and rheological properties of electrorheological (ER) suspensions (or fluids) of synthetic nano-layered silicates i.e. smectites. Papers 1-3 exclusively deals with structural morphologies i.e. chains-or-columns like structures of three different types of X-fluorohectorite clay particles, distinguished by intercalated interlayer cation X, where X = Na^{+}, Ni^{2+} and Fe^{3+}. The papers 4 and 5 separately deal with the rheological properties of laponite clay- and fluorohectorite clay- oil suspensions respectively.

Paper 6 deals with structural morphologies in a related system of Na-fluorohectorite clay particles suspended in saline solutions. In paper 7, which is not included in the thesis, a theory accounting for the orientational distribution function (ODF) of fluorohectorites clay particles in the ER structures, based on the competition between homogeneizing entropic effects and aligning dipolar interaction, is presented and successfully compared to the data.

In papers 1, 2, 3, 6 and 7 all authors contributed to the synchrotron experiments as a team. In paper 1 and 7, the present author was responsible for making the experimental cell and for preparing the samples; he also contributed to the discussions of paper 1's results. In papers 2 and 3, the present author was responsible for making the experimental cell and preparing the samples, and contributed to the data analysis and discussions; he wrote the first version of paper 3, and contributed actively during the revision discussions that followed. In papers 4 and 5 the author was responsible for preparing the samples, performing the experiments, and contributed to the data analysis; and discussions; he wrote the first version of papers 4 and 5, and took active part in all revision discussions that followed. The present author took active part in the synchrotron experiments and discussions of paper 6.

The focus of paper 1 to use synchrotron WAXS to study chains-or-columns like structures (ER structures) of three different fluorohectorite (Na^{+}, Ni^{2+} and Fe^{3+}) in order to investigate the direction of induced polarization of nano-layered clay particles and the width of their orientation distribution function inside their ER structures. Further the goal was to study finite time effects of particle orientations (induced dipoles) as well as possible changes in interlayer spacing in applied electric fields.

Paper 2 and paper 3 exclusively deal with the positional nature of particle assemblies in ER structures investigated by synchrotron SAXS experiments. The nature of internal arrangements of nano-layered fluorohectorite particles in their ER structures were investigated by computing one-dimensional profiles of scattered intensity $I(q)$ versus scattering vector q along the direction of applied field, and perpendicular to it. The observed power law exponents and corresponding crossover q-values were used to determine the porous nature i.e. bulk pore sizes of assembled nano-layered fluorohectorite particles in their ER structures. The effects of particles thickness on pore sizes were investigated.

The focus of paper 4 and paper 5 is exclusively to study the effect of external electric fields (~kV/mm) on flow behavior of ER suspensions of laponite- and fluorohectorite- particles respectively. Rheological properties i.e. viscosity, shear stress and yield stress were mapped out as a function of particle concentration and the magnitude of applied electric field. The obtained yield stress results indicate that the conductivity (i.e. possible movement of surface charge and interlayer cations) of these nano-layered particles may play a major role for their polarization in external electric fields.

Paper 6 is a separate study dealing with structural morphologies in related systems of Na-fluorohectorite clay particles suspended in saline solutions. The SAXS patterns observed from these aqueous suspensions are highly anisotropic and show both similarities and differences compared to the patterns obtained from the fluorohectorite ER- case studied. These aqueous suspensions are under detailed study within the PhD of D. M. Fonseca, who is the main contributor to paper 6 and its first author. Paper 6 will be included in his PhD thesis as a main paper.

5. References

[1]. Richard A. Jones, “Soft Condensed Matter”, Oxford University Press (2002).

[2]. Ian W. Hamley, “Introduction to Soft Matter: Polymers, Colloids, Amphiphiles and Liquid Crystals”, John Wiley & Sons (2000).

[3]. Ciullo, P. A., “Industrial Minerals and Their Uses - A Handbook and Formulary”, William Andrew Publishing/Noyes (1996).

[4]. Bergaya F., Theng B. K. G. and Lagaly G., “Handbook of Clay Science, 1”, Elsevier Publication Ltd. (2006).

[5]. Velde B., “Clays and clay minerals in natural and synthetic systems”, Elsevier Publication Ltd. (1977).

[6]. Bailey S. W., “Summary of recommendations of AIPEA nomenclature committee on clay minerals”, American Mineralogist, V. 65, 1-7 (1980).

[7]. B. Velde, “Introduction to Clay Minerals", Chapman and Hall, London (1992).

[8]. Brindley and Brown, “Crystal structures of clay minerals and their X-ray identification”, Mineralogical Society, London (1980).

[9]. Moore, D. M. and Reynolds, R. C., “X-ray diffraction and the identification and analysis of clay minerals”, Oxford University Press (1989).

[10]. Kaviratna P. D., Pinnavaia T. J. and Schroeder P. A., “Dielectric Properties of Smectite Clays”, J. Phys. Chem. Solids. l57, 1897 (1996).

[11]. Brindley, G. W., “Ethylene glycol and glycerol complexes of smectites and vermiculites”, Clay minerals 6, 237 (1965).

[12]. Henoricks, S. B., Nelson, R. A. and Alexander, L. T., “Hydration mechanism of the clay mineral montmorillonite saturated with various cations”, J. Am. Chem. Soc. 62, 1457 (1940).

[13]. da Silva G. J., Fossum J. O., DiMasi E. and Måløy K. J., “Hydration transitions in a nanolayered synthetic silicate: A synchrotron x-ray scattering study”, Phys. Rev. B, 67 094114 (2003).

[14]. da Silva G. J., Fossum J. O., DiMasi E., Måløy K. J. and Lutnæs S.B., “Synchrotron x-ray scattering studies of water intercalation in a layered synthetic silicate”, Phys. Rev. E, 66 011303 (2002).

[15]. Gunier A. and Fournet G., “Small Angle Scattering of X-rays”, John Wiley Ltd. (1955).

[16]. Glatter O. and Kratky O., “Small Angle X-ray Scattering”, Academic Press Ltd. (1982).

[17]. Feigin L. A., and Svergun D. I., in “Structure Analysis by Small Angle X-ray and Neutron Scattering”, G.W. Taylor (editor), Plenum Press Ltd. (1987).

[18]. Hendricks S.B. and Teller E., “X-ray interference in partially ordered layer lattices”, J. Chem. Phys. 10, 147 (1942).

[19]. Reynolds, Jr., R.C., “Principles of powder diffraction”. in Modern Powder Diffraction: V. 20, edited by Bish D. L. and Post J. E., The

Mineralogical Society of America, Washington, D.C. QE351.M43 v.
[20]. Pedersen J. S., "Analysis of small-angle scattering data from colloids and polymer solutions: modeling and least-squares fitting- I", Adv. Colloid Interface Sci., 70, 171 (1997).
[21]. P. W. Schmidt, in "Fractal Approach to Heterogeneous Chemistry: Surfaces Colloids and Polymers", edited by D. Avnir, John Wiley & Son Ltd., pp. 67–79 (1989).
[22]. Bale H. D. and Schmidt P. W., "Small-Angle X-Ray-Scattering Investigation of Submicroscopic Porosity with Fractal Properties", Phys. Rev. Lett. 53, 596 (1984).
[23]. Erzan A. and Gungor N., "Fractal Geometry and Size Distribution of Clay Particles", J. Colloid Interface Sci. 176, 301 (1995).
[24]. Marshall, C. E., "The Colloid Chemistry of the Silicate Minerals". Academic Press Ltd., N.Y., pp 195 (1949).
[25]. van Olphen, H., "An Introduction to Clay Colloid Chemistry: for clay technologists, geologists, and soil scientists", Wiley, New York (1977).
[26]. Güven N. and Pollastro R. M., "Clay-Water Interface and its Rheological Implications", CMS Workshop Lectures, Volume 4 (1993).
[27]. Luckham P.F., and Rossi S., "The colloidal and rheological properties of bentonite suspensions", Adv. Colloid and Interface Sci. 82, 43 (1999).
[28]. Macosko C.W., "Rheology: Principles, Measurements, and Applications", John Wiley & Sons, Canada (1994).
[29]. Barnes H. A., Hutton J. F., Walters K., "An Introduction to Rheology", Elsevier Publication Ltd. (1989).
[30]. Coussot P., Nguyen Q. D., Huynh H.T. and Daniel Bonn, "Avalanche Behavior in Yield Stress Fluids", Phys. Rev. Lett. 88, 175501 (2002).
[31]. T. Freltoft, J. K. Kjems, and S. K. Sinha, **"**Power-law correlations and finite-size effects in silica particle aggregates studied by small-angle neutron scattering**",** Phys. Rev. B 33, 269 (1986).
[32]. G. Dietler, C. Aubert, and D. S. Cannell, **"**Gelation of Colloidal Silica**"**, Phys. Rev. Lett. 57, 3117 (1986).
[33]. R. Vacher, T. Woigner, J. Pelous, and E. Courtens, **"**Structure and self-similarity of silica aerogels**"**, Phys. Rev. B 37, 6500 (1988).
[34]. D. W. Schaefer and K. D. Keefer, **"**Structure of Random Porous Materials: Silica Aerogel**"**, Phys. Rev. Lett. 56, 2199 (1986).
[35]. S. K. Sinha, T. Freltoft, and J. K. Kjems, in "Kinetics of Aggregation and Gelation", edited by F. Family and D. P. Landau, Elsevier, Amsterdam, pp. 87–90 (1984).
[36]. Wong, P.-Z., Howard J. and Lin J.-S, **"**Surface Roughening and the Fractal Nature of Rocks"**,** Phys. Rev. Lett. 57, 637 (1986).
[37]. D. F. R. Mildner, R. Rezvani, P. L. Hall, and R. L. Borst, "Small-angle scattering of shaley rocks with fractal pore interfaces", Appl. Phys. Lett. 48, 1314 (1986).
[38]. G. Lucido, R. Triolo, and E. Caponetti, **"**Fractal approach in

petrology: Small-angle neutron scattering experiments with volcanic rocks**”**, Phys. Rev. B 38, 9031 (1988).
[39]. A. P. Radlinski, C. J. Boreham, G. D. Wignall, and J.-S. Lin, **“**Microstructural evolution of source rocks during hydrocarbon generation: A small-angle-scattering study”, Phys. Rev. B 53, 14152 (1996).
[40]. P. Pfeifer and D. Avnir, “Chemistry in noninteger dimensions between two and three. I. Fractal theory of heterogeneous surfaces”, J. Chem. Phys. 79, 3558 (1983).
[41]. G. Porod, Kolloid Z 124, 93 (1951).
[42]. Tao, R., “International Conference on Electrorheological Fluids: Mechanism, Properties, Structure, Technology and Application”, World Scientific Singapore (1992).
[43]. Halsey, T.C. “Electrorheological fluids”. Science 258, 761 (1992).
[44]. Halsey T. C. and Toor W., “Structure of electrorheological fluids”, Phys. Rev. Lett. 65, 2820 (1990).
[45]. Hao T., “Electrorheological Fluids”, Adv. Mater. 13, 1847 (2002).
[46]. Hao T., “Electrorheological suspensions” Adv. Colloid and Interface Sci. 97, 1 (2002).
[47]. Gast A. P. and Zukoski C. F., “Electrorheological fluids as colloidal suspensions”, Adv. Colloid Interface Sci. 30, 153 (1989).
[48]. Block H., Kelly J. P., Qin A. and Watson T., “Materials and mechanisms in electrorheology”, Langmuir, 6, 6 (1990).
[49]. Parthasarathy M. and Klingenberg D. J., “Electrorheology: mechanisms and models”, Materials Sci. Eng. R17, 57 (1996).
[50]. Wen W., Ma H., Tam W., and Sheng P., “Frequency-induced structure variation in electrorheological fluids”, Appl. Phys. Lett. 77, 3821 (2000).
[51]. Ota M. and Miyamoto T., “Optimum particle size distribution of an electrorheological fluid”, J. Appl. Phys. 76, 5528 (1994).
[52]. Wu C. W. and Conrad H., “Influence of mixed particle size on electrorheological response”, J. Appl. Phys. 83, 3880 (1998).
[53]. Wong, W. and Shaw M.T., “The role of water in electrorheological fluids”, In:, Anonymous (1998).
[54]. Anderson R. A., “Effect of finite conductivity in electrorheological fluids”, Proc. 3rd. Int. Conf. on Electrorheological Fluids, edited by R Tao (Singapore: World Scientific) pp. 81-90 (1992).
[55]. Jordan T.C. and Shaw M.T., “Electrorheology**”** IEEE Trans. Electr. Insulation, 24, 849 (1989).
[56]. Filisko FE and Radzilowski LH, **“**An intrinsic mechanism for the activity of alumino-silicate based electrorheological materials” J Rheo. 34, 539 (1990).
[57]. Davis L. C., “Polarization forces and conductivity effects in electro-rheological fluids”, J. Appl. Phys. 72, 1334 (1992); L.C. Davis, Appl. Phys. Lett. 60, 319 (1992).
[58]. Klingenberg D. J. and Zukoski C. F., “Studies on the steady-shear behavior of electrorheological suspensions”, Langmuir 6, 15 (1990).

[59]. Felici N., Foulc J. N. and Atten P., "A conduction model of electro-rheological effect", Proc. 4th Int. Conf. Electrorheological Fluids, edited by R Tao and G D Roy (Singapore: World Scientific) pp. 139-52 (1994).
[60]. Tang X., Wu C. W. and Conrad H., "On the conductivity model for the electro-rheological effect", J. Rheo. 39, 5, 1059 (1995).
[61]. Wu C. W. and Conrad H., "A modified conduction model for the electrorheological effect" J. Phys. D: Appl. Phys. 29, 3147 (1996).
[62]. Khusid B. and Acrivos A., **"**Effects of conductivity in electric-field-induced aggregation in electrorheological fluids", Phys. Rev. E 52, 1669 (1995).
[63]. Martin, J. E. and Anderson, R. A., "Chain model of electrorheology". J. Chem. Phys. 104, 4814 (1996).
[64]. Hao T., Kawai A. and Ikazaki F., **"**Mechanism of the Electrorheological Effect: Evidence from the Conductive, Dielectric, and Surface Characteristics of Water-Free Electrorheological Fluids", Langmuir 14, 1256 (1998).
[65]. Wen W. and Lu K., "A primary x-ray investigation of the turning of ferroelectric microspheres contained in electrorheological fluids under a direct current electric field", Appl. Phys. Lett. 68, 1046 (1996).
[66]. Lan Y., Xu X., Men S. and Lu K., **"**Orientation of particles in an electrorheological fluid under an electric field", Phys. Rev. E 60, 4336 (1999).
[67]. J.O. Fossum, Y. Méheust, K.P.S. Parmar, K.D. Knudsen, K.J. Måløy and D.M. Fonseca, "Intercalation-enhanced electric polarization and chain formation of nano- layered particles", Europhys. Lett. **74** (3), pp. 438-444 (2006).
[68]. J. S. Chong J.S., Christiansen E.B. and Baer A.D., "Rheology of concentrated suspensions", J. Appl. Polym. Sci. 15, 2007 (1971)
[69]. Coussot P. "Structural similarity and transition from Newtonian to Non-Newtonian Behavior for Clay-Water Suspensions", Phy. Rev. Lett.74, 3971(1995).

Paper 1

EUROPHYSICS LETTERS 1 May 2006

Europhys. Lett., **74** (3), pp. 438–444 (2006)
DOI: 10.1209/epl/i2005-10541-0

Intercalation-enhanced electric polarization and chain formation of nano-layered particles

J. O. Fossum[1], Y. Méheust[1], K. P. S. Parmar[1], K. D. Knudsen[2], K. J. Måløy[3] and D. M. Fonseca[1]

[1] *Department of Physics, NTNU - Hoegskoleringen 5, NO-7491 Trondheim, Norway*
[2] *Physics Department, IFE - P.O. Box 40, NO-2027 Kjeller, Norway*
[3] *Physics Department, UiO - Postboks 1048 Blindern, NO-0316 Oslo, Norway*

received 21 December 2005; accepted in final form 28 February 2006
published online 22 March 2006

PACS. 61.10.Eq – X-ray scattering (including small-angle scattering).
PACS. 82.70.Dd – Colloids.
PACS. 83.80.Gv – Electro- and magnetorheological fluids.

Abstract. – Microscopy observations show that suspensions of synthetic and natural nano-layered smectite clay particles submitted to a strong external electric field undergo a fast and extended structuring. This structuring results from the interaction between induced electric dipoles, and is only possible for particles with suitable polarization properties. Smectite clay colloids are observed to be particularly suitable, in contrast to similar suspensions of a non-swelling clay. Synchrotron X-ray scattering experiments provide the orientation distributions for the particles. These distributions are understood in terms of competing i) homogenizing entropy and ii) interaction between the particles and the local electric field; they show that clay particles polarize along their silica sheet. Furthermore, a change in the platelet separation inside nano-layered particles occurs under application of the electric field, indicating that intercalated ions and water molecules play a role in their electric polarization. The resulting induced dipole is structurally attached to the particle, and this causes particles to reorient and interact, resulting in the observed macroscopic structuring. The macroscopic properties of these electro-rheological smectite suspensions may be tuned by controlling the nature and quantity of the intercalated species, at the nanoscale.

In this letter we study colloidal suspensions of electrically polarizable particles in insulating fluids. When such suspensions are subjected to an external electric field, usually of the order of 1 kV/mm, the particles become polarized, and subsequent dipolar interactions are responsible for aggregating a series of interlinked particles that form chains and columns parallel to the applied field. This structuring occurs within seconds, and disappears almost instantly when the field is removed [1–5]. It coincides with a drastic change in rheological properties (viscosity, yield stress, shear modulus, etc.) of the suspensions [6], which is why they are sometimes called electrorheological fluids (ERFs). This makes the mechanical behavior readily controllable by using an external electric field [1–7]. Particle size has a quite diverse impact on the behavior of ERFs [8]. The nature of the insulating fluid and of the colloidal particles determines the electrorheological behavior of the suspensions. The mechanism is not fully understood yet, but

it is mainly triggered by the so-called interfacial polarization, and requires electric anisotropy of the particles [9]. Consequently, particle shape [10] and surface properties [11] can also be critically important, as dielectric properties largely depend on them.

Clays as traditional material have played an important role throughout human history. Their common modern uses include nano-composites, rheology modification, catalysis, paper filling, oil well-drilling and -stability, etc. [12]. The basic structural unit of so-called 2 : 1 clays is a 1 nm-thick platelet consisting of two tetrahedral silica sheets sandwiching one octahedral silica sheet. Smectites are 2 : 1 clays for which platelets carry a moderate negative surface charge on their plane surfaces. This charge is sufficiently large so that individual platelets are able to stack by sharing cations, and moderate enough so as to allow further intercalation of water molecules into the resulting "decks of cards"-like smectite particles. Natural smectite clay particles dispersed in salt solutions have been studied for decades [12], and recently there has been a growing activity in the study of complex physical phenomena in synthetic smectites [13]. Much effort has gone into relating the lamellar microstructure of smectite clay-salt water suspensions to their collective interaction and to resulting macroscopic physical properties, such as phase behavior and rheological properties [13–21]. Nematic liquid crystalline-like ordering in smectite systems has been characterized by the observation of birefringent domains with defect textures [14, 16, 18, 19] or by Small-Angle X-Ray Scattering [16, 18].

Wide Angle X-Ray Scattering (WAXS) studies of the well-characterized synthetic smectite clay fluorohectorite, in water suspensions [17], show that fluorohectorite particles contain about 80 1 nm thick platelets. Due to their large structural surface charge ($1.2\,e^-$/unit cell [22]), fluorohectorite stacks remain intact when suspended in water, in contrast to those of laponite ($0.4\,e^-$/unit cell) or of the natural clay montmorillonite. The natural smectite illite ($0.9\,e^-$/unit cell [23]) on the other hand, behaves much like fluorohectorite in this respect [24]. For fluorohectorite, the number of mono-layers of water that can be intercalated into the stacks, depending on temperature and relative humidity, has been mapped for hydration and dehydration by means of synchrotron X-ray scattering techniques [25]. However, the spatial configuration for the intercalated water molecules, with respect to the silica sheets and to the intercalated cations, is not precisely known yet. We show in this letter that the strong electro-rheological behavior exhibited by suspensions of smectite clay particles in silicon oil can be attributed to the intercalated species.

We studied four types of smectite suspensions in oil: Firstly, three suspensions based on fluorohectorite (see [17] for its origin and chemical formula), and secondly, a mixed natural quick clay from the Trondheim region in Norway. The three types of fluorohectorite samples differ by the nature of the exchangeable cation, which is either mono- (Na^+), di- (Ni^{2+}) or tri-valent (Fe^{3+}). These synthetic samples are polydisperse with wide distributions of sizes (diameter up to a few micrometers, stack thicknesses around 100 nm) and aspect ratios. The quick clay is far less well characterized than the synthetic clays, although from preliminary X-ray diffraction analysis we know that this mixed natural clay contains considerable amounts of illite and other natural smectite particles, in addition to the non-smectite clay kaolinite. The samples were initially prepared at ambient temperature by adding 1.5% by weight of clay particles to the silicon oil Rotitherm M150 (viscosity 100cSt at 25 °C) , and subsequently removing the heavier particles ($\gtrsim 10\,\mu$m) by sedimentation, which modified only marginally the suspensions' particle density.

When placed between copper electrodes between which a sufficiently strong electric field is applied, the four types of samples exhibit the dipolar chain formation characteristic of ERFs (see fig. 1). The sample cell used for these observations consisted of two parallel and identical 1/2 mm thick copper electrodes separated by a gap of 2 mm and glued onto a transparent quartz glass microscope slide. The gap between the electrodes was closed at its ends by

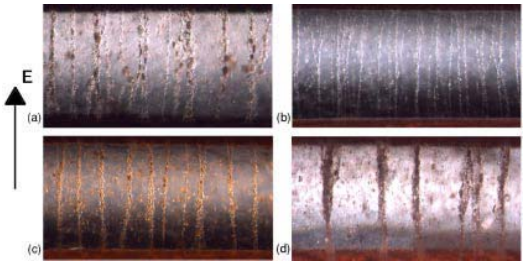

Fig. 1 – Microscope images of electrorheological chain formation in oil suspensions of smectite clays. (a) Na-fluorohectorite. (b) Ni-fluorohectorite. (c) Fe-fluorohectorite. (d) Natural quick clay.

a non-conducting plastic material. The top part of the cell was open, and the sample cell was mounted horizontally, with the microscope slide flat down. A small volume ($< 1\,\mathrm{ml}$) of the prepared sample was added and studied at ambient temperatures. The sample was illuminated from below, and observed from above in a stereomicroscope. An electric field $E \sim 500\,\mathrm{V/mm}$ was applied between the copper electrodes, and the changes in the sample were recorded by means of a digital camera connected to a PC. The process resulted in all clay particles being part of the electrorheological chain bundles after 10 to 20 s, and no motion being visible within the sample in less than 1 min. The critical electric field necessary to trigger the electrorheological behavior was found to be $E_c \simeq 400\,\mathrm{V/mm}$.

The procedure was then repeated using a suspension of kaolinite, a 1 : 1 natural clay which, in contrast to smectite clays, does not spontaneously intercalate cations and water molecules in between its silica sheets. Kaolinite particles in their natural state have been reported in the literature to exhibit a weak electrorheological behavior when suspended in a silicon oil [26]. Microscopy observations of kaolinite suspensions with the same density as the smectite suspensions exhibited electrorheology, but only for $E \gtrsim 2\,\mathrm{kV/mm}$. They formed with characteristic time 10 to 100 times larger than that of the smectite suspensions. Furthermore, the bundle structure formed by the kaolinite suspensions appeared much less ordered than those observed with the smectites.

Relative orientations of the smectite particles inside the electrorheological chains were determined using synchrotron X-ray scattering experiments: chain and column formations were observed by means of a video camera, while simultaneously recording X-rays scattered

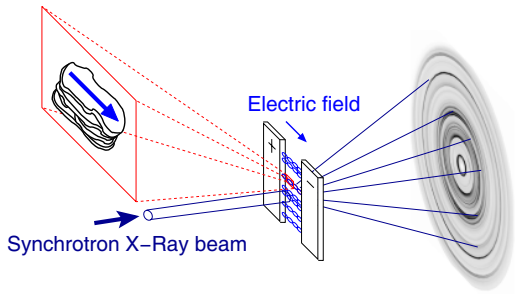

Fig. 2 – Sketch of the X-Ray scattering experiments. Corresponding diffractograms are shown in figs. 3(b) and (c). The magnified area shows a single nano-layered clay particle inside a dipolar chain; the arrow indicates the direction of the dipole moment induced by the external electric field.

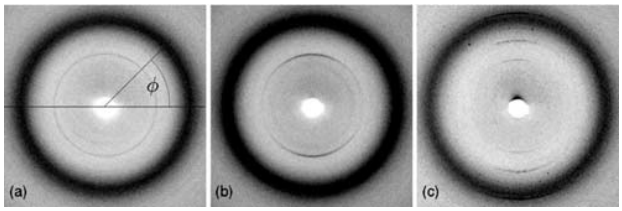

Fig. 3 – Central regions of two-dimensional WAXS images of the electrorheological samples. (a) Suspension of Na-fluorohectorite at $E \sim 0$. (b) Suspension of Na-fluorohectorite for $E \sim 500\,\mathrm{V/mm} > E_c$. (c) Natural quick clay for $E \sim 500\,\mathrm{V/mm} > E_c$.

by the clay crystallites. These experiments were performed at the Swiss-Norwegian Beamlines (SNBL) at ESRF (Grenoble, France), using the WAXS setup with a 2D mar345 detector at beamline BM01A. The sample cells used for these experiments differ from those described above in that the electrodes were placed vertically, the cells being closed at the bottom and with their top open, which allowed to partly fill the cell with sample from above. A sketch of the experiment is shown in fig. 2.

Figure 3 shows three different two-dimensional diffractograms. Figure 3(a) is obtained from a suspension of Na-fluorohectorite prior to the application of an electric field. Each lamellar clay particle may be regarded as a single crystallite, and the particles are randomly oriented inside the sample, so the image is isotropic. The broad outermost ring is due to scattering from the silicon oil (characteristic length $d \sim 6.9$–$7.9\,\text{Å}$), whereas the narrow symmetric ring at lower scattering angles is the (001) Bragg peak from the lamellar clay stacks with 1 water layer intercalated ($d \sim 12.3\,\text{Å}$). In the presence of an electric field (fig. 3(b)), in contrast, the (001) Bragg peak has become anisotropic due to particle orientation in the field. In addition, the number of water layers intercalated was determined directly from the positions of the Bragg peaks in reciprocal space (as in [27]). Figure 3(c) shows the diffractogram of a suspension of natural quick clay, for $E > E_c$. Three anisotropic scattering rings are visible: the 1st order of illite ($d \sim 10.1\,\text{Å}$), and the 1st ($d \sim 14.28\,\text{Å}$) and 2nd order of an another smectite clay. The whole diffractogram (not shown here) also reveals the 3rd-order ring of illite, and the 3rd- and 4th-order rings of the other smectite clay. All the visible diffraction rings correspond to diffraction by smectite clays and are anisotropic. Figure 4(a) shows how the intensity of circular scattering rings such as those presented in fig. 3 evolve as a function of the azimuthal angle, between 0 and 360°. In the case of fluorohectorite, we have considered the ring at a radial position corresponding to the first-order Bragg peak for the clay stack [27], which is characteristic of 1 mono-layer of intercalated water at ambient temperatures ($d \sim 12.4\,\text{Å}$ for the Na-fluorohectorite). For the natural sample, we have considered the lowest-order Bragg peak of illite (see fig. 3(c)). The scattered intensity at a given azimuthal angle is proportional to the number of particles that meet the Bragg condition for that angle, so the shapes of the scattered intensities in fig. 4(a) provide the orientation distributions of clay particle orientations inside the chains and columnar structures. For $E \sim 0$, the intensities are independent of ϕ (except for the experimental noise). For $E > E_c$, the azimuthal positions of the maxima along the plots in fig. 4(a) demonstrate that the preferred orientation of the clay particles is with the lamellar stacking plane parallel to the direction of the electric field. Since the collective dipolar interactions between particles align their dipole moments with the electric field, the preferred direction of polarization for each stacked particle could also be inferred, as indicated in the insert of fig. 2: it is parallel to the silica sheets.

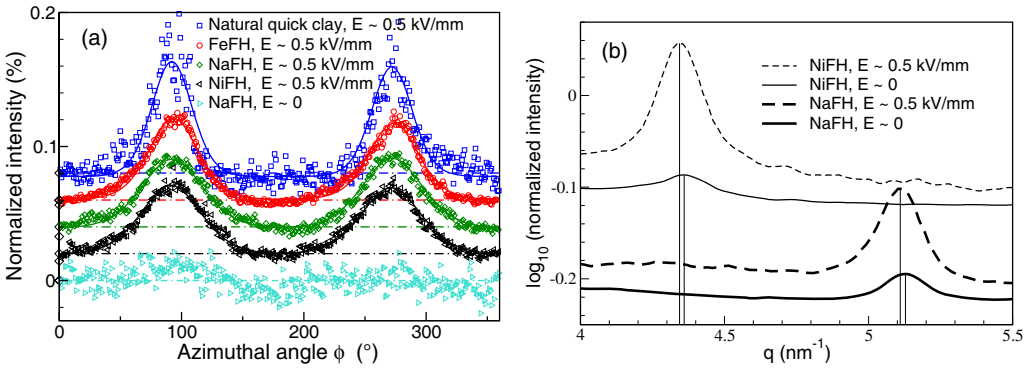

Fig. 4 – (a) Dependence of the intensity of circular scattering rings on the azimuthal angle ϕ: data and corresponding theoretical fits. (b) Scattering lines along the q direction for the Na- and Ni-fluorohectorite samples in the 1WL hydration state (corresponding, respectively, to $d = 2\pi/q = 12.26\,\text{Å}$ and $d = 14.41\,\text{Å}$ for $E \sim 0$): a systematic increase of the platelet separation inside the clay particles occurs under application of the electric field, and results in a shift of the corresponding diffraction peak. In (a) and (b), the plots have been imposed a different vertical offset, for clarity.

Colloids that make "good" electrorheological particles are known to possess two important properties, which allow them to not only polarize, but also to rotate under the effect of the electric field: i) their interfacial polarizability is important, and ii) they are electrically anisotropic [9, 28]. In the case of our platelet-shaped nano-layered smectite clay particles, particle polarization occurs along their silica sheet. A fine monitoring of the scattering line along q shows that the application of the electric field results in a subtle increase in the characteristic separation between adjacent platelets inside clay particles (see fig. 4(b)), of about 0.05 Å. This is consistent with polarization occurring mainly by movement of charges along the quasi-2D inter-layer space, perpendicular to the stacking direction, for example by movement of ions out of preferred sites on inter-layer surfaces. We believe that the intercalated cations and possibly water molecules dominate the interfacial polarization process for smectite particles, which explains the low critical field and fast response observed for the smectite suspensions as compared to the kaolinite suspensions.

Considering that the induced dipole is structurally forced to remain in the plane of the silica sheets, we can explain why the particles rotate under application of the field, and we can further describe the distribution of particle orientations around the mean orientation in terms of a competition between i) the homogenizing entropy and ii) the aligning effect of the strong external electric field. Indeed, the Gibbs energy of the colloid population can be written as the sum of an entropic term and of the interaction energy of the clay particles with a local mean electric field aligned with the external field. These two terms are dependent on the functional form of the orientation distribution probability (ODP) function, f, of the particles. Minimizing the Gibbs energy with respect to that functional form yields the orientation distribution at equilibrium. This calculation is presented in detail in a separate manuscript [29]; it follows the line of the well-known theory developed by Maier and Saupe to describe a different geometry, namely nematic ordering [30, 31]. In our system, the interaction energy is different from that of Maier and Saupe, but the final functional form obtained for f is identical: $f(\alpha) \propto \exp[m \cos^2 \alpha]$, where the angle α denotes the deviation from the mean orientation, while the physical parameters characteristic of the system are contained in the expression of the parameter m [29]. Obviously, the expression for m is different in our system from what it is

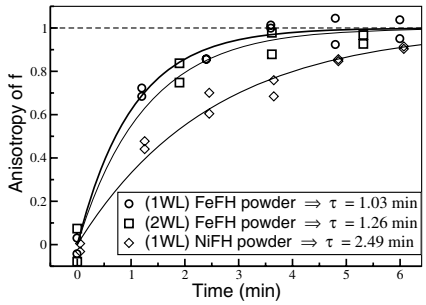

Fig. 5 – Anisotropy of the ODP function as a function of time during the buildup of the electrorheological structure. The anisotropy is computed as the amplitude of the oscillations in fig. 4(a), normalized by its asymptotic value at large times. The characteristic time τ is obtained by fitting an exponential profile to the data.

in the Maier-Saupe theory. For each type of clay in fig. 4, we have fitted the proper profiles to the data in order to infer the Maier-Saupe ODP function f of the particles within the bundles (see [32] for a detailled description of the method). The RMS values for the half width of f are: $25.1 \pm 0.3°$ for Na-fluorohectorite, $24.7 \pm 0.4°$ for Ni-fluorohectorite, $20 \pm 0.7°$ for Fe-fluorohectorite, and $17.2 \pm 0.06°$ for the natural quick clay, which corresponds to values of the corresponding order parameter, $S = \langle 3 \sin^2 \alpha - 2 \rangle_f$ [29], of 0.53, 0.54, 0.68 (Ni-, Na-, Fe-fluorohectorite, respectively) and 0.76 (natural clay) [29]. This difference in order parameter magnitude may be related to differences in particle size and polydispersity.

What exactly occurs in the between-platelets space under the application of the electric field remains unclear. We have monitored the transient buildup of the orientation distributions (as represented in fig. 4(a)) following the sudden switch-on of the electric field above E_c. Figure 5 shows the amplitude of the azimuthal profiles (such as those shown in fig. 4(a)) as a function of time; the plots have been rescaled so that the amplitude at infinite time be equal to 1. Characteristic time scales τ were obtained from fits in the form $1 - \exp[-t/\tau]$; the time scales obtained are of the same order as or a bit larger than the durations after which no particle movement is visible in the microscope. As shown by fig. 5, those dynamical experiments did resolve clear differences in characteristic time scales for chain ordering depending on the type of intercalated ion; for example, a factor of 2 (faster dynamics) was observed in the buildup velocity for Ni-, as compared to Fe-, fluorohectorite samples. In contrast, when preparing fluorohectorite samples in different hydration states, we were not able to resolve a dependency of the transient dynamics on the number of intercalated water layers, although we cannot exclude the possibility of such effects existing within our experimental uncertainty. Yet, our present data clearly indicates that the role of ions in the polarization process dominates that of water molecules. Understanding the mechanisms underlying the particle polarization shall require experiments utilizing other experimental techniques. An EXAFS study of the vicinity of the intercalated nickel cations during particle polarization, which can show how their spatial configuration inside the interlayer space is modified by the electric field, is planned. Note that for these suspensions, one may be able to control the characteristic time for dipolar chain formation on the macro-scale by manipulating, on the nano-scale, the nature of the intercalated ions as well as the number of intercalated water layers. Among foreseeable applications are the ones common to electrorheological fluids [33]. Another potential application is a method for separating smectite from non-smectite components, in natural clays.

* * *

We gratefully acknowledge assistance from the staff of the Swiss-Norwegian Beam Lines at ESRF. J. JØNLAND generously provided us with the natural clay. This work was supported by the Research Council of Norway (RCN) through the NANOMAT Program: RCN project numbers 152426/431, 154059/420 and 148865/432, as well as 138368/V30 and SUP154059/420.

REFERENCES

[1] GAST A. P. and ZUKOSKI C. F., *Adv. Colloid Interface Sci.*, **30** (1989) 153.
[2] HILL J. C. and VAN STEENKISTE T. H., *J. Appl. Phys.*, **70** (1991) 1207.
[3] HALSEY T. C., *Science*, **258** (1992) 761.
[4] HALSEY T. C. and MARTIN J. E., *Sci. Am.*, **269** (1993) 58.
[5] WEN W. D., ZHENG W. and TU K. N., *J. Appl. Phys.*, **85** (1999) 530.
[6] WEN W., HUANG X., YANG S., LU K. and SHENG P., *Nature Mater.*, **2** (2003) 727.
[7] SPRECHER A. F., CARLSON J. D. and CONRAD H., *Mater. Sci. Eng.*, **95** (1987) 187.
[8] TAN Z.-J., ZOU X.-W., ZHANG W.-B. and JIN Z.-Z., *Phys. Rev. E*, **59** (1999) 3177.
[9] HAO T., KAWAI A. and IKAZAKI F., *Langmuir*, **14** (1998) 1256.
[10] QI Y. and WEN W., *J. Phys. D*, **35** (2002) 2231.
[11] DÜRRSCHMIDT T. and HOFFMANN H., *Colloid Surf. A*, **156** (1999) 257.
[12] VELDE B., *Introduction to Clay Minerals* (Chapman and Hall, London) 1992.
[13] FOSSUM J. O., *Physica A*, **270** (1999) 1.
[14] MOURCHID A., LECOLIER E., VAN DAMME H. and LEVITZ P., *Langmuir*, **14** (1998) 4718.
[15] BONN D., KELLAY H., TANAKA H., WEGDAM G. and MEUNIER J., *Langmuir*, **15** (1999) 7534.
[16] GABRIEL J.-C. P. *et al.*, *Nature*, **413** (2001) 504.
[17] DIMASI E., FOSSUM J. O., GOG T. and VENKATARAMAN C., *Phys. Rev. E*, **64** (2001) 061704.
[18] LEMAIRE B. J., PANINE P., GABRIEL J.-C. P. and DAVIDSON P., *Europhys. Lett.*, **59** (2002) 55.
[19] FOSSUM J. O., GUDDING E., FONSECA D. M., MÉHEUST Y., DIMASI E., GOG T. and VENTAKARAMAN C., *Energy*, **30** (2005) 873.
[20] COUSSOT P., NGUYEN Q. D., HUYNH H. T. and BONN D., *Phys. Rev. Lett.*, **88** (2002) 175501.
[21] BONN D., TANASE S., ABOU B., TANAKA H. and MEUNIER J., *Phys. Rev. Lett.*, **89** (2002) 015701.
[22] KAVIRATNA P. D., PINNAVAIA T. J. and SCHROEDER P. A., *J. Phys. Chem. Solids*, **57** (1996) 1897.
[23] MOORE D. M. and REYNOLDS R. C. jr, *X-Ray Diffraction and the Identification and Analysis of Clay Minerals*, 2nd edition (Oxford University Press, Oxford) 1997, p. 150.
[24] BRINDLEY G. W. and BROWN G., *Crystal Structure of Clay Minerals and Their X-ray Identification* (Mineralogical Society, London) 1980.
[25] DA SILVA G. J., FOSSUM J. O., DIMASI E. and MÅLØY K. J., *Phys. Rev. B*, **67** (2003) 094114.
[26] WANG B. X. and ZHAO X. P., *J. Mater. Chem.*, **12** (2002) 1865.
[27] DA SILVA G. J., FOSSUM J. O., DIMASI E., MÅLØY K. J. and LUTNÆS S. B., *Phys. Rev. E*, **66** (2002) 011303.
[28] HAO T., *Adv. Colloid Interface Sci.*, **97** (2002) 1.
[29] MÉHEUST Y., PARMAR K. P. S., FOSSUM J. O., KNUDSEN K. D., MÅLØY K. J. and FONSECA D. M., *Orientational distribution of nano-layered clay particles inside electrorheological chains —a Waxs study* (2006), preprint.
[30] MAIER W. and SAUPE A., *Z. Naturforsch. A*, **13** (1958) 564.
[31] MAIER W. and SAUPE A., *Z. Naturforsch. A*, **14** (1959) 882.
[32] MÉHEUST Y., KNUDSEN K. and FOSSUM J. O., *Inferring orientation distributions in anisotropic powders of nano-layered crystallites from a single 2D WAXS image* (2005), preprint submitted to *J. Appl. Cryst.*
[33] GANDHI M. V. and THOMPSON B. S., *Smart Materials and Structures* (Kluwer Academic Publishers, Dordrecht) 1992.

Paper 2

The porous space inside bundles of polarized phyllo-silicate crystallites – A SAXS study

Kanak P. S. Parmar,[a]* Yves Méheust,[a] Jon O. Fossum,[a]* Kenneth D. Knudsen[b] and Davi de Miranda Fonseca[a]

[a]Physics Department, Norwegian University of Science and Technology (NTNU), Norway, [b]Physics Department, Institute for Energy Technology (IFE), Kjeller, Norway. E-mail: kanak.parmar@ntnu.no, jon.fossum@ntnu.no

When submitted to a strong electric field, crystallites of Na-fluorohectorite clay suspended in a silicon oil acquire an induced electric dipole. Their subsequent interactions lead to aggregation into chain-like structures parallel to the applied electric field. We have used Small Angle X-Ray scattering to get insight into the geometry of the porous medium in these structures. The 2D SAXS images exhibit a marked anisotropy, which is analyzed by fitting ellipses to iso-intensity lines. This also provides principal directions along which one-dimensionl spectra are computed. They display several power law behaviors, typical of porous media, separated by crossovers. The values for the power law exponents indicate that surface scattering is dominant, while the crossovers provide typical length scales for the clay particle bundles. The corresponding "picture" of the particle assembly inside the bundles complements that inferred from WAXS data in a previous study.

1. Introduction

Colloidal suspensions consisting of small particles of dielectric constant and/or conductivity higher than that of the surrounding liquid undergo a dramatic meso-structural change when submitted to a strong external electric field (of the order of kV/mm): the dielectric particles polarize, and the resulting induced electric dipoles interact with each other, leading to an aggregation of the particles into chain/bundle-like structures parallel to the direction of the external electric field. (Gast & Zukowski, 1989; Halsey, 1992). Consequently, application of the electric field leads to an important change in the suspensions' rheology (Tao, 1992; Davis, 1992; Anderson, 1994), which is why they are called *electro-rheological (ER) fluids* (Hao, 2001). The potential applications of this property are numerous (Halsey, 1992; Hao, 2001).

The formation of the ER structures and the subsequent rheological properties (in particular the yield shear stress) are controlled by several factors, including concentrations (Martin *et al.*, 1998), size distributions of particles (Ota & Miyamoto, 1994), field frequency (Wu & Conrad, 1998; Wen *et al.*, 2000), and dielectric mismatch between the particles and the surrounding fluid. Among the fluids that have been shown to be electro-rheological, suspensions of clay particles in an insulating fluid have only been addressed recently (Wang & Zhao, 2002; Fossum *et al.*, 2006). In particular, suspensions of fluorohectorite clay crystallites in a low conductivity silicon oil have exhibited a strong electro-rheological behavior (Fossum *et al.*, 2006). A wide-angle X- ray scattering (WAXS) study of the ER bundles has demonstrated the clay particles' preferred orientations inside the bundles, and shown that they polarize along their silica sheets (Fossum *et al.*, 2006).

Fluorohectorite is a synthetic 2:1 clay whose crystallites consist of a stack of $\sim$ 100 one-nm-thick clay platelets (da Silva *et al.*, 2002). This nano-layered nature makes WAXS a very convenient tool to study any type of poly-crystalline sample of this material, either in a dry- or in a suspended form. For the purpose of the present article, however, it is sufficient to know that these stacks remain quasi-two-dimensional in nature, as the lateral dimensions may be as much as 200 times the particle thickness. The particular way these very anistropic crystallites organize with respect to one another, i.e., their positional and orientational order, determines the morphology of the porous medium in the ER structures. In the present study, we use SAXS to investigate the geometry of this porous medium. In the particular case of Na-fluorohectorite samples, we discuss what type of information we can obtain from SAXS data on such systems.

The paper is structured as follows: section 2 addresses the features of small-angle scattering spectra expected from a meso-porous medium; section 3 contains a description of the experiments and their results; section 4 is the discussion; we conclude in section 5.

2. Small-angle scattering in a porous medium

Small angle scattering profiles recorded from meso-porous media often exhibit power laws over a wide q range. This has been observed in particular for aggregates of colloids (Dietler *et al.*, 1986; Schaefer & Keefer, 1986; Vacher *et al.*, 1988), carbons (Calo & Hall, 2004) and various types of rocks (Bale & Schmidt, 1984; Wong & Lin, 1986; Mildner *et al.*, 1986; Lucido *et al.*, 1988; Radlinski *et al.*, 1996). Such power law scattering curves have been explained in terms of fractal properties of the diffracting medium, from models in which aggregated particles (for example, ruguous spheres) form a porous medium with geometrical properties that relate to the concept of fractals. Except for the anisotropy of the clay particles, the porous medium consisting of aggregated clay particles that we consider here certainly bears similarities to those models, and will be studied in this framework. Here, it is important to distinguish betwen mass and surface fractals (Schmidt, 1989):

If we consider systems in which the aggregated particles are positioned with respect to one another so that their two-point correlation function is a power law function in the form

$$g(r) \propto r^{D_m-3}\,, \tag{1}$$

where D_m is a fractal dimension, a power law scattering curve with an exponent $-D_m$ is observed for q values in the range $1/l \ll q \ll 1/a$. Here a is the typical size of an aggregated particle, and l is the size of the whole system, i.e., the largest accessible length scale (Sinha *et al.*, 1984; Schmidt, 1989). Since by definition D_m is in the range $]1;3]$, the exponent observed in the scattering data is in the range $[-3;-1[$

If we now probe length scales smaller than the particle size, the scattering becomes sensitive to the roughness of the aggregates particles. If this roughness qualifies the particle for being considered a *surface fractal* with a dimension D_s, or more generally if the area of the surface is a power law of its linear size with an exponent D_s on a given range of length scales, then the scattering profiles exhibit a power law behavior with an exponent $-(6-D_s)$ on that range of length scales (Bale & Schmidt, 1984; Schmidt, 1989). Here by definition D_s is in the range $[2;3[$, and the scattering curve exponent is in the range $[-4;-3[$, with the well-known Porod law limit (-4) being that observed for smooth particles (Porod, 1951).

Therefore, in such systems of aggregated rough particles, two power law behaviors are observed, one with an exponent between -4 and -3 at large q values, and one with an exponent between -3 and -1

IUCr macros version 2.0β15: 200/05/19

at intermediate q values corresponding to length scales larger than the particle size. The scattering properties of porous media possessing long range correlations in their mass geometry or in the roughness of their pores are generally investigated in this framework as well, and fitted to a power law model in the form

$$I(q) = A\, q^{-D} + B\,, \tag{2}$$

in which B is the incoherent background scattering. However, the understanding of such data is more difficult in the presence of a polydispersity of the aggregated particles, or, equivalently, of a wide distribution for the pore sizes. In this case, an exponent $D > 3$ can arise both from surface scattering form rough pore walls, or from bulk scattering from a porous media with a wide pore size distribution (Pfeifer & Avnir, 1983).

In the case of the anisotropic clay particles, which have two characteristic length scales instead of one, experiments are often carried out in an intermediate q range corresponding to length scales intermediate between the typical particle thickness and the typical particle width. It is the case in the experiments presented here.

3. Experiments

3.1. Experimental method

Synthetic sodium fluorohectorite, with chemical formula $Na_{0.6}(Mg_{2.6}\ Li_{0.6})\ Si_4\ O_{10}\ F_2$ per unit cell (where Na is an interlayer exchangeable cation) was purchased form Corning Inc.(New York) in powder form. The powder was further cation-exchanged in order to saturate the crystallites' nano-pores with Na^+ cations: NaCl salt was dissolved in distilled water and added in an amount approximately five times the cation exchange capacity (Kaviratna *et al.*, 1996), to promote saturation. After thorough mixing, the clay was dialyzed against distilled water until a negative chloride test was obtained. After dialysis, the samples were dried out and grinded into powder form. A suspension of 3 % (w/w) was then prepared by directly mixing the chosen amount of clay powder with Rothiterm silicone oil in sealed glass tubes at ambient temperature. Finally, the mixture was shaken vigorously for 15 min, and subsequently left to rest.

The synchrotron SAXS experiments were performed using the supernatant of the suspension in a custom-made scattering cell. The scattering cell consists of an insulating plastic material, whose top part was open, while both the (front and back) sides and the bottom part were closed by gluing a standard kapton film. Two parallel and identical 1/2 mm thick copper electrodes separated by a gap of 2 mm were inserted from the top of the sample cell. The sample to be studied (< 2 ml) was placed between the electrodes from the top part. After application of an electric potential difference (2 kV) between these copper electrodes, the clay particles were first observed to form chain-like structures parallel to the applied electric field. The chains were subsequently observed to collapse, forming stable chain bundles in about 10 sec. Fig. 1(a) shows one such structure.

SAXS experiments were carried out under ambient temperature at beamline BM-26B of the European Synchrotron Radiation Facility (ESRF), in Grenoble (France), using a wavelength $\lambda = 1.24$ Å. Scattered X-rays were recorded on a 2-dimensional detector (a square matrix of 512×512 elements) positioned $\sim$ 8000 mm away from the sample; the exposure time was 600 s. The experimental geometry is shown in Fig. 2; the ER bundles were lying on average horizontally. In what follows, we shall refer to the corresponding axis of the SAXS images as the horizontal direction, while the perpendicular one shall be denoted as the vertical direction. This experimental setup allowed obtention of SAXS data on a range of momentum transfer values between $q_{\min} = 0.001\ \mathrm{nm}^{-1}$ and $q_{\max} = 0.15\ \mathrm{nm}^{-1}$.

3.2. Data analysis

3.2.1. Method The raw 2-dimensional SAXS patterns obtained from the bundle structures are clearly anisotropic. The iso-intensity lines are roughly homothetic and resemble ellipses that have their major axis lying approximately vertical, and their minor axis lying approximately horizontal (see the white elliptic ring in Fig. 3). We first analyzed the 2-dimensional SAXS images using a custom-made image analysis software. Ellipses were fitted to iso-intensity lines for each SAXS pattern; the principal axes (direction and length) were computed, and an eccentricity $e = \sqrt{1-(b/a)^2}$, where a and b are the long and short axes of the fitted ellipse, respectively, was determined. This eccentricity accounts for the anisotropy of the image. An average eccentricity value for the Na-FH system was computed from images recorded from identical samples; this allowed us to reduce the variations arising from the noise in the data (see Table 1).

For further analysis, each SAXS pattern was corrected for detector sensitivity and background by subtracting from the image data an image of the empty cell. Besides, the sample to detector distance was calibrated using the fiber diffraction of wet rat-tail collagen, which has strong characteristic peaks at $q = 2\pi\, n/67.2\ \mathrm{nm}^{-1}$ ($n = 1, 3, 5$).

We then computed one-dimensional profiles of X-ray intensity $I(q)$ versus scattering vector q along the principal axes of the ellipses, as obtained previously. Those directions are respectively nearly parallel to the horizontal (i.e, the direction of the applied electric field) and the vertical directions. The profiles were obtained by averaging the 2-dimensional images over azimuthal angles, in $\pm 5°$-wide sectors around those two directions. Log-log plots of those profiles appear to consist of linear segments, which means that different power laws in the form of Eq. (2) are observed on different q-ranges. Fig. 4 illustrates this behavior, for profiles recorded both along the minor axis and along the major axis. The length scales corresponding to the crossover q-values are characteristic of the system, but since no peak is observed at these q-values, they do not correspond to a regular periodicity within the clay assembly.

For intensity profiles recorded along the horizontal direction (plot denoted (1) in Fig. 4), three different q-ranges are clearly visible, on which three power laws can be fitted. The crossover q values were first estimated visually, with an uncertainty; they are listed as $q_{\|i}(i = 1, 2)$ in Table 1, the index i being incremented as one moves from larger to lower q-values. Straight lines were fitted to the linear segments in the log-log plots; they are shown in Fig. 4 while the corresponding power law exponents $D_{\|i}(i = 1, 2, 3)$ (same convention on the index i as for the q_is) are listed together in Table 1.

For intensity profiles recorded along the vertical direction (plot denoted (2) in Fig. 4), we also distinguish three regimes. The crossovers $q_{\perp 1}$ is determined visually. It is somewhat more difficult to determine than along the horizontal axis. The crossovers $q_{\perp 2}$ is chosen equal to $q_{\|2}$ (see section 3.2.2). The fitted values of the exponents D differ enough from each other on the adjacent ranges (see $D_{\perp i}(i = 1, 2, 3)$ values in Table 1) to confirm the existence of two crossovers. As explained above for the ellipse eccentricity values, the values for the exponents D listed in Table 1 are obtained from averaging over 7 images recorded on identical samples.

3.2.2. Results and discussion The minor axes of the ellipses fitted to the 2D SAXS images are close to horizontal. This shows that the apparent size of the clay particles along that direction, as probed by X-rays, is larger along that horizontal direction – also the direction

of the electric field – than along the vertical direction. Since the clay particles are platelets with a thickness much smaller than their lateral dimension, this suggests that they are lying in the ER bundles with one of their lateral dimensions parallel to the field; i. e., on average, the clay particles have their directors aligned perpendicular to the direction of applied field. Whether the directors are aligned with each other along a particular direction perpendicular to that of the applied field, or whether they are distributed in the vertical plane that contains the incoming beam, cannot be inferred directly from the SAXS data alone.

In a recent study, we investigated the same electro-rheological bundles using X-ray diffraction (i.e., wide angle X-ray scattering, or WAXS) (Fossum *et al.*, 2006). Taking advantage of the nano-layered nature of the clay crystallites, we were able to infer particle orientations inside the particle bundles from the anisotropy of two-dimensional WAXS images (see (Méheust *et al.*, 2006) for a description of the method). This study suggested that the particles polarize along their silica sheets (see Fig. 1(c)), and hence, that their directors were, on average, perpendicular to the direction of the electric field. Our SAXS data is consistent with these previous findings (see second paragraph of section 3.2.2). In Figure 1(b), we present a 2D sketch of an aggregate inside the particle assembly, as inferred from the study in (Fossum *et al.*, 2006) and from the current SAXS study. In such an aggregate, due to the particles' quasi-2D nature, they are on average all parallel to a mean planar orientation. The total 3D assembly has to be understood as a combination of such aggregates, in which the possible mean planar orientations for the aggregates contain the direction of the electric field (i.e., the direction of the red arrow in Fig. 3(c)) and are random otherwise. Consequently, the whole structure remains statistically unchanged by rotations around the direction of the electric field.

In terms of intensity profiles along the principal axes of the 2D SAXS images, the results can be understood as follows:

1. Along the minor axis (horizontal direction), the two crossover q values denote characteristic scales for the system: the larger one, $l_{\|2}$, (see Fig. 4, plot (1), and Table 1) is a typical particle extension/width, while the smaller one, $l_{\|1}$, can be understood as a typical pore size between aggregated clay particles, along the direction of the external electric field. Therefore, $l_{\|1}$ is controlled by the particles' sizes and their relative orientations/positioning, while $l_{\|2}$ is less dependent on the particular arrangement of the particles with respect to each other (provided they are aligned with the electric field). Those two typical length scales are indicated in Fig. 1(b); due to the particle polydispersity, they must be understood as average values and do not correspond to a true regular structure of the assembly. Such a regular structure would probably result in a correlation peak in the scattering data, which is not visible here.
2. Along the major axis (vertical direction, perpendicular to the electric field), due to the axial symmetry of the particle population around the direction of the electric field, some of the platelet-shaped particles present their width to the beam, and others present their top/bottom surfaces, so that both the particle- thickness and width should be visible on the scattering profiles. This is why we have choosen $q_{\perp 2} = q_{\|2}$, interpreted as a the typical particle width. At small length scales, the relevant characteristic length scales are the typical particle thickness d (see Fig. 1(b)), the typical pore size $l_{\|1}$ as discussed above, and a typical pore size normal to the mean plane of an aggregate (vertical direction in Fig. 1(b)). We believe that these three length scales are close to each other, and are therefore not visible as distinct crossovers in the intensity profiles (see Fig. 1(b)). Thus, we have defined visually from plot (2) a crossover, with a value indeed close to that found for $l_{\|1}$ in plot (1) (see Table 1).
3. By changing q, we probe the system at different scales: for $q > q_1$ (in the two directions), we probe the properties of the individual particles; at smaller q values, we probe the properties of the porous space between the particles, or of aggregates of particles. As summarized in section 2, the values of the exponents D for the fitted power laws denote long range correlations in the inner surfaces (if $3 < D < 4$) or bulk arrangement (if $2 < D < 3$) of the porous medium. For $q > q_1$ (see D_1 values in Table 1, in the two directions), we expect the exponent to be controlled by the surface roughness of the particles. This is what is observed here. The other exponents are also greater than 3 in absolute value, which indicates a predominant surface scattering, at all scales probed by the experiment. Note that due to the axial symmetry discussed above, the exponent observed in Fig.4, plot (1), in the large q range, is probably determined by the scattering properties of the lateral surfaces of the clay particles, while the exponent found in plot (2) of the same figure, in the same range of q values, results from a mixed scattering by the lateral- and the top/bottom surfaces of the platelet-shaped scatterers. This is why two different exponents are observed, although at those length scales smaller than the particle thickness the difference in meso-porous arrangement arising from the particles' anisotropy plays no role.

The geometry studied here has similarities with that observed for dry-pressed samples, in which all particles have their flat surfaces parallel on average, in a nematic-like arrangement. Namely, we have inferred a geometric description in which the overall assembly possesses a statistical axial symmetry around the direction of the applied electric field, but consists of aggregates (like that sketched in Fig. 1(b)) with a nematic-like arrangement. Such nematic arrangements were previously studied using small angle neutron scattering (SANS) for Na-fluorohectorite samples, by Knudsen et al. (Knudsen *et al.*, 2004). In those samples, which were dehydrated under a uniaxial load of 0.12 MPa and 2.60 MPa, and in which clay particles are expected to be much more densily packed than in the electro-rheological bundles addressed in the present paper, the authors inferred a correlation length for the porous medium in the direction of the applied load, and one along the average plane of the clay particles. These correlation lengths can be related to typical pore sizes in the two directions, and were observed to be 2 times larger along the particle planes than in the direction of the load, probably due to the particles' aspect ratio and the dense packing. In the present system, no typical pore size is observed at length scales significantly different from the typical pore size $l_{\perp 1}$. I. e., in aggregates like that pictured in Fig. 1(b), the typical pore size normal to the aggregate's mean plane is similar to the pore size along that plane; this indicates a looser packing.

4. Conclusion

Small-angle X-ray scattering is a useful tool when investigating the mesoporous organization of poly-crystalline systems of platelet-shaped scatterers with a lateral size in the micron range and a thickness $10-20$ times smaller. In this article, we have shown that anisotropic 2D SAXS images recorded from electro-rheological bundles of fluorohectorite clay particles can be analyzed in order to obtain a geometrical characterization of an assembly of clay particles aggregated after being polarized by an electric field. Fitting ellipses to iso-intensity lines of the images allowed to determine the overall alignment of the particle, which is parallel to the field (as shown by a previous WAXS study), and to estimate the preferential orientation of the particles. Scattering

profiles recorded along the azimuthal directions parallel to and perpendicular to the applied electric field exhibit several power law regimes, with crossover scales between them that correspond to typical length scales of the particle assembly. The exponents of the power laws are in the range usually attributed to surface scattering with a correlated roughness.

This study opens many prospects. Firstly, we plan to widen the available q range through SALS- and further SAXS experiments, in order to obtain power law exponents on a wider range and with a better confidence on the fitted exponents. Secondly, we plan to study the influence of the intercalated cation on the overall collective behavior of the clay particles in an electric field, by studying different X-fluorohectorite samples (X being the intercalated cation). Thirdly, we want to relate the measured ellipse eccentricity to the orientation density probability function of the population of platelets, as done in a recent study (van der Beek *et al.*, 2006) in which an identical geometry was addressed for magnetically-oriented Gibbsite particles

The staff at the DUBBLE beamline at ESRF is gratefully acknowledged for support during the SAXS experiments. This work was supported by the Research Council of Norway (RCN) through a Strategical University Program and through the Nanomat Program: RCN projects 152426/431, 154059/420, 148865/432, and 138368/V30 and SUP154059/420.

References

Anderson, R. A. (1994). *Langmuir*, **10**, 2917.

Bale, H. D. & Schmidt, P. W. (1984). *Phys. Rev. Lett.* **53**, 596.

van der Beek, D., Petukhov, A. V., Davidson, P., Ferré, J., Jamet, J. P., Wensink, H. H., Vroege, G. J., Bras, W. & Lekkerkerker, H. N. W. (2006). *Phys. Rev . E*, **73**, 041402.

Calo, J. M. & Hall, P. J. (2004). *Carbon*, **42**, 1299–1304.

da Silva, G. J., Fossum, J. O. & DiMasi, E. (2002). *Phys. Rev. E*, **66**(1), 011303.

Davis, L. C. (1992). *Appl. Phys. Lett.* **60**, 319.

Dietler, G., Aubert, C. & Cannell, D. S. (1986). *Phys. Rev. Lett.* **57**, 3117.

Fossum, J. O., Méheust, Y., Parmar, K. P. S., Knudsen, K. & Måløy, K. J. (2006). *Europhys. Lett.* **74**(3), 438–444.

Gast, A. P. & Zukowski, C. F. (1989). *Adv. Colloid Interface Sci.* **30**, 153–202.

Halsey, T. C. (1992). *Science*, **258**, 761–766.

Hao, T. (2001). *Adv. Mater.* **13**, 1847.

Kaviratna, P. D., Pinnavaia, T. J. & Schroeder, P. A. (1996). *J. Phys. Chem. Solids*, **57**, 1897.

Knudsen, K. D., Fossum, J. O., Helgesen, G. & Haakestad, M. W. (2004). *Physica B*, **352**(1-4), 247–258.

Lucido, G., Triolo, R. & Caponetti, E. (1988). *Phys. Rev. B*, **38**(13), 9031–9034.

Martin, J., Anderson, R. & Tigges, C. (1998). *J. Chem. Phys.* **108**, 3765.

Méheust, Y., Knudsen, K. & Fossum, J. O. (2006). *J. Appl. Cryst.* Accepted.

Mildner, D. F. R., Rezvani, R., Hall, P. L. & Borst, R. L. (1986). *Appl. Phys. Lett.* **48**(19), 1314–1316.

Ota, M. & Miyamoto, T. (1994). *J. Appl. Phys.* **76**, 5528.

Pfeifer, P. & Avnir, D. (1983). *J. Chem. Phys.* **79**, 3558–3565.

Porod, G. (1951). *Kolloid Z*, **124**, 93–94.

Radlinski, A. P., Boreham, C. J., Wignall, G. D. & Lin, J.-S. (1996). *Phys. Rev. B*, **53**(21), 14152–14159.

Schaefer, D. W. & Keefer, K. D. (1986). *Phys. Rev. Lett.* **56**, 2199.

Schmidt, P. W. (1989). In *The fractal approach to heterogeneous chemistry*, edited by D. Avnir, pp. 67–79. John Wiley & Son Ltd.

Sinha, S. K., Freltoft, T. & Kjems, J. K. (1984). In *Kinetics of Aggregation and Gelation*, edited by F. Family & D. P. Landau, pp. 87–90. Elsevier, Amsterdam.

Tao, R. (ed.) (1992). *International Conference on Electrorheological Fluids: Mechamism , Properties, Structure, Technology and Application*. World Scientific Singapore.

Vacher, R., Woigner, T., Pelous, J. & Courtens, E. (1988). *Phys. Rev. B*, **37**, 6500.

Wang, B. X. & Zhao, X. P. (2002). *J. Mat. Chem.* **12**, 1865–1869.

Wen, W., Ma, H., Tam, W. & Sheng, P. (2000). *Appl. Phys. Lett.* **77**, 3821.

Wong, P.-Z. andHoward, J. & Lin, J.-S. (1986). *Phys. Rev. Lett.* **57**, 637.

Wu, C. W. & Conrad, H. (1998). *J. Appl. Phys.* **83**, 3880.

Table 1
Calculated fit parameters: (i) average eccentricities e of the 2-dimensional scattering patterns, and (ii) power law scattering exponents D_i ($i = 1, 2, 3$) and crossover q_1 and q_2 in the scattering profiles recorded along the minor axis (Fig. 4, plot (1)).

E (V/mm)	1000
N° of images per curve	7
e	0.54
Crossover $q_{\parallel 1}$ (nm^{-1})	0.086 ± 0.03
Crossover $l_{\parallel 1}$ (nm)	73 ± 3
Crossover $q_{\parallel 2} = q_{\perp 2}$ (nm^{-1})	0.025 ± 0.003
Crossover $l_{\parallel 2} = l_{\perp 2}$ (nm)	251 ± 25
Crossover $q_{\perp 1}$ (nm^{-1})	0.090 ± 0.005
Crossover $l_{\perp 1}$ (nm)	70 ± 4
$D_{\parallel 1}$	-3.44 ± 0.05
$D_{\parallel 2}$	-3.02 ± 0.05
$D_{\parallel 3}$	-3.38 ± 0.05
$D_{\perp 1}$	-3.38 ± 0.05
$D_{\perp 2}$	-3.21 ± 0.05
$D_{\perp 3}$	-3.67 ± 0.05

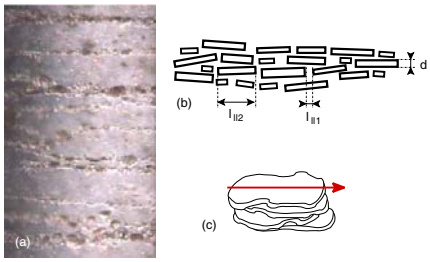

Figure 1
(a) Stable electro-rheological structures of sodium(Na)-fluorohectorite clay particles in silicone oil and under application of an external horizontal DC electric field = 1 kV/mm. – (b) 2D sketch of a nematic aggregate of clay particles inside an ER bundle; the direction of the external electric field is horizontal; the platelet-shaped clay particles are horizontal on average in this particular aggregate; many such aggregates, possessing various orientations around the direction of the electric field, form the overall particle bundle. –(c) Sketch of a nano-stacked clay particle in the arrangement shown in (b); the arrow indicates the direction of the electric dipole induced in the particle, which, on average, coincides with that of the external electric field.

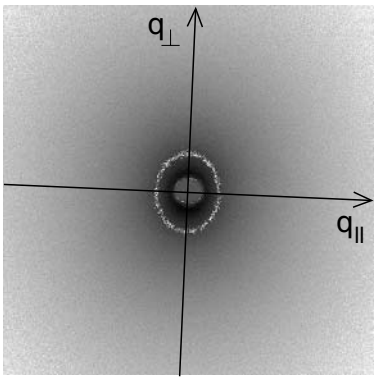

Figure 3
A two-dimensional anisotropic scattering pattern obtained from a Na-Fluorohectorite sample of 3.0% (w/w), at $E = 1.0$ kV/mm. The gray color scale is logarithmic. An iso-intensity line is colored white to emphasize the anisotropy of the image.

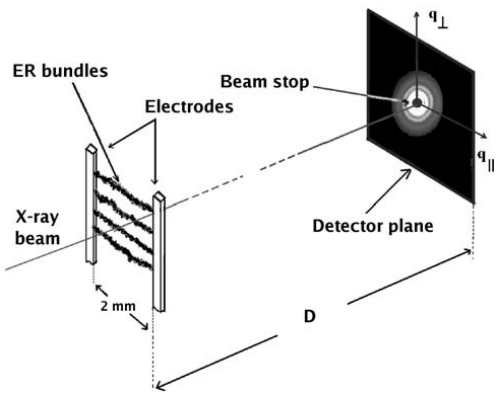

Figure 2
Experimental setup to record SAXS data from electro-rheological bundles of polarized particles in oil. The camera length is $D \sim 8$ m.

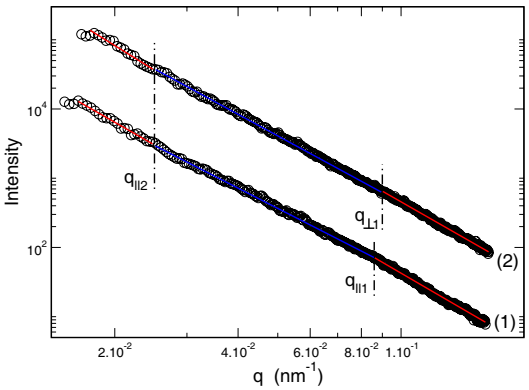

Figure 4
Log-Log plot of the intensity of the scattering profiles recorded along (1) the horizontal direction, i. e., the direction of the applied electric field, and (2) the vertical direction.

Paper 3

Packing and voids in electro-rheological structures of polarized clay particles

K. P. S. Parmar [a)], Y. Méheust, and J. O. Fossum[a)]
Physics Department, Norwegian University of Science and Technology (NTNU), Trondheim, Norway

K. D. Knudsen
Physics Department, Institute for Energy Technology (IFE), Kjeller (Norway)

D. M. Fonseca
Physics Department, Norwegian University of Science and Technology (NTNU), Trondheim, Norway

Oil suspensions of fluorohectorite clay particles exhibit a dramatic meso-structural ordering when submitted to a strong electric field. This is due to dipolar interaction between polarized fluorohectorite particles, which orientate and aggregate to forms chains and/or bundle-like structures along the direction of applied electric field. We have used synchrotron small angle X-ray scattering to get insight into the nature of the porous medium in the bundles. Three types of fluorohectorite clay samples corresponding to three different intercalated cations Na^{+}, Ni^{2+} and Fe^{3+} were studied. The two-dimensional SAXS images from bundles of fluorohectorites exhibit a marked anisotropy which is analyzed by fitting ellipses to iso-intensity lines of SAXS patterns. This also provides principal directions along which one-dimensional spectra are computed. They display a power law behavior typical of porous media, separated by crossovers. The crossovers are interpreted in terms of typical length scales for the clay particle bundles, providing for the first time a quantitative image of the 3D geometry inside such bundles of polarized clay particles. The exponents of the power laws indicate either predominant surface- (for 2 types of samples) or bulk- (for the last type) scattering, at all length scales investigated.

I. INTRODUCTION

The rheological properties (viscosity, yield stress, shear modulus etc.) of colloidal suspensions consisting of small particles of dielectric constant and/ or conductivity[1–3] higher than that of the surrounding liquid can be controlled by an external electric field. Such suspensions are known as electrorheological (ER) fluids[4, 5]. The applied electric field (of the order of kV/mm) results in induced dipoles in the particles. Consequently, the particles undergo positional and orientational alignment to minimize dipole interaction energy, which results in their aggregation into chain/bundle-like structures, parallel to the direction of applied electric field[6–10].

The study of the structure formation of ER fluids has attracted increasing interest in recent years for its fundamental and technological importance. It has been shown that microcrystalline structures inside the bundles of spherical particles are a body-centered tetragonal (bct) lattice[11–13]. This provides a new technique to form mesocrystals with unique photonic properties[14-15]. The details of the structure formation in ER fluids depend on several factors, such as concentrations[16], size distributions of particles[17], field frequency[18-19] etc. The influence of the dielectric constant or conductivity of particles is another interesting topic since the dielectric and conductivity mismatch between the particles and the liquid is widely accepted as the main cause of the ER phenomenon. The yield stress of an ER fluid is a critical parameter that governs the numerous potential applications of such a fluid. Besides the other experimental parameters, it depends upon the internal close packing of the particles density[20].

In this paper, we address ER fluids consisting of 2:1 clay particles suspended in silicone oil. Among the large variety of clay minerals, 2:1 clays have been investigated

for potential applications such as nanocomposites, catalysts, cosmetics and pharmaceuticals etc., and applications where their unique bonding, suspending or gellant properties are required. The basic physical structural unit of a 2:1 clay is a platelet (about 1 nm thick) made of one aluminum or magnesium hydroxide octahedral sheet sandwiched between two inverted tetrahedral silica sheets. The isomorphic substitutions in the octahedral and or tetrahedral sheets by less charged cations generate a net negative layer charge on the platelet[21]. To balance this structural layer charge, individual platelets tend to stack by sharing intercalated (possibly hydrated) cations. The structural charge on the platelets of 2:1 varies from 0.4 to 1.2 e- per unit cell[22]. This moderate platelet charge results in physical and chemical properties that are unique and not found in other clay minerals.

Fluorohectorite is a synthetic 2:1 clay that has one of the largest values for the particle diameter, up to about 10 μm, and a layer charge of 1.2 e^- per unit cell, which is very large in comparison to that of other synthetic 2:1 such as laponite (0.4 e^- per unit cell)[23]. This high surface charge leads to a very robust stacking of the fluorohectorite platelets, resulting in fluorohectorite particles effectively consisting of ~ 100 stacked platelets[24-25]. Those particles (or grains) are ~0.1 μm-thick; they remain quasi-two-dimensional in nature, as the lateral dimensions may be as much as 200 times the particle thickness. However, fluorohectorite is polydisperse with a wide distribution in lateral sizes, so that this ratio is not fixed, and may be considerably lower for other grains.

Colloidal suspensions of fluorohectorite particles dispersed in a low conductivity silicone oil have been shown to exhibit a dramatic electro-rheological behavior[26]. A wide-angle X- ray scattering (WAXS) study of the ER bundles has demonstrated the clay particles' preferred orientations inside the bundles, and shown that they polarize

along their silica sheets[26]. The particular way the anisotropic clay particles organize in the bundle with respect to one another i.e., their positional and orientational order, determines the morphology of the porous medium in-between the aggregated particles.

Small angle X-ray scattering (SAXS) and small angle neutron scattering (SANS) are techniques commonly used to study the mesoscopic structural arrangement of soft matter. In particular, they have proved very useful in the study of systems of clay mineral particles in aqueous media, for which a variety of structures/properties under different preparation conditions have been demonstrated, such as spontaneous ordering, aggregation, gelation and thixotropy behavior[27–30]. In this paper we have used SAXS to study the electrorheological bundles of clay particles in silicone oil in order to get insight into the nature of the porous medium in between the clay particles that make up the chain bundles.

Following this introduction, the paper is structured as follows: section 2 addresses the features of small-angle scattering spectra expected from a meso-porous medium; section 3 contains a description of the experiments and a discussion of their results; we conclude in section 4.

II. SMALL-ANGLE SCATTERING IN A POROUS MEDIUM

The fluorohectorite particles consist of stacks of 1 nm- thick platelets with a thickness ~100 nm and a lateral extension between 200 nm and 2 μm. X-ray diffraction from the stacked structure is classically used to determine the platelet separation of such nano-stacks[31-32], and their thickness. More recently, it has been used to infer particle orientation distributions in poly-crystalline samples of these nano-stacks[33]. Besides wide angle diffraction (WAXS), the dimensions of the clay particles make small angle

scattering a suitable tool when it comes to studying the collective behavior/organization of these clay particles.

Small-angle scattering is a useful tool to study disordered structures and porous media[34–43]. In a small angle X-ray scattering (SAXS) experiment, the dependence of the scattered intensity on the scattering angle 2θ is controlled by the size of the colloidal particles, their tendency to aggregate, the porosity of the disperse system, the magnitude of the specific surface area, and more generally, by the inhomogeneties characterizing the structure of the disperse system[44-45]. In the Born approximation, the scattered intensity $I(q)$, as a function of the momentum transfer vector q

$$q = \frac{4\pi}{\lambda}\sin\left(\frac{2\theta}{2}\right) \tag{1}$$

where λ is the wavelength of the incident beam and 2θ is the scattering angle, is simply proportional to the Fourier transform of the geometric correlation function of the electron density.

For porous media, the scattering profiles often exhibit power laws on a wide q-range. This has been observed in particular for aggregates of colloids[36–38], carbons[46] and various types of rocks[44-45, 47–49]. Such power law scattering curves have been explained in terms of fractal properties of the diffracting medium, from models in which aggregated particles (for example, ruguous spheres) form a porous medium with geometrical properties that relate to the concept of fractals. Here, it is important to distinguish between mass and surface fractals[50].

If we consider mass fractals, or more generally systems in which the aggregated particles are positioned with respect to one another so that their two-point correlation function is a power law function in the form

$$I(q) = Aq^{-D} + B \tag{3}$$

where A is a scaling factor and B is the incoherent background scattering. However, the understanding of such data is more difficult in the presence of a polydispersity of the aggregated particles, or, equivalently, of a wide distribution for the pore sizes. In this case, an exponent (in absolute value) $D > 3$ can arise both from surface scattering form rough pore walls, or from bulk scattering from a porous media with a wide pore size distribution[51].

III. EXPERIMENTS

III.1. EXPERIMENTAL METHOD

Synthetic sodium fluorohectorite, with a chemical formula $Na_{0.6}(Mg_{2.6}\ Li_{0.6})\ Si_4\ O_{10}\ F_2$ per unit cell (where Na is an interlayer exchangeable cation) was purchased form Corning Inc. (New York) in powder form. Three fluorohectorite clay powders, with different intercalated cations, sodium (Na^+), nickel (Ni^{2+}) and iron (Fe^{3+}), were prepared through an ion exchange method: the corresponding cation salts were dissolved in distilled water and added in an amount approximately five times the cation exchange capacity in order to promote saturation. After thorough mixing, three fluorohectorite clays were dialyzed against distilled water until a negative chloride test was obtained. After dialysis, the three fluorohectorite clays were dried out and grinded in powder form. Suspensions at 3 % (w/w) were then prepared by directly mixing the chosen amount of clay powder with Rothiterm silicone oil in sealed glass tubes at ambient

temperature. Finally, the mixtures were shaken vigorously for 15 min, and subsequently left to rest.

The synchrotron SAXS experiments were performed using the supernatant of these suspensions in a custom-made scattering cell. The scattering cell was made of an insulating plastic material, whose top part was open and both the (front and back) sides and the bottom part were closed by gluing a standard thin (thickness, 0.08mm) kapton film. Two parallel and identical 1/2 mm-thick copper electrodes separated by a uniform gap of 2 mm were inserted from the top of the sample cell. The suspension to be studied (< 2 ml) was introduced between the electrodes from the top part. After application of an electric potential difference (2 kV) between these copper electrodes, the clay particles were first observed to form chain-like structures parallel to the applied electric field. The chains were subsequently observed to collapse, forming stable chains bundles in about 10 sec. Fig. 1 shows one such structure formed by iron (Fe^{3+}) - fluorohectorite clay particles.

SAXS experiments were carried out under ambient temperature at beamline BM-26B of the European Synchrotron Radiation Facility (ESRF), in Grenoble (France), using a wavelength λ = 1.24 Å. Scattered X- rays were recorded on a two-dimensional detector (a square matrix of 512×512 elements) positioned about 8000 mm away from the sample; the exposure time was 600 s. The experimental geometry is shown in Fig. 2: the ER bundles were lying on average horizontally. In what follows, we shall refer to the corresponding axis of the SAXS images as the horizontal, while the perpendicular one shall be denoted as the vertical direction. This experimental setup allowed SAXS data on a range of momentum transfer q-values between $q_{\min}$ = 0.01 nm^{-1} up to $q_{\max}$ = 0.15 nm^{-1}, corresponding to length scales $d_{\max} \sim 600$ nm and $d_{\min} \sim 40$ nm, respectively.

III.2. DATA ANALYSIS

III.2.1. METHOD

The raw two-dimensional SAXS patterns obtained from bundle structures for all the three samples – sodium (Na^{+}) fluorohectorite, nickel (Ni^{2+}) fluorohectorite and iron (Fe^{3+}) fluorohectorite are clearly anisotropic (see Fig. 3). The iso-intensity lines are roughly homothetic and resemble ellipses that would have their major axis lying approximately vertical, and their minor axis lying approximately horizontal. We first analyzed the two-dimensional SAXS images using a home-made image analysis software in Matlab. Ellipses were fitted to iso-intensity lines for each SAXS pattern; the principal axes (direction and length) were computed, and an eccentricity *e* defined as

$$e = \sqrt{1 - \frac{j^2}{k^2}} \quad , \tag{4}$$

where *j* and *k* are the long and short axes of the fitted ellipse, was determined. This eccentricity accounts for the anisotropy of the images. The eccentricity values obtained for each type of sample under an identical electric field are shown in Table 1. Those values are average values obtained from several images recorded from identical samples; this allowed us to account for the large variations arising from the noise in the data. For each eccentricity value in Table 1, the number of images used to calculate it, is also listed.

For further analysis, each SAXS pattern was corrected for detector sensitivity and background by subtracting from the image data an image data of the empty cell.

Besides, the sample to detector distance was calibrated using the fiber diffraction of wet rat-tail collagen, which has a strong characteristic peaks at $q = 2\pi n/67.2$ nm^{-1} (n = 1, 3, 5). We then computed one-dimensional profiles of X-ray intensity $I(q)$ versus scattering vector q along the principal axes of the ellipses, as obtained previously. Those directions are nearly parallel to the horizontal (i.e. the direction of the applied electric field) and the vertical directions, respectively. The profiles were obtained by averaging the two-dimensional images over azimuthal angles, in ± 5°- wide sectors around those two directions. Log-log plots of those profiles appear to consist of linear segments, which mean that different power laws in the form of Eq. (3) are observed on different q-ranges. Fig. 4 (a) and Fig. 4 (b) illustrate this behavior for profiles recorded along the minor- and the major- axis respectively.

For intensity profiles recorded along the horizontal direction (Fig. 4 (a)) three different q-ranges are clearly visible, on which three power laws can be fitted. The crossover q- values were first estimated visually, with an uncertainty; they are listed as $q_{\parallel \mathrm{i}}$ (i = 1, 2) in Table 1, the index i being incremented as one moves from larger to smaller q-values. Straight lines were fitted to the linear segments in the log-log plots; they are shown Fig. 4 (a) while the corresponding power law exponents $D_{\parallel \mathrm{i}}$ (i = 1, 2, 3) (same convention on the index i as for the q_is) are listed together in Table 1.

For intensity profiles recorded along the vertical direction (see Fig. 4(b)), we also distinguish three regimes, but the crossovers are somewhat more difficult to determine than along the horizontal axis. The crossovers $q_{\perp 1}$ are determined visually, and the crossovers $q_{\perp 2}$ are chosen equal to $q_{\parallel 2}$ (see section 3.2.2). The fitted values of the exponents D differ enough from each other on the adjacent ranges (see the $D_{\perp i}$, i = 1, 2 in Table 1) to confirm the existence of two crossovers. As explained above for the ellipse eccentricity values, the values for the exponents D listed in Table 1 are obtained

from averaging over 7 images recorded on identical samples. Note that no power law exponent was fitted on the low-q ranges in Fig.4(b), because the data range was not wide enough, and did not allow good enough confidence levels on the fits.

III.2.2. RESULTS AND DISCUSSIONS

Table 1 lists all results, both related to the eccentricities of the two-dimensional images and to power law exponents of one-dimensional scattering profiles.

The minor axis of the ellipses fitted to the two-dimensional SAXS images are close to horizontal. This shows that the apparent size of the clay particles along that direction, as probed by the X-ray, is larger along that horizontal direction – also the direction of the electric field – than along the vertical direction. Since the clay particles are platelets with a thickness much smaller than their lateral dimension, this suggests that they are lying in the ER bundles with one of their lateral dimensions parallel to the field; i.e., on average, the clay particles have their directors aligned perpendicular to the direction of applied field. The maximum eccentricity is seen for nickel (Ni) fluorohectorite (e = 0.61), and the minimum eccentricity for sodium (Na) fluorohectorite (e = 0.54). The difference is less than 12% (see Table 1). This means that, at equal electric field strength, the orientational order for the particles are of the same order of magnitude for all types of samples.

If all the particle directors were aligned with the vertical direction, the anisotropy of the SAXS pictures would be much larger than what is observed. Whether the directors are aligned with each other along another direction perpendicular to that of the applied field, or whether they are widely distributed (and possibly, uniformly) in the vertical

plane that contains the incoming beam, cannot be inferred directly from the SAXS data. In a recent study, however, we investigated the same electro-rheological bundles using X-ray diffraction (i.e., wide angle X-ray scattering, or WAXS)[26]. Taking advantage of the nano-layered nature of the clay crystallites, we were able to infer particle orientations inside the particle bundles from the anisotropy of two-dimensional WAXS images[33]. This study suggested that the particles polarize along their silica sheets (see Fig. 1(c)), and hence, that their directors were, on average, perpendicular to the direction of the electric field. Our SAXS data is consistent with these previous findings (see second paragraph of section 3.2.2). In Figure 1(b), we present a two-dimensional sketch of an aggregate inside the particle assembly, as inferred from the study in[26] and from the current SAXS study. In such an aggregate, due to the particles' quasi-two-dimensional nature, they are on average all parallel to a mean planar orientation. The total three-dimensional assembly has to be understood as a combination of such aggregates, in which the possible mean planar orientations for the aggregates contain the direction of the electric field and are random otherwise. Consequently, the whole structure remains statistically unchanged by rotations around the axis of the electric field. Figure 1(c) shows a cut of the same aggregate through a plane parallel to its mean plane and indicated by the red dashed line in Fig. 1(b). Figures 1(b) and (c) correspond to two configurations met by the X-ray beam and that contribute equivalently to the scattering profiles recorded along the vertical direction.

In terms of intensity profiles along the principal axes of the two-dimensional SAXS images, the results can be understood as follows:

Crossovers in the horizontal profiles: Along the minor axis (horizontal direction), the two crossover q-values denote characteristic scales for the system: the larger one,

$l_{\parallel 2}$, (see Fig. 4 (a), plot (1), and Table 1) is a typical particle extension/width, while the smaller one, $l_{\parallel 1}$, can be understood as a typical pore size between aggregated clay particles, along the direction of the external electric field (see Fig. 1(b) and (c)). Therefore, $l_{\parallel 1}$ is controlled by the particles' sizes and their relative orientations/ positioning, while $l_{\parallel 2}$ is less dependent on the particular arrangement of the particles with respect to each other (provided they are aligned with the electric field). We see that $l_{\parallel 1}$ is significantly different for the Na/Fe-fluorohectorite and the Ni-fluorohectorite samples. The parameter $l_{\parallel 1}$, which depends on the particle arrangement, can be influenced by the type of intercalated cation. From Table 1 we see that Ni-fluorohectorite also has $l_{\parallel 2}$ (average stack diameter) larger than for Na/Fe-fluorohectorite. Thus, it seems that this difference has an effect on the steric hindrances, and on the packing along the direction of the electric field, thereby increasing also the average pore size in the horizontal direction.

The typical relative length scales are indicated in Fig. 1(b); due to the particle polydispersity, they must be understood as average values that do not correspond to a true regular structure of the assembly. Such a regular structure would probably result in a correlation peak in the scattering data, which is not visible here.

Crossovers in the vertical profiles: Along the major axis (vertical direction, perpendicular to the electric field), due to the axial symmetry of the particle population around the direction of the electric field, some of the platelet-shaped particles present their width to the beam, and others present their top/bottom surfaces, so that both the particle- thickness and width should be visible on the scattering profiles. More precisely, if in Figure 1(b) and (c) one imagines an incident beam normal to the paper's

plane, some aggregates are met by the beam as sketched in Fig. 1(b), others as sketched in Fig. 1(c):

- Intensity profiles resulting, along the vertical direction of the detector, from scattering by the latter aggregates (Fig. 1(c)), will exhibit two crossovers, one corresponding to the typical pore size $l_{\perp 1}$, the other one to the typical particle size $l_{\perp 2}$. Due to the statistical isotropy of the particles in their mean plane, $l_{\perp 2}$ and $l_{||2}$ are actually identical (see Fig. 1(b-c)).
- Intensity profiles resulting, along the vertical direction of the detector, from scattering by the former aggregates (Fig. 1(b)), will exhibit two crossovers at the typical particle thickness d and at a typical pore size in the direction perpendicular to the mean plane of an aggregate (vertical direction in Fig. 1(b)).

The profiles recorded along the vertical direction result from a mix of these two configurations and of all intermediate configurations in which the orientation of the aggregate's mean plane is in-between those of Fig. 1(b) and Fig. 1(c). Hence, at large scales we expect a crossover $q_{||2} = q_{\perp 2}$. This is why we have used the value obtained from Fig. 4(a), where the crossover at small q values is more marked. On the other hand, at small length scales, the relevant characteristic length scales are d , $l_{||1}$, $l_{\perp 1}$, and the typical pore size along the normal to the mean plane of aggregate. We believe that these four length scales are close to each other, and are therefore not visible as distinct crossovers in the log-log intensity profiles. Thus, we have defined visually from Fig. 4(b) a single crossover at large q values; its value is indeed close to that found for $q_{||1}$ in Fig. 4(a) (see Table 1).

Signification of the exponents: By changing q, we probe the system at different scales: for $q > q_1$ (in the two directions), we probe the properties of the individual particles; at smaller q- values, we probe the properties of the porous space between the particles, or of aggregates of particles. As summarized in section 2, the values of the exponents D for the fitted power laws denote long range correlations in the inner surfaces (if $3 < D < 4$) or bulk arrangement (if $2 < D < 3$) of the porous medium. Furthermore, the value of exponents D for the fitted power laws denote scattering from aggregated mass (if $1 < D < 3$) of particles if the probed length scales are larger than the particles size.

For $q > q_1$ (see D_1 values in Table 1, in the two directions), we expect the exponent to be controlled by the surface roughness of the particles for all the X-fluorohectorites samples, where X= Na^+, Ni^{2+}, and Fe^{3+}. This is what is observed here for Na/Ni-fluorohectorite samples, but not for Fe-fluorohectorite samples. The other exponents for Na/Ni-fluorohectorite samples are also greater than 3 in absolute value, which indicates a predominant surface scattering at all scales probed by the experiment for Na/Ni-fluorohectorite samples. Note that due to the axial symmetry discussed above, the exponent observed in Fig.4 (a), in the large q-range, is probably determined by the scattering properties of the lateral surfaces of the clay particles, while the exponent found in Fig. 4 (b), in the same range of q-values, results from a mixed scattering by the lateral- and the top/bottom surfaces of the platelet-shaped scatterer. This is why two different exponents are observed, although at those length scales smaller than the particle thickness the difference in meso-porous arrangement arising from the particles' anisotropy plays no role.

Fe- fluorohectorite samples behave differently from the other samples (Table 1): the exponent $D_{||i}$ ($i=1, 2, 3$) and $D\perp_i$ ($i=1, 2$) are smaller than 3, indicating that, both along

minor- and major axis, the scattering is controlled by the mass aggregates of Fe-fluorohectorite particles, rather than by the roughness of their surface in bundle structure. Since the primary particles i.e., the stacked clay platelets, have the same chemical composition in all samples, this suggests that the nature of the intercalated cations changes the interactions between particles enough to influence the meso-structure of the aggregates.

The geometry studied here has similarities with that observed for dry-pressed samples, in which all particles have their flat surfaces parallel on average, in a nematic-like arrangement. Namely, we have inferred a geometric description in which the overall assembly possesses a statistical axial symmetry around the direction of the applied electric field, but consists of aggregates (like that sketched in Fig. 1(b)) with a nematic-like arrangement. Such nematic arrangements were previously studied using small angle neutron scattering (SANS) for Na-fluorohectorite samples, by Knudsen et al.[52]. In those samples, which were dehydrated under a uniaxial load of 0.12 MPa and 2.60MPa, and in which clay particles are expected to be much more densely packed than in the electro-rheological bundles addressed in the present paper, the authors inferred a correlation length for the porous medium in the direction of the applied load, and one along the average plane of the clay particles. These correlation lengths can be related to typical pore sizes in the two directions, and were observed to be 2 times larger along the particle planes than in the direction of the load, probably due to the particles' aspect ratio and the dense packing. In the present system, no typical pore size can be observed at length scales different from the typical pore size $l_{\perp_1}$, i.e., in aggregates like that pictured in Fig. 1(b), the typical pore size normal to the aggregate's mean plane is similar to the pore size along that plane; this indicates a looser packing.

IV. CONCLUSION

We have studied the porous medium in electrorheological bundles of fluorohectorite clay particles, using X-ray small angle scattering. The platelet-shaped scatterers have a lateral size in the micron range and a thickness 10−20 times smaller. Three types of samples were studied: Na-, Ni-, and Fe-fluorohectorite, corresponding to cations with three different valences, from +1 to +3. The two-dimensional SAXS patterns obtained from these bundled structures are clearly anisotropic, reflecting the preferential orientation of the particles in the field. They can be analyzed in order to obtain a geometrical characterization of the assembly of aggregated polarized particles. It confirms a geometric model for particle packing that we had previously inferred from WAXS experiments. Scattering profiles recorded along the azimuthal directions parallel to and perpendicular to the applied electric field exhibit several power law regimes, with crossover scales between them that correspond to typical length scales of the particle assembly. For samples of Na- and Ni-fluorohectorite, the exponents of the power laws are in the range usually attributed to surface scattering and mass scattering with a correlated roughness depending upon the nature of intercalated cations. For Fe-fluorohectorite, bulk scattering seems to be predominant, although this influence of the intercalated cations on the meso-structure of the bundles is not yet understood.

This study opens many new prospects. Firstly, one may combine SAXS with SALS studies in order to obtain power law exponents on an even wider q-range. Secondly, we plan to investigate the relationship between the local structure around the intercalated cation and the overall collective behavior of the clay particles, by studying some selected X-fluorohectorite samples (X being the intercalated cation) with EXAFS.

Thirdly, it will be of interest to relate the measured ellipse eccentricity to the orientation density probability function of the population of platelets, as done in a recent study[53] in which an identical geometry was addressed for magnetically-oriented Gibbsite particles.

ACKNOWLEDGMENTS

The staff at the DUBBLE beamline at ESRF is gratefully acknowledged for support during the SAXS experiments. This work was supported by the Research Council of Norway (RCN) through a Strategical University Program and through the Nanomat Program: RCN projects 152426/431, 154059/420, 148865/432, and 138368/V30 and SUP154059/420.

[1] R. Tao, ed., International Conference on Electrorheological Fluids: Mechamism , Properties, Structure, Technology and Application (World Scientific Singapore, 1992).

[2] L. C. Davis, Appl. Phys. Lett. **60**, 319 (1992).

[3] R. A. Anderson, Langmuir **10**, 2917 (1994).

[4] H. Block and Kelly, J. P., J. Phys. D **21**, 1661 (1998).

[5] T. Hao, Adv. Mater. **13**, 1847 (2001).

[6] A. P. Gast and C. F. Zukowski, Adv. Colloid Interface Sci. **30**, 153 (1989).

[7] P. M. Adriani and A. P. Gast, Faraday Discuss. Chem. Soc. **90**, 17 (1990).

[8] H. Block, J. P. Kelly, A. Qin, and T. Watson, Langmuir **6**, 6 (1990).

[9] T. C. Halsey, Science **258**, 761 (1992).

[10] M. Parthasarathy and D. J. Klingenberg, Materials Sci. Eng. **R17**, 57 (1996).

[11] R. Tao and J. M. Sun, Phys. Rev. Lett. **67**, 398 (1991).

[12] R. Tao and J. M. Sun, Phys. Rev. A **44**, R6181 (1991).

[13] T. J. Chen, R. N. Zitter, and R. Tao, Phys. Rev. Lett. **68**, 2555 (1992).

[14] W. Wen, N. Wang, H. Ma, Z. Lin, W. Tam, C. Chan, and P. Sheng, Phys. Rev. Lett. **82**, 4248 (1999).

[15] M. Golosovsky, Y. Saado, and D. Davidov, Appl. Phys.Lett. **75**, 4168 (1999).

[16] J. Martin, R. Anderson, and C. Tigges, J. Chem. Phys. **108**, 3765 (1998).

[17] M. Ota and T. Miyamoto, J. Appl. Phys. **76**, 5528 (1994).

[18] C.W.Wu and H. Conrad, J. Appl. Phys. **83**, 3880 (1998).

[19] W. Wen, H. Ma, W. Tam, and P. Sheng, Appl. Phys.Lett. **77**, 3821 (2000).

[20] W.Wen, X. Huang, S. Yang, K. Lu, and P. Sheng, Nature Materials **2**, 727 (2003).

[21] B. Velde, *Introduction to Clay Minerals* (Chapman and Hall, London, 1992).

[22] B. G., C. T. Mitsud, and J. Mering, Clays Clay Mineral. **22**, 379 (1974).

[23] P. D. Kaviratna, T. J. Pinnavaia, and P. A. Schroeder, J. Phys. Chem. Solids **57**, 1897 (1996).

[24] J. O. Fossum, Physica A **270**, 270 (1999).

[25] G. J. da Silva, J. O. Fossum, and E. DiMasi, Phys. Rev. E **66**, 011303 (2002).

[26] J. O. Fossum, Y. Méheust, K. P. S. Parmar, K. Knudsen,and K. J. Måløy, Europhys. Lett. **74**, 438-444 (2006).

[27] H. van Olphem, An *Introduction to Clay Colloid Chemistry* (Interscience, New York, 1977).

[28] J. D. F. Ramsay and P. Lindner, J. Chem. Soc. Faraday Trans. **89**, 4207 (1993).

[29] F. Pignon, A. Magnin, J.-M. Piau, B. Cabane, P. Lindner, and O. Diat, Phys. Rev. E **56**, 3281 (1997).

[30] F. Pignon, A. Magnin, and J.-M. Piau, Phys. Rev. Lett. **76**, 4857 (1996).

[31] E. DiMasi, J. O. Fossum, T. Gog, and C. Venkataraman, Phys. Rev. E **64**, 061704 (2001).

[32] G. J. da Silva, J. O. Fossum, E. DiMasi, K. J. Måloy, and S. B. Lutnæs, Phys. Rev. E **66**, 011303 (2002).

[33] Y. Méheust, K. Knudsen, and J. O. Fossum, J. Appl. Cryst. (2006), in press.

[34] S. H. Chen and J. Teixeira, Phys. Rev. Lett. **57**, 2583 (1986).

[35] T. Freltoft, J. K. Kjems, and S. K. Sinha, Phys Rev. B **33**, 269 (1986).

[36] G. Dietler, C. Aubert, and D. S. Cannell, Phys. Rev. Lett. **57**, 3117 (1986).

[37] R. Vacher, T. Woigner, J. Pelous, and E. Courtens, Phys. Rev. B **37**, 6500 (1988).

[38] D. W. Schaefer and K. D. Keefer, Phys. Rev. Lett. **56**, 2199 (1986).

[39] A. Boukenter, D. Champagnon, J. Dumas, E. Duval, J. F. Quinson, J. L. Rousset, J. Serughetti, S. Etienne, and C. Mai, C. (Paris), Rev. Phys. Appl. **24**, 133 (1989).

[40] F. Chaput, A. Lecomte, A. Dauger, and J. P. Boilot, Rev. Phys. Appl. (Paris) **24**, 137 (1989).

[41] D. Posselt, J. S. Pedersen, and K. Mortensen, J. Non. Cryst. Solids **145**, 128 (1992).

[42] G. Porod, Kolloid Z **124**, 93 (1951).

[43] S. K. Sinha, T. Freltoft, and J. K. Kjems, in *Kinetics of Aggregation and Gelation*, edited by F. Family and D. P. Landau (Elsevier, Amsterdam, 1984), pp. 87–90.

[44] H. D. Bale and P. W. Schmidt, Phys. Rev. Lett. **53**, 596 (1984).

[45] J.Wong, P.-Z. andHoward and J.-S. Lin, Phys. Rev. Lett. **57**, 637 (1986).

[46] J. M. Calo and P. J. Hall, Carbon **42**, 1299 (2004).

[47] D. F. R. Mildner, R. Rezvani, P. L. Hall, and R. L. Borst, Appl. Phys. Lett. **48**, 1314 (1986).

[48] G. Lucido, R. Triolo, and E. Caponetti, Phys. Rev. B **38**, 9031 (1988).

[49] A. P. Radlinski, C. J. Boreham, G. D. Wignall, and J.-S. Lin, Phys. Rev. B **53**, 14152 (1996).

[50] P. W. Schmidt, in *The fractal approach to heterogeneous chemistry*, edited by D. Avnir (John Wiley & Son Ltd., 1989), pp. 67–79.

[51] P. Pfeifer and D. Avnir, J. Chem. Phys. **79**, 3558 (83).

[52] K. D. Knudsen, J. O. Fossum, G. Helgesen, and M. W. Haakestad, Physica B **352**, 247 (2004).

[53] D. van der Beek, A. V. Petukhov, P. Davidson, J. Ferré, J. P. Jamet, H. H. Wensink, G. J. Vroege, W. Bras, H. N. W. Lekkerkerker, Phys. Rev. E **73**, 041402 (2006).

TABLE 1: Calculated fit parameters: (i) average eccentricities of the two-dimensional scattering patterns, and (ii) power law scattering exponents D_i (i = 1, 2, 3) and crossover q_1 and q_2 in the scattering profiles (Fig. 4)

Sample	Na-fluorohectorite	Ni-fluorohectorite	Fe-fluorohectorite
E (V/mm)	1000	1000	1000
No. of images per curve	7	6	9
e	0.54	0.61	0.57
Crossover $q_{\parallel 1}$ (nm^{-1})	0.086±0.003	0.055±0.002	0.087±0.005
Crossover $l_{\parallel 1}$ (nm)	~73±3	~114±5	~72±5
Crossover $q_{\parallel 2}$=$q_{\perp 2}$ (nm^{-1})	0.028±0.002	0.025±0.001	0.028±0.002
Crossover $l_{\parallel 2}$= $l_{\perp 2}$ (nm)	~224±16	~252±10	~224±15
Crossover $q_{\perp 1}$ (nm^{-1})	0.090±0.005	0.057±0.005	0.091±0.005
Crossover $l_{\perp 1}$ (nm)	~70±4	~110±5	~69±5
$D_{\parallel 1}$	3.44±0.05	3.23±0.05	2.63±0.05
$D_{\parallel 2}$	3.02±0.05	3.10±0.05	2.30±0.05
$D_{\parallel 3}$	3.38±0.05	3.34±0.05	2.94±0.05
$D_{\perp 1}$	3.38±0.05	3.21±0.05	2.60±0.05
$D_{\perp 2}$	3.21±0.05	3.07±0.05	2.56±0.05

FIG. 1: (a) Stable electro-rheological structures of iron (Fe) - fluorohectorite clay particles in the host silicone oil and in the presence of a DC external electric field of a magnitude equal to 1 kV/mm. The chain bundles are along the direction of applied electric field. **(b)** A two-dimensional sketch of a nematic aggregate of clay particles inside an ER bundle; the direction of the external electric field is horizontal; the platelet-shaped clay particles are horizontal on average in this particular aggregate; many such aggregates, possessing various orientations around the direction of the electric field, form the overall particle bundle. **(c)** A horizontal cut of the same aggregate, for example through the plane denoted by the red dashed line in (b). The characteristic lengths $l_{\|1}$ and $l_{\|2}$ are also visible in this representation; due to the statistical isotropy of each particle in in its mean plane, the characteristic lengths $l_{\|2}$ and $l_{\perp 2}$ are identical.

FIG. 2: Experimental setup for recording SAXS data from the electro-rheological chain bundles of clay particles. Y is the sample to detector distance (camera length).

FIG. 3: Contour plot of a two-dimensional anisotropic scattering pattern obtained from bundles of iron (Fe)-fluorohectorite clay particles initially dispersed in silicone oil (at 3.0% w/w), in the presence of a DC external electric field of magnitude equal to 1 kV/mm (see Fig. 1). Each of the elliptically-shaped black areas corresponds to an iso-intensity region, i.e. to a given detector count; the logarithms of the detector count values for these iso-intensity regions are equally-spaced. The raw image data, in which grey shadings are proportional to the detector count, is shown as an inset in the top righ part of the image.

FIG. 4: Log-Log plots of the intensity of the scattering profiles recorded as a function of the scattering vector q. The curves have been shifted vertically for better visualization. Different slopes are observed for (1) sodium (Na)-fluorohectorite, (2) nickel (Ni)-fluorohectorite, and (3) iron (Fe)-fluorohectorite, with different crossover between them (see Table 1). **(a):** along the minor axis (horizontal direction, i.e., direction of the applied electric field) and **(b):** along the major axis (vertical axis).

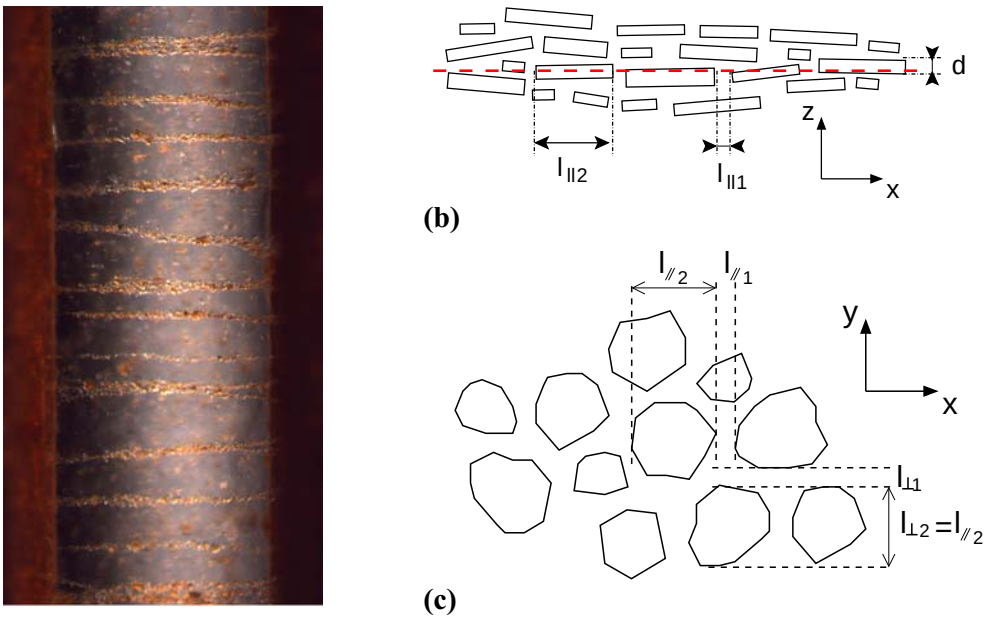

FIG. 1: (a) Stable electro-rheological structures of iron (Fe) - fluorohectorite clay particles in the host silicone oil and in the presence of a DC external electric field of a magnitude equal to 1 kV/mm. The chain bundles are along the direction of applied electric field. **(b)** A two-dimensional sketch of a nematic aggregate of clay particles inside an ER bundle; the direction of the external electric field is horizontal; the platelet-shaped clay particles are horizontal on average in this particular aggregate; many such aggregates, possessing various orientations around the direction of the electric field, form the overall particle bundle. **(c)** A horizontal cut of the same aggregate, for example through the plane denoted by the red dashed line in (b). The characteristic lengths $l_{\|1}$ and $l_{\|2}$ are also visible in this representation; due to the statistical isotropy of each particle in in its mean plane, the characteristic lengths $l_{\|2}$ and $l_{\perp 2}$ are identical.

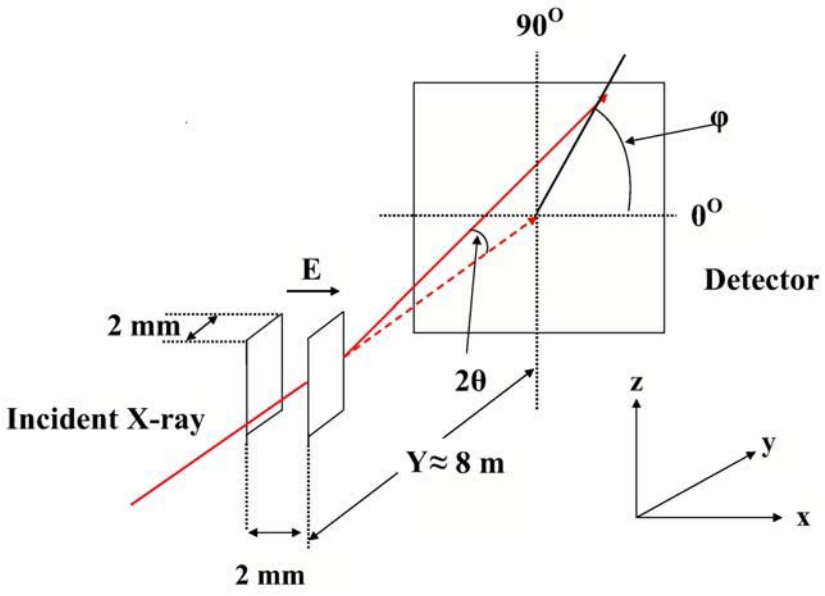

FIG. 2: Experimental setup for recording SAXS data from the electro-rheological chain bundles of clay particles. Y is the sample to detector distance (camera length).

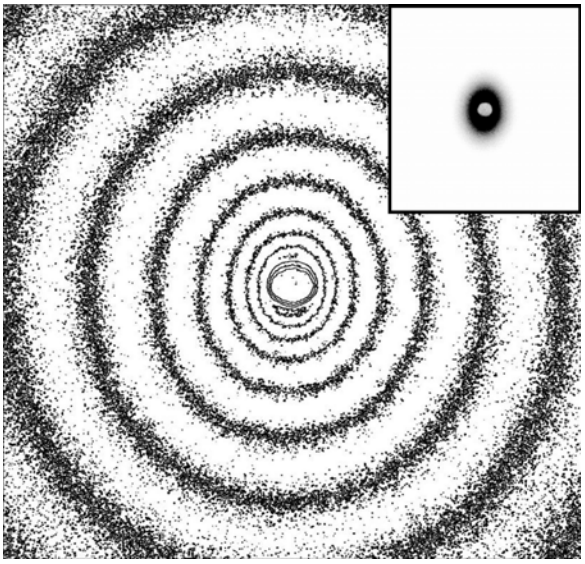

FIG. 3: Contour plot of a two-dimensional anisotropic scattering pattern obtained from bundles of iron (Fe)-fluorohectorite clay particles initially dispersed in silicone oil (at 3.0% w/w), in the presence of a DC external electric field of magnitude equal to 1 kV/mm (see Fig. 1). Each of the elliptically-shaped black areas corresponds to an iso-intensity region, i.e. to a given detector count; the logarithms of the detector count values for these iso-intensity regions are equally-spaced. The raw image data, in which grey shadings are proportional to the detector count, is shown as an inset in the top righ part of the image.

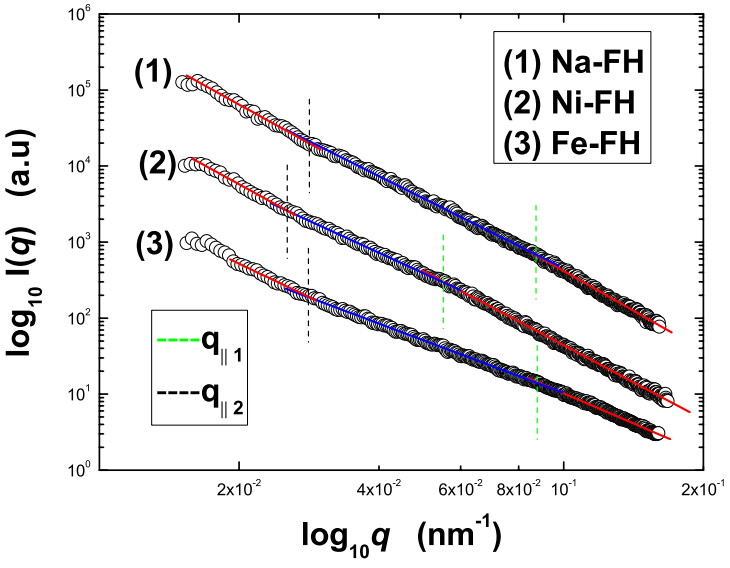

(a)

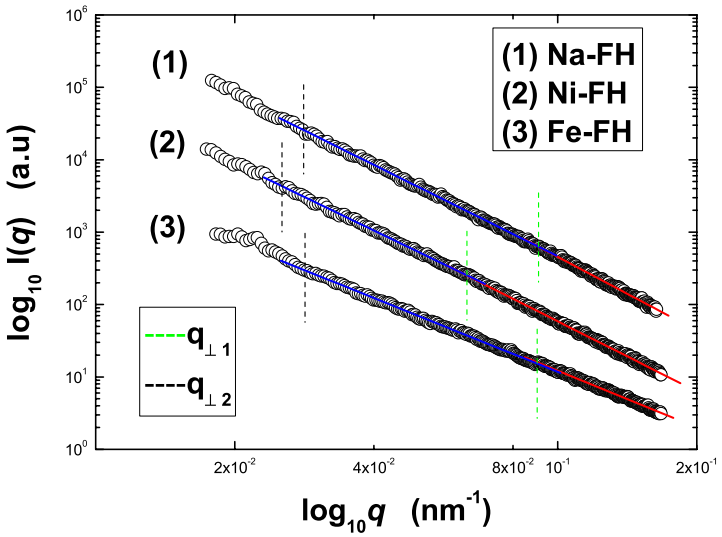

(b)

FIG. 4: Log-Log plots of the intensity of the scattering profiles recorded as a function of the scattering vector q. The curves have been shifted vertically for better visualization. Different slopes are observed for (1) sodium (Na)-fluorohectorite, (2) nickel (Ni)-fluorohectorite, and (3) iron (Fe)-fluorohectorite, with different crossover between them (see Table 1). **(a):** along the minor axis (horizontal direction, i.e., direction of the applied electric field) and **(b):** along the major axis (vertical axis).

Paper 4

Electrorheological suspensions of laponite in oil: rheometry studies under steady shear

K. P. S. Parmar, Y. Méheust, and J. O. Fossum[*]

Department of Physics, Norwegian University of Science and Technology,

NTNU,

7491 Trondheim, Norway

[*]jon.fossum@ntnu.no

Paper IV is not included due to copyright.

Paper 5

Electrorheology of Synthetic Na-Fluorohectorite Clay Particles Suspended in Oil: Rheometry Studies under Steady Shear

K. P. S. Parmar, Y. Méheust, and J. O. Fossum[**],
Department of Physics, Norwegian University of Science and Technology, NTNU, N-7491 Trondheim, Norway

[*]jon.fossum@ntnu.no

Abstract. –Under application of an electric field greater than a triggering electric field E_c~0.4 kV/mm, fluorohectorite particles suspended in a silicone oil aggregate into chain- and/or column-like structures. We report here on the effect of this micro-structural change on the rheological properties of such colloidal suspensions: without an applied electric field, the steady state shear behavior of such suspensions is Newtonian-like; under application of an electric field larger than E_c, a significant yield stress is measured, and under continuous shear the fluid is shear-thinning. Here we report on studies of steady shear rheological properties as a function of particle volume fraction, for various strengths of the applied electric field. The steady shear flow curves can be scaled onto a master curve with respect to electric field strength, in a manner similar to what was recently done on suspensions of synthetic laponite clay [16]. In the present case of Na-fluorohectorite, the yield stress is demonstrated to depend on the applied electric field, E, as E^{α}, with α~1.93, and α~1.58, for the dynamic and static yield stresses, respectively. This measured yield stress behavior is consistent with standard conduction models for electrorheological systems. Interesting prospects include using such systems for guided self-assembly of clay nano-particles.

In this report, we investigate colloidal suspensions of electrically polarizable nanolayered clay particles suspended in silicone oil. When such suspensions are subjected to an external electric field, of the order of ~1kV/mm, the particles become polarized, and subsequent dipolar interactions are responsible for aggregating a series of interlinked particles that form chains and columns parallel to the applied field. In the general case [1–8], i.e. not necessarily clay particles in suspension as in the present case, this kind of structuring stabilizes within some tenths of seconds, and disappears when the field is removed. The structuring coincides with a drastic change in rheological properties of such suspensions, which is why

they are called Electro-Rheological (ER) fluids [1]; the mechanical behavior of such a system is thus controllable by the applied electric field [1–8]. Various physical and chemical properties of particles and the suspending liquid may control the behavior of an ER-fluid: Dielectric constant and/or-conductivity of the suspended particles [5-6], volume fraction of particles [9], frequency and magnitude of the applied electric field [5-6]. Other factors such as particle geometry [10-12], size [13-14] and polydispersity [13-14] also influence the ER-shear stress behavior. Small amounts of additives like water [15] adsorbed and/or- absorbed on the particles, may also play an important role for certain types of ER fluids.

Recently, we have studied the effect of an external DC electric field (~kV/mm) on the rheological properties of colloidal suspensions consisting of laponite particles in a silicone oil [16]. The laponite particles were observed to exhibit the polarization and subsequent aggregation typical of ER fluids. Without an applied electric field, the steady state shear behavior of such laponite suspensions is Newtonian-like. Under application of an electric field larger than the triggering field, it was measured to change dramatically: a significant yield stress is measured, and under continuous shear the fluid is shear-thinning. We studied the rheological properties, in particular the dynamic and static shear stress, τ, as a function of particle volume fraction, for various strengths of applied electric field, E. We showed that the flow curves under continuous shearing can be scaled with respect to both, particle fraction, Φ, and electric field strength, onto a master curve, of the form:

$$\tau\left(\Phi, E\right) = \Phi^{\beta} E^{\alpha} f\left(\frac{\dot{\gamma}}{\Phi E^{2}}\right) \tag{1}$$

where $\dot{\gamma}$ is the shear rate, α and β are scaling exponents, and f represents the master curve. We demonstrated that Eq. (1) is consistent with simple scaling arguments. We showed that in the laponite case, the shape of this master curve approaches a standard Herschel-Bulkley model at high Manson numbers. For our laponite suspensions, both dynamic and static yield stress were thus shown to depend on the particle fraction Φ and electric field E as $\Phi^{\beta}E^{\alpha}$, with α ~1.85, and β~1 and 1.70, for the dynamic and static yield stresses, respectively. In this case we argued that the measured yield stress behavior may be explained in terms of standard conduction models for electrorheological systems.

The clay particles investigated in the present report belong to the same family as the laponite particles, namely 2:1 clays, whose basic structural unit is a 1 nm-thick platelet consisting of two tetrahedral silica sheets

sandwiching one octahedral silica sheet. 2:1 clays carry a moderate negative surface charge on their plane surfaces. This charge is usually sufficiently large so that individual platelets are able to stack by sharing cations, and at the same time moderate enough so as to allow further intercalation of water molecules into the resulting "decks of cards"-like smectite particles. Natural 2:1 clay particles dispersed in salt solutions have been studied for decades [17], and recently there has been a growing activity in the study of complex physical phenomena in synthetic smectites [18]. Much effort has gone into relating the lamellar microstructure of smectite clay-salt water suspensions to their collective interaction and to resulting macroscopic physical properties, such as phase behavior and rheological properties [18-27]. Nematic liquid crystalline-like ordering in smectite systems has been characterized by the observation of birefringent domains with defect textures [21, 23-24] and by X-Ray scattering [22, 25-25].

In the present report, we study in particular X-fluorohectorite (X-FH), where X is an interlayer cation such as Na^{+}, Ni^{2+}, or Fe^{3+} etc. The chemical formula of Na-FH is $Na_{-0.6}$ ($Mg_{-2.4}$ $Li_{-0.6}$) $Si_4O_{10}F_2$ per half unit cell. The individual fluorohectorite particle density is 2.8 [28]. X-FH are 2:1 synthetic sheet silicate clay minerals; whose particles are made of ~80-100 negatively surface charged clay platelets [22,29-41] residing on top of each other with intercalated charge balancing cations X [18,30]. Each clay platelet is about 1 nm thick and the layer charge density of the platelet is 1.2 e^{-} /unit cell [30]; allowing the interlayer cations to be exchanged with other types of cations. As for all 2:1 clays, water molecules or other polar molecules can be adsorbed or intercalated between interlayer spaces of the platelets, depending upon the environmental conditions such as temperature and relative humidity etc. [28-34]. In the dry state, X-FH clay particles are sheet-like (thickness ~ 0.1 μm); their lateral size can vary from tenths of nm up to a few μm. When observed in a scanning electron microscope (SEM), untreated sodium fluorohectorite (Na-FH) clay powder display particles with edges and surfaces that are very rough and they are highly anisotropic in their shape, and highly polydisperse in size along their lateral directions. The lateral size of such clay particles can be further reduced by a process of fine grinding of its powder.

Recently, we have demonstrated; that X-FH particles suspended in silicone oil display ER structuring [35-36]. We reported on synchrotron X-ray scattering investigations of chain or-column like-structures of X-FH particles [35], and we determined the direction of induced dipoles in X-FH particles, and the structural morphology (preferred positional and orientational of X-FH particles) of the chain- or column-like structures. Later we have extended those studies, and we have reported on the voids or pores spaces between the assembled or packed polarized X-FH particles [36]. We have pointed to the migrations of surface charges and possible

movement of interlayer cations X of X-FH as main factors, possibly responsible for their polarization in an external dc electric field [35]. In the present report we complement the previous structural studies with results from rheometry studies under steady shear.

As in our previous structural study on X-FH in silicone oil [35], we have used synthetic fluorohectorite, originally purchased from Corning Inc. (New York) in powder form and subsequently cation-exchanged to sodium (Na^+) through an ion exchange method [35]. After dialysis the Na-fluorohectorite clay was first dried at 100 ^{0}C for ~10 hours and then grinded in powder form with the help of a mortar and spatula. As suspending liquid in the present studies, we used the silicone oil: Dow Corning 200/100 Fluid (dielectric constant = 2.5, viscosity = 100 mPa-s and specific density = 0.973 at 25 ^{O}C) with a small conductivity of about 10^{-12} S/m [37]. Four different ER suspensions of dehydrated Na-FH clay particles with different volume fractions (Φ) were prepared following a protocol previously established with oil-laponite suspensions[16]: (1) removal of water traces in the clay powder and oil by 72 hrs-long heating at 130 ^{0}C; (2) mixing of the powders and silicone oil inside glass tubes; (3) cooling of the sealed tubes to room temperature; (4) Homogeneization of the suspensions by hand- and subsequent ultrasonic bath-shaking for 30 minute, at 25 ^{0}C. The suspensions were subsequently left to rest so as to remove clay particles with a spherical diameter larger than ~100 μm (according to Stoke law of particles settling). The remaining suspensions were again hand-shaken about five minutes for three times. Under such conditions, the clay particles were well dispersed in silicone oil as observed by eye. It should be noted that after removal of the large particles, the volume fraction (Φ_0) of the clay particles is significantly lower than the initial volume fraction (Φ) of the prepared ER suspensions. Consequently, Φ_0 is not precisely known.

The rheology of fluorohectorite clay suspensions was measured under an applied DC electric field, using a Physica MCR 300 Rotational Rheometer equipped with a coaxial cylinder Couette cell (Physica ERD CC/27). The outer cylinder diameter is 14.46 mm, and the inner is 13.33 mm. The immersion length is 40 mm and the sample volume is 19.35 ml. All rheological measurements were carried out at constant temperature 25 ^{0}C. The steady shear rheological properties were measured after the suspensions had been pre-sheared at $\dot{\gamma}$ = 200 s^{-1} for 60 s in order to give the same initial conditions. In order to determine the static yield stress, a control shear stress (CSS) test i.e. linearly increasing shear stresses (with a step of 2 Pa) were applied in disrupt ER suspensions that were and had been in applied dc electric field for 5 minutes. Two grounding brushes connected to the bob's axis induce an artificial 1 Pa yield stress in all data, but this value is

negligible compared to all yield stress values addressed here. All rheological measurements were carried out at constant temperature (25 ^{0}C).

Without an electric field, the ideal steady state shear behavior of an ER fluid is Newtonian-like [38] and the volume fraction (Φ) of particles only increases the magnitude of its viscosity. The Φ-dependent viscosity of an ER fluid of monodisperse spherical particles suspended in Newtonian-liquid ($\Phi < 3\%$) can be approximated by the Batchelor relation [39] and the Krieger-Dougherty relation [39]. These relations account for the interactions between the particles themselves and between particles and the surrounding liquid. One empirical equation which has been found to account for the viscosity of monodisperse and polydisperse sphere suspensions in a range of particle fraction up to 50%, has been suggested by Chong, Christiansen and Baer [40]. The three relations mentioned above can strictly only be used to describe the viscosity of concentrated colloidal suspensions of isotropic and monodisperse non-charged particles [57'-58], but the Chong-Christiansen-Baer relation [40] has been found to be an appropriate description for concentrated suspensions of kaolinite clay [41], a system that consists of anisotropic and polydisperse particles.

Steady state flow curves (i.e. obtained from Controlled Shear Rate tests) for four different volume fractions (Φ) of Na-FH clay suspensions at zero applied electric field are shown in Figure 1 (a). These suspensions show a Newtonian behavior i.e. constant viscosity (ratio of shear stress to the applied shear rate) and no value of pre-yield stress. The viscosity of Na-FH clay suspension increase with the volume fraction of clay particles as illustrated in Figure 1 (b). As the volume fraction of particles (Φ) increases the various interaction forces such as hydrodynamics forces, dispersion forces, electrostatic forces, and polymeric forces simultaneously act between the clay particles themselves and between the clay particles to that of silicone oil. The net result is an increase in the viscosity.

In our recent study of oil suspensions of synthetic laponite we found that the following empirical relation can be used to fit the zero field viscosity [16] :

$$\eta = \eta_0 \left(1 + \frac{K}{\frac{\Phi_m}{\Phi} - 1} \right)^2 \qquad (2)$$

Equation (2) represents a generalization of the Chong-Christiansen-Baer relation [40] Using Equation (2) in the present case, we find K= 0.123 and Φ_m=88.7% as a best fit to the data in Fig. 1(b). Φ_m is expected to be a measure of the maximum packing fraction [40]. As discussed above, the true $\Phi_0 < \Phi$ is uncertain in the present case, thus the meaning of Φ_m is somewhat

lost (the true maximum packing fraction probably being smaller than Φ_m in the same manner as Φ_0 is overestimated by Φ).

Under application of an electric field (~kV/mm) and in steady state shear, a general ER fluid shows a well-defined yield stress beyond which it tends to be shear-thinning (pseudoplastic) i.e. the viscosity decreases with increasing shear rate. The typical steady-shear behavior of an ER fluid under the influence of an external electric field is generally characterized as a Bingham-like solid [38]. The value of the dynamic yield stress is strongly influenced by the rheological model and the shear rate range selected, as it is obtained by extrapolating the curves from steady state shearing measurement to zero shear rate. Under application of an electric field, the yield stress of a completely broken-down ER fluid is its dynamic yield stress, whose value can be significantly different from the static yield stress i.e. a yield stress of a disrupt (no shearing) ER fluid [42]. There are several models that attempt to explain the shear stress behavior for various ER fluids. The polarization theory [8,43], based on the mismatch in dielectric constant between the particles and the suspending liquid, predicts that the yield stress is proportional to E^{α}, where E is the magnitude of the applied electric field and the exponent α is equal to 2. In the polarization theory, the response of the particle polarization and the suspending liquid are assumed to be linearly related to the applied electric field. The conduction theories based on the mismatch in conductivity between the particles and the suspending liquid predict the exponent as $1 \leq \alpha < 2$ at both low- and high-volume fractions of particles [44-48]. Also multipole effects are often proposed to account for particle interactions at relatively high concentrations of particles [5-6].

Figure 2 (a) and 2 (b) shows the shear stress- and viscosity- curves (obtained from Controlled Shear Rate CSR tests) for one of our Na-FH clay suspensions at Φ=37.2%. under various magnitudes of the applied DC electric field. Behaviors similar to Figure 2 (a) and 2(b) are observed for other prepared concentrations of Na-fluorohectorites particles. Increasing the electric field causes an increase in the shear stress (and viscosity) of these suspensions and the shear stress vs. shear rate curves become Bingham–like or pseudoplastic (shear thinning) over the entire range of shear rates. At very low shear rate, these clay suspensions show dynamic yield stresses that become larger as the magnitude of the electric field increases.

Following the approach previously used for laponite ER- effects under steady shear [16], we show in Figure 3 (a) scaling in the form of Equation (1) (for constant Φ) applied to the data in Figure 2(a). The result is quite satisfying and in good agreement with our previous findings for laponite [16]. Figure 3 is for one concentration Φ = 37.2 %. The other concentrations that we have investigated, display equivalent behaviors with $\alpha \approx 1.93$. We

observe that the asymptotic behavior at the highest values of the horizontal scaling parameter, is Bingham like.

Figures 4(a) and 4(b) show the effect of the volume fractions (Φ) of clay particles on the flow- and viscosity- curves (Controlled Shear Rate CSR tests) for Na-FH ER fluids at a fixed applied electric field E~ 1.3 kV/mm. The shear stress- increases with the volume fraction (Φ) of clay particles, and its behavior is seen to be Bingham-like over the entire range of applied shear rates. The corresponding viscosity-curves also show an increase in viscosity with increasing volume fraction of clay particles. We also observe yield stresses that increase with increasing volume fraction Φ.

In the present case, we have not been able to find a good data collapse and scale that data in Figure 4 (a) according to equation (1) for fixed E. We attribute this to the large uncertainties connected to the real Φ-values, for the present samples, as described above. Furthermore, we could not perform more systematic tests on the influence of the particle fraction due to shortage of sample (fluorohectorite powder).

Figure 5 shows the static yield stress (obtained from Controlled Shear Stress CSS test) plotted versus applied dc electric field for different volume fraction (Φ) of the present ER fluids. The static yield stresses increases when the strength of the applied DC electric field increases. All our static yield stresses are observed to be proportional to E^{α}, with values of exponents α close to 1.58 for all Φ values. This is illustrated in Figure 6, where the static yield stress is scaled with $E^{1.58}$ and plotted versus Φ. Figure 6 illustrates the large uncertainties connected to the real Φ values for the present samples.

The value obtained for $\alpha \approx 1.58$ suggests that interaction forces between polarized clay particles are governed by their conductivity mismatch to that of the silicone oil, thus indicating that the polarization of such clay particles in an applied external dc electric field is caused by migration of surface charge and also maybe by movements of interlayer cations (Na^{+}). In the present study, the conductivity of dehydrated Na-FH clay particles and silicone oil that are used to prepare the ER suspensions are not known. Other types of experiments are needed in order to understand in more detail the particle conductivity influence on these ER effects. Note that the conductivity of the suspending oil might also increase in applied electric fields [37,46], and this may lead to a significant effect on ER behavior. In Figure 5, a large "jump" in static yield stress is clearly seen between Φ equal to 37.2 and to 47.0. This rapid "jump" is experimentally reproducible for the one sample we have studied at Φ = 47.0. We can at present not explain this "jump", although we may suggest that it possibly could be due to formation of larger effective aggregates above some critical threshold Φ between 37.2 and 47.0.

In this report, we have studied the electrorheological behavior of sodium fluorohectorite clay particles suspended in silicone oil. In absence of electric field, these clay particle suspensions are Newtonian-like, and the clay particles volume fraction only increases the viscosity of such suspensions. Under application of a DC electric field larger than about 0.4 kV/mm, the flow curves of such clay particle suspensions are Bingham-like, exhibiting a well-defined yield stress that increases with increasing volume fraction of particles as well as with increasing applied electric field. The static yield stresses observed follow a power law $E^{1.58}$, suggesting that interaction forces are governed by the conductivity mismatched between dipolar particles (fluorohectorite) and the suspending medium (silicone oil). The observed yield stresses are similar to other comparable systems [16].

The effect of clay particle nature i.e. their anisotropic shapes, edges and surface roughnesses, as well as and shape and size polydispersity on shear stress- and viscosity- can not be distinguished in the present case. The anisotropic shape of our clay particles may cause enhanced dipolar interactions as compared to same size and same conducting isotropic spherical particles [11]. But at the same time, size and shape polydispersity may cause reduction of shear stress- and viscosity- as these will depend on the packing of individual clay particles in chain or- column like-structures [49]. In order to better understand the influence of clay particles nature (physical shape and chemical polarisibility) on ER effects, a systematic investigation controlling these parameters is required, and is beyond the present study.

The present report adds mechanical behaviors and "numbers" to the structural parameters determined in our previous studies on these systems [35-36]. Future prospects include reducing the polydispersity of the suspensions, as well as investigating methods for functionalizing such the surfaces in order to ease single grain dispersion in oils. The presently-obtained values for yield stresses suggest that such fluorohectorite-based ER fluids would not be able to compete with other systems in terms of practical use. Rather, one application of these systems of (possibly functionalized) fluorohectorite particles could be in guided self-assemblies of nanoparticles for nano-templating and/or inclusion in composite materials.

Acknowledgements

This work was supported by NTNU, and by the Research Council of Norway (RCN) through the RCN NANOMAT Program as well through a RCN SUP (Strategic University Program) project awarded to the COMPLEX CRT in Norway: (see www.complexphysics.org).

5. References

[1]. Halsey T.C., “Electrorheological fluids”, Science 258, 761 (1992).

[2]. Hao T., “Electrorheological fluids”, Adv. Mater. 13, 1847 (2001).

[3]. Halsey T., and Martin J., "Electrorheological fluids", Scientific American, pp. 42-49 (Oct. 1993).

[4]. Tian Hao “Electrorheological suspensions” Adv. Colloid Interface Sci., 97, 1 (2002).

[5]. Parthasarathy, M. and Klingenberg, D.J., “Electrorheology: mechanisms and models”, Materials Sci. Eng. R17, 57 (1996).

[6]. Block H., Kelly J.P., Qin A., and Watson T., “Materials and mechanisms in electrorheology”, Langmuir 6, 6 (1990).

[7]. Weijia W., D.W. Zheng, and K.N. Tu, “Chain/column evolution and corresponding electrorheological effect”, J. App. Phy. 85, 530 (1999).

[8]. Halsey T.C. and Toor W., “Structure of electrorheological fluids”, Phys. Rev. Lett. 65, 2820 (1990).

[9]. Yu Tian, Yonggang Meng, Shizhu Wen, “Particulate volume effect in suspensions with strong electrorheological response”, Materials Letters 57, 2807 (2003).

[10]. Asano, K. et al., “Influence of the particle configuration on electrorheological effect,” J. Electrost., 40, 573 (1997).

[11]. Kanu, R.C. and M.T. Shaw, “Enhanced electrorheological fluids using anisotropic particles,” J. Rheo., 42, 657 (1998).

[12]. Xiaodong Duan, Weili Luo, Hong Chen, and Yuanjin He, “The effect of particle shape on water-free mica ER fluids”, J. Intell. Mat.al Systems and Structures, 11, 43 (2000).

[13]. Zhi-Jie Tan et al., “Influences of the size and dielectric properties of particles on electrorheological response”, Phys. Rev. E 59, 3177 (1999).

[14]. Yung –H. and Conrad H., “Influence of particle size on the dynamic strength of electrorheological fluids”, International Journal Of Modern Physics B [Condensed Matter Physics; Statistical Physics; Applied Physics], Vol. 8, Nos. 20-21, 2835-2853 (1994).

[15]. Wong, W. and Shaw, M.T., “The role of water in electrorheological fluids”, In:, Anonymous (1998).

[16]. K.P.S. Parmar, Y. Méheust and J.O. Fossum, “Electrorheological suspensions of laponite in oil: rheometry studies under steady shear”, Preprint submitted.

[17]. Velde B., *Introduction to Clay Minerals* (Chapman and Hall, London) 1992.

[18]. Fossum J. O., “Physical phenomena in clays”, Physica A, 270, 1-2, (1999).

[19]. Mourchid A., Lecolier E., van Damme H. and Levitz P., **"**On Viscoelastic, Birefringent, and Swelling Properties of Laponite Clay Suspensions: Revisited Phase Diagram**"**, *Langmuir*, **14** (1998) 4718.
[20]. Bonn D., Kellay H., Tanaka H., Wegdam G. and Meunier J., **"**Laponite: What Is the Difference between a Gel and a Glass?",*Langmuir*, **15** (1999) 7534.
[21]. Gabriel J.-C. P. *et al.*, Swollen liquid-crystalline lamellar phase based on extended solid-like sheets", *Nature*, **413** (2001) 504.
[22]. DiMasi E., Fossum J. O., Gog T. and Venkataraman C., "Orientational order in gravity dispersed clay colloids: A synchrotron x-ray scattering study of Na fluorohectorite suspensions", *Phys. Rev. E*, **64** (2001) 061704.
[23]. Lemaire B. J., Panine P., Gabriel J.-C. P. and Davidson P., The measurement by SAXS of the nematic order parameter of laponite gels**"** *Europhys. Lett.*, **59** (2002) 55
[24]. Fossum J. O., Gudding E., Fonseca D. M., Meheust Y., DiMasi E., Gog T. and Ventakaraman C., Observations of orientational ordering in aqueous suspensions of a nano-layered silicate", *Energy*, **30** (2005) 873.
[25]. D.M. Fonseca, Y. Méheust, J.O. Fossum, K.D. Knudsen, K.J. Måløy and K. P.S. Parmar, "*Nematic ordering of platelet-shaped nanosilicate colloids in saline solu-tions*", submitted to in J. Appl. Cryst.
[26]. Coussot P., Nguyen Q. D., Huynh H. T. and Bonn D., **"**Avalanche Behavior in Yield Stress Fluids**"**, *Phys. Rev. Lett.*, **88** (2002) 175501.
[27]. Bonn D., Tanase S., Abou B., Tanaka H. and Meunier J., **"**Laponite: Aging and Shear Rejuvenation of a Colloidal Glass**"**, *Phys. Rev. Lett.*, **89** (2002) 015701.
[28]. Kenneth D. Knudsen, Jon Otto Fossum, Geir Helgesen and Vegard Bergaplass, "Pore characteristics and water absorption in a synthetic smectite clay", J. Appl. Cryst. 36, 587 (2003).
[29]. G. J. da Silva, J.O. Fossum, E. DiMasi, K. J. Måløy, and S. B. Lutnæs, "Synchrotron x-ray scattering studies of water intercalation in a layered synthetic silicate", Phys. Rev. E 66, 011303 (2002)
[30]. P.D. Kaviratna, Thomas J. Pinnavaia and P.A. Schroeder, "Dielectric properties of smectite Clays", J. Phys. Chem Solids 57, 1897 (1996).
[31]. G. J. da Silva, J.O. Fossum, E. DiMasi, and K. J. Måløy, "Hydration transitions in a nanolayered synthetic silicate: A synchrotron x-ray scattering study", Phys. Rev. B 67, 094114 (2003)
[32]. K.D. Knudsen, J.O. Fossum, G. Helgesen and M.W. Haakestad, "Small-angle neutron scattering from a nano-layered synthetic silicate", Physica B: Condensed Matter, 352, 247-258 (2004)
[33]. Y. Meheust, B. Sandnes, G. Løvoll, K.-J. Måløy, J.O. Fossum, G. J. da Silva, M. S. P. Mundim, R. Droppa and D. d. Miranda Fonseca, "Using

synchrotron X-ray scattering to study the diffusion of water in a weakly-hydrated clay sample", Clay Science, 12, 66 (2006)
[34]. G. Løvoll, B. Sandnes, Y. Méheust, K.J. Måløy, J.O. Fossum, G.J. da Silva, M.S.P. Mundim, R. Droppa Jr. and D.M. Fonseca, "Dynamics of water intercalation fronts in a nano-layered synthetic silicate: A synchrotron X-ray scattering study", Physica B: Condensed Matter, 370, 90-98 (2005)
[35]. J.O. Fossum, Y. Méheust, K.P.S. Parmar, D.M. Fonseca, K.D. Knudsen, and K.J. Måløy, "Dipolar chain formation and particle orientational ordering in oil suspensions of nano-layered clay particles", EuroPhys. Lett. 74, 438 (2006).
[36]. K.P.S. Parmar, Y. Méheust, J.O. Fossum, K.D. Knudsen and D.M. Fonseca, "The porous space inside bundles of polarized phyllo-silicate crystallites – A SAXS study, submitted to J. Appl. Cryst.
[37]. Tang X., Wu C. W. and Conrad H., "On the conductivity model for the electro-rheological effect", J. Rheology 39, 1059 (1995).
[38]. Klingenberg, D.J. and Zukoski, C.F., "Studies on the steady-shear behavior of electrorheological suspensions", Langmuir 6,15, (1990)
[39]. Christopher W. Macosko, Ch W. Macosko, Chapter 10; Suspension rheology; in "Rheology: Principles, Measurements and Applications", Wiley, John & Sons, Incorporated (1994)
[40]. Chong J.S., Christiansen E.B. and Baer A.D., "Rheology of concentrated suspensions", J. Appl. Polym. Sci. 15, 2007 (1971)
[41]. Coussot, P., "Structural similarity and transition from newtonian to non-newtonian behavior for clay-water suspensions", Phys. Rev. Lett. 74(20), 3971 (1995).
[42]. Shenoy A. V.; Chapter 4; Constitutive Theories and Equations for Suspensions; in "Rheology of filled polymer systems", Kluwer Academic Publishers (1999).
[43]. Martin, J.E. and Anderson, R.A., "Chain model of electrorheology", J. Chem. Phys. 104, 4814 (1996).
[44]. Atten, P., "A conduction model of the electrorheological effect," Int.J. Mod. Phys. B, 8(20–21), 2731 (1994).
[45]. Anderson R.A., "Effect of finite conductivity in electrorheological fluids", Proc. 3rd. Int. Conf. on Electrorheological Fluids edited by R. Tao (Singapore: World Scientific) pp 81-90 (1992).
[46]. Felici N., Foulc J.N. and Atten P., "A conduction model of electro-rheological effect", Proc. 4th Int. Conf. Electrorheological Fluids edited by R Tao and G D Roy (Singapore: World Scientific) pp 139-52 (1994).
[47]. C.W. Wu and H. Conrad, "A modified conduction model for the electrorheological effect", J. Phys. D: Appl. Phys. 29, 3147 (1996).
[48]. Wu C.W., Chen, Y. Tang, X., and Conrad, H., "Conductivity and force between particles in a model electrorheological fluid: I conductivity,"

International Journal of Modern Physics B, 10, (23/24), 3315-3325, (1996).
[49]. D. Brooks, J. Goodwin, C. Hjelm, et al., "Viscoelastic Studies on an Electrorheological Fluid", Colloids Surf. 18, 293 (1986).

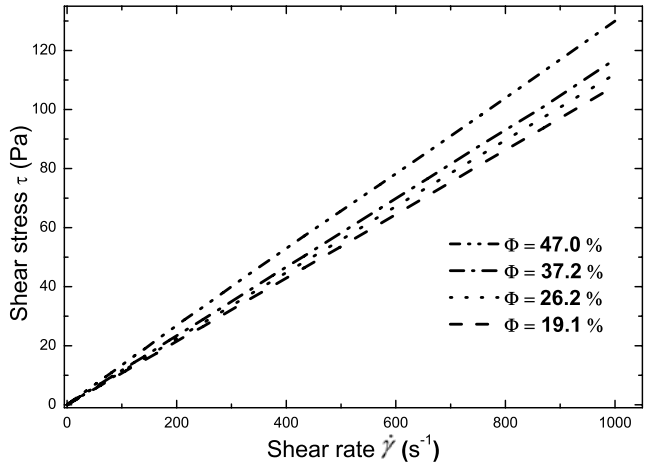

(a)

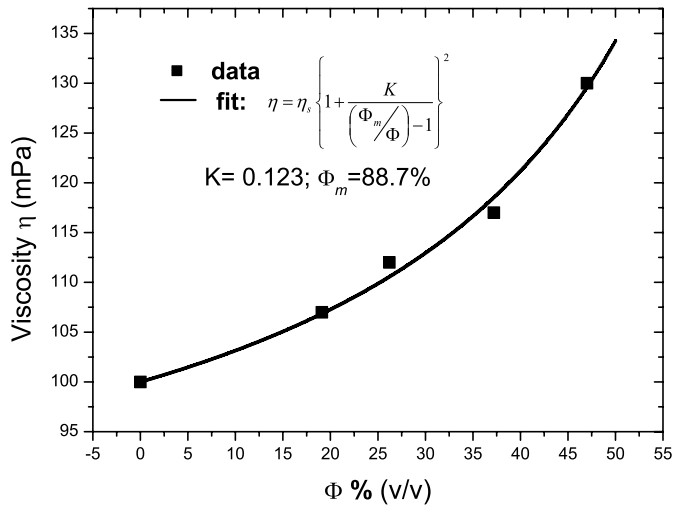

(b)

Figure 1:- (a) Flow curves of Na-FH suspensions of four different volume fraction (Φ) of particles, E ~ 0. **(b)** Viscosity vs. volume fraction curve of Na-FH suspension, E~0 including a best fit to equation (2) with K= 0.123 and Φ_m=88.7%.

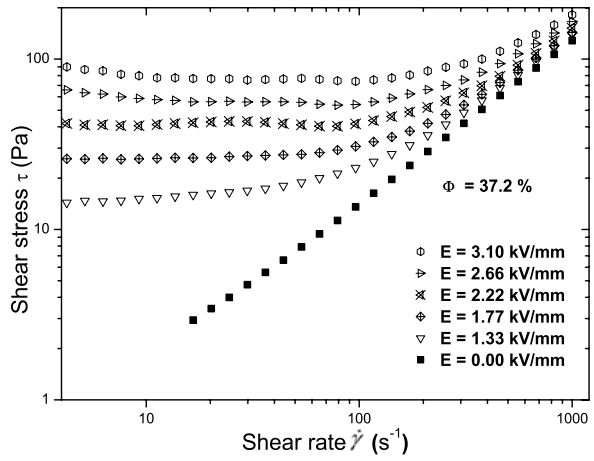

(a)

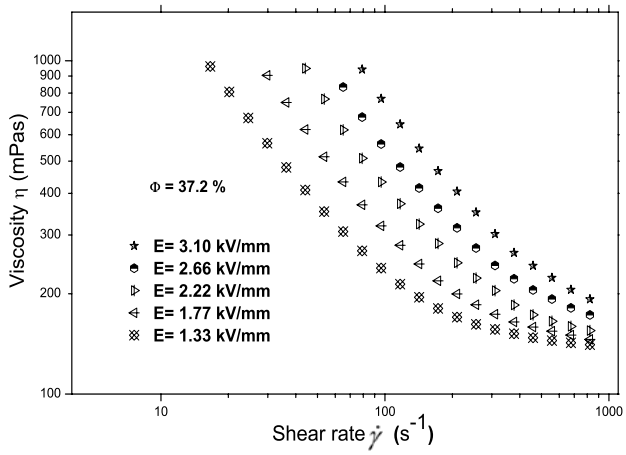

(b)

Figure 2: (a) Flow- curves of Na-FH suspensions for Φ = 37.2 at different applied electric fields The flow curves clearly show the yielding behavior of ER suspensions under application of an electric field. **(b)** Viscosity versus shear rate for the same suspension.

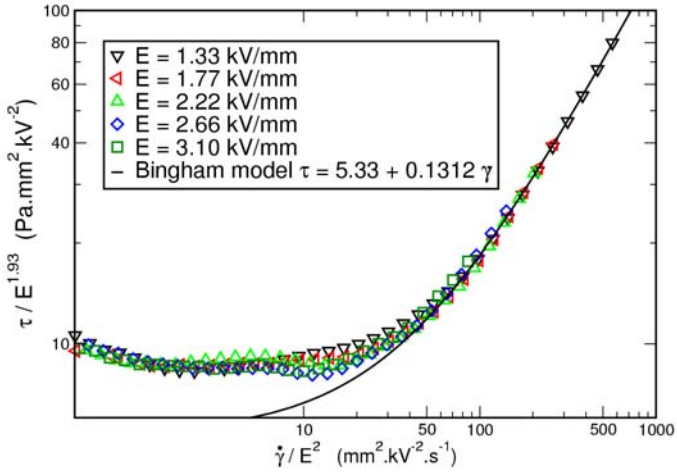

Figure 3: Scaling of the data of Figure 2(a) using equation (1) with α = 1.93, for a particle fraction Φ = 37.2%. The fully drawn line represents the Bingham model.

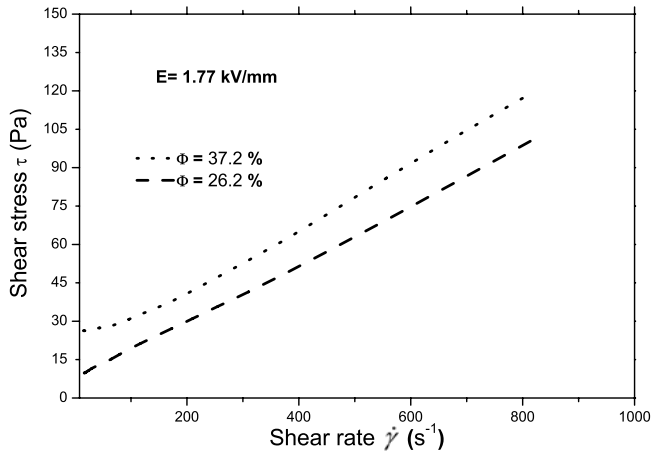

(a)

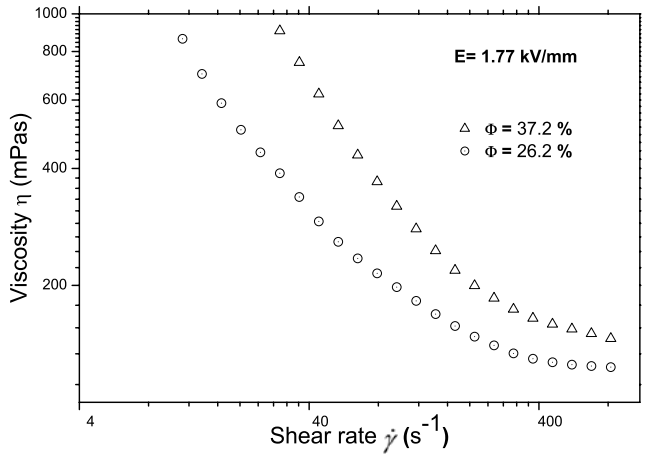

(b)

Figure 4:- (a) Flow- curves of Na-FH suspension for two different Φ-values at E~1.77 kV/mm. **(b)** Viscosity- curves for the same suspensions. The shear stress and viscosity increase with increasing Φ.

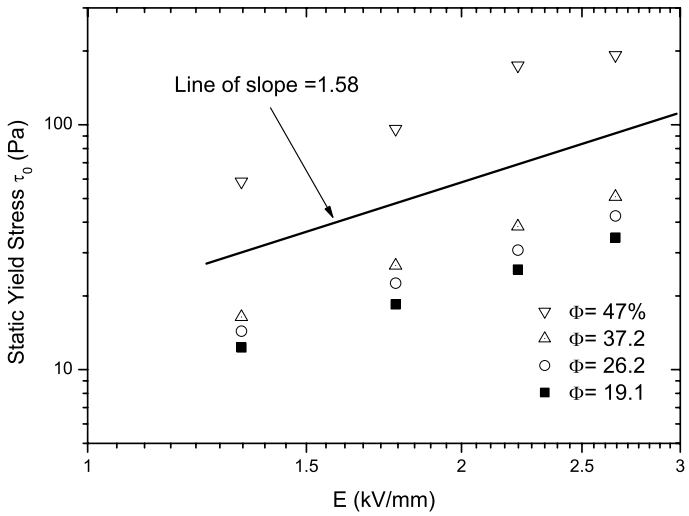

Figure 5: Log-log plot of the static yield stress plotted against the strength of the applied DC electric field for different volume fractions of Na-FH particles dispersed in silicone oil.

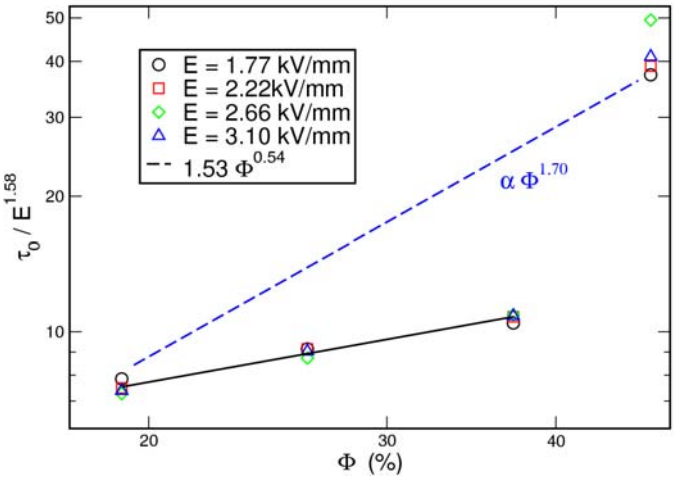

Figure 6: Scaled static yield stress versus particle concentration for the present Na-FH suspensions. The dashed line (slope equal to 1.70) represents the behavior of our previously-reported laponite suspensions [16].

Paper 6

Phase behavior of platelet-shaped nanosilicate colloids in saline solutions – a SAXS study

D. M. Fonseca,[a*] Y. Méheust,[a] J. O. Fossum,[a*] K. D. Knudsen,[b] K. J. Måløy[c] and K. P. S. Parmar[a]

[a]Physics Department, Norwegian University of Science and Technology (NTNU), Trondheim, Norway, [b]Physics Department, Institute for Energy Technology (IFE), Kjeller , Norway, and [c]Physics Department, University of Oslo (UiO), Oslo, Norway. E-mail: davi.fonseca@ntnu.no, jon.fossum@ntnu.no

Abstract A study of polydisperse suspensions of fluorohectorite clay in saline solutions is presented. The suspended clay colloids consist of stacks of several tenths of 1 nm-thick nanosilicate sheets. They are polydisperse both with respect to the number of stacked nanolayers and with respect to their extension along the sheets. Due to this polydispersity, a spontaneous gravity-induced vertical segregation occurs in the sample tubes, and results in the presence of up to four different phases on top of each other. Precise characterization of the phase diagram of the samples as a function of salt concentration and vertical position in the tubes, based on Small Angle X-ray Scattering data is presented. The vertical positions of the phase boundaries were monitored by analyzing the eccentricity of elliptic fits to iso-intensity cuts of the scattering images. The intensity profiles along the two principal directions of scattering display two power law behaviors with a smooth transition between them, and show the absence of positional order in all phases.

Synopsis Precise characterization of the phase diagram for suspensions of Na-Fluorohectorite colloids in saline solutions is achieved from SAXS measurements. Radial intensity profiles are also addressed.

Keywords: Platelet-shaped colloids; nematic ordering; phase diagram; SAXS

1. Introduction

Colloidal suspensions of 2:1 clay particles in aqueous salt solutions make ideal model systems for the study of interactions between platelet-shaped particles. Indeed, the particle-particle interaction consists of (i) the van der Waals attraction and (ii) the electrostatic repulsion between the particles' electric double layer (McBride & Baveye, 2002). The extension of the latter repulsion can be easily tuned by changing the electrolyte concentration (Israelachvili, 1992). This complex particle-particle interaction combined with the strong particle anisotropy results in rich phase behaviors. The phase diagram of the monodisperse synthetic 2:1 clay Laponite dispersed in saline solution, in particular, has been the subject of much attention (Mourchid *et al.*, 1998; Bonn *et al.*, 1999; Lemaire *et al.*, 2002). Such

dispersions are now well-known for the existence of a spontaneous nematic arrangement of the platelets at given salt- and particle-concentrations (Mourchid *et al*., 1998; Lemaire *et al*., 2002; van der Beek & Lekkerkerker, 2003).

Another synthetic clay, Na-fluorohectorite (NaFHT), has been found to exhibit interesting phase behavior when suspended in saline solutions. NaFHT presents polydispersity in both particle size and aspect ratio (Kaviratna *et al*., 1996). In the presence of polydispersity a spontaneous phase segregation occurs in the suspensions (Fossum, 1999; Bates, 1999; van der Kooij, 2001), with several phases co-existing in strata. X-ray Diffraction studies of such systems (DiMasi *et al.*, 2001) have investigated the clay particles' orientations in these NaFHT-NaCl-H_2O systems, taking advantage of their nano-layered nature. Three distinct gel regions were identified and characterized by differences in orientational order and/or the size of ordered domains. One phase was presented as nematic. Those findings are consistent with visual observations (Fossum *et al*., 2005), including observations through crossed polarizers: a birefringent region, coinciding with the region exhibiting orientational order (as inferred from the WAXS study), was observed.

However, the corresponding phase diagram has not yet been determined with precision, nor has the orientationally-ordered gel phase been fully characterized as nematic. In the present work, synchrotron Small Angle X-ray Scattering (SAXS) is used to obtain a fine characterization of the phase diagram, over a large NaCl concentration range. The experimental method is presented in section 2 and the data analysis and results in section 3; section 4 is the conclusion.

2. Experimental method

2.1. Samples

The samples consist of Na-Fluorohectorite (NaFHT) crystallites suspended in a saline solution. They were prepared in the following way: Li-Fluorohectorite clay was purchased in powder form from Corning Inc. (New York). It was cation-exchanged using NaCl, and then the extra Cl^- ions were removed through dialysis. After drying, the obtained clay crystallites have the nominal chemical formula $Na_{0.6}(Mg_{2.4}Li_{0.6})Si_4O_{10}F_2$.

Several suspensions of such crystallites were subsequently prepared, with a 3% concentration of clay (w/w), and NaCl concentrations ranging from 0.1 to 25 mM (Table 1). After addition of the clay powder to the saline solution, the suspensions were left shaking overnight; after twelve hours, they were poured into 2 mm diameter capillaries made of borosilicate glass. They were then allowed to settle for thirty days. After this time, one could observe up to four superimposed phases, as shown in Fig. 1: the phase at the very bottom is opaque; that on top of it is a translucent gel; the third phase observed from the bottom up is a transparent gel; the top phase is a transparent sol.

2.2. Scattering setup

Small Angle X-ray Scattering (SAXS) experiments were performed on the Dutch-Belgian Beamline (DUBBLE) at the European Synchrotron Radiation Facility (ESRF), in Grenoble (France). This beamline provides a focused,

monochromatic radiation with an energy tuneable in the range 5-30 keV, corresponding to wavelengths between 0.41 and 2.48 Å. A wavelength of 1.55 Å was chosen for this experiment.

The experimental hutch contains the SAXS camera with a maximal and minimal sample-to-detector distance of 8 and 1.4 m, respectively. The maximum camera length was picked so as to investigate length scales as large as possible. Two-dimensional SAXS images were recorded using a 2D multiwire gas-filled detector (Gabriel & Dauvergne, 1982). This detector has an image size of 133x133 mm^2 with a spatial resolution of 250±5 μm. Consequently, the q-range accessible in the experiment was 0.018-0.33 nm^{-1}, corresponding to length scales between 20 and 350 nm. The measurement setup also contains a linear WAXS detector based on a curved microstrip glass strip counter. This allowed to simultaneously record SAXS and WAXS data with a time resolution down to 1 msec/timeframe. The WAXS data will not be discussed in this paper.

In order to avoid repeatedly entering the experimental hutch to change samples, a sample holder containing ten capillaries placed side by side and regularly spaced was employed. The samples were placed in the beam in turn by translating the holder using a remotely-controlled horizontal translation stage. Another translation stage allowed controlling the vertical position of the sample with respect to the beam.

2.3. Experimental protocol

For each sample: (i) a vertical transmission scan was carried out and (ii) SAXS patterns at different heights were collected. Table 1 lists the details of vertical positions at which SAXS data was recorded for each sample. The liquid phase at the top of the sample tube was not investigated. All SAXS images were recorded with an exposure time of 60 seconds.

3. Data analysis

3.1. Method

Fig. 2 displays examples of SAXS images recorded from the lower and upper gel phases, for a salt concentration of 1 mM. The data in Fig. 2(*a*) is isotropic, while the one displayed in Fig. 2(*b*) is clearly anisotropic, indicating a preferential orientation of the clay crystallites.

Iso-intensity lines of the SAXS images are well described by ellipses. Hence, a custom-made MATLAB program was used to fit ellipses to such iso-intensity lines. Practically, the fitting procedure is accomplished in the following way. First, a narrow intensity range is selected (Fig. 3*a*), and then the pixels with an intensity that falls in that range are extracted from the 2D SAXS image. Subsequently an ellipse is fitted to the cloud of points defined by the horizontal and vertical coordinates of the selected pixels (Fig. 3*b*). This procedure provides the center of the ellipse, the length of its major axis, a, that of its semi-minor axis, b, and its angle of tilt with respect to the horizontal. From a and b one can calculate the eccentricity, e

$$e = \sqrt{1 - \frac{b^2}{a^2}} \, .$$

This procedure was tested at different intensity levels, and the fit results were shown to depend only weakly on the intensity range used to obtain them.

The obtained fit parameters can be related to the scattering process as follows: (i) the center of the ellipse is a fine estimate for the position of the direct beam; (ii) the principal axes of the ellipse are related to the orientational ordering of the scattering clay particles; (iii) the eccentricity of the ellipse is a measure of the image's anisotropy: an image with a perfect axial symmetry would yield a value e = 0, while a value closer to 1 denotes a very anisotropic image; and (iv) the angle of tilt of the ellipse is related to the preferential orientation of the scatterers with respect to the laboratory frame.

Finally, one-dimensional intensity profiles of scattered intensity versus q along the principal axes of the ellipses were computed. Those profiles were generated by integrating the 2D images over azimuthal angles in 5^o wide sectors around each of the principal directions. The resolution of those profiles along the radial direction was set to 250 radial bins.

3.2. Results

3.2.1. Phase diagram

The computed eccentricities were plotted as a function of the vertical position for each sample. From these plots (not shown here) it is readily noticeable that: (i) a region at the bottom part of the sample corresponds to eccentricities spread over a wide range of values, (ii) a region which only contains high eccentricities values is found on top of the latter one, and (iii) the third region from the bottom up contains only low eccentricities values. Note that the fourth (and top) phase observed visually in the highest part of the sample tube was not studied by SAXS, and will not be discussed in what follows. The three regions found from the SAXS data correspond to the three bottom phases observed visually. Since the anisotropy of the 2D scattering images is characteristic of particle orientational ordering, the phases were identified as the sediment, a gel phase with preferential particle ordering, and an isotropic gel, respectively.

From these plots for individual samples, a surface plot taking all samples into account was constructed. Since the concentrations used here form a non-regular and non-monotonic grid, MATLAB was used to interpolate the data on a regular grid. Fig. 4(*a*) shows a grayscale view of that surface plot, with salt concentration along the horizontal axis and vertical position along the vertical axis; grayscale intensities denote the eccentricity value at a given point of the parameter space. In this representation, sudden changes in the gray level denote possible phase boundaries. A dark gray zone at the top of the image obviously denotes the isotropic gel phase, since the scattering from that phase is isotropic. On the other hand, the images collected in the gel phase with a preferential orientation of the particles must correspond to high eccentricities, since the characteristic orientational ordering causes a very anisotropic scattering. Therefore, the white

zone on the left part of the image, under the region corresponding to the isotropic gel, corresponds to that anisotropic gel.

In order to complete our understanding of the phase boundaries as inferred from the SAXS data, a 2D grayscale image of the transmission data was also made (Fig. 4*b*). Owing to the relatively sharp change in transmission from the sediment to the gel phases, it is easy to identify the sediment. Note that the images of Figs. 4(*a*) and 4(*b*) complement each other; their joint interpretation allows clear definition of the phase boundaries for the sediment, anisotropic gel and isotropic gel. We are left with an unidentified region in the right part of the image, between the regions corresponding to the sediment and to the isotropic gel. That region exhibits moderate absorption, and moderate eccentricity values that vary on a small scale in the parameter space. It also exhibits all possible angles of tilt for the fitted ellipses (tilt angle data are not shown here).

Fig. 5 summarizes this phase diagram for the suspensions. When Fig. 5 is compared to the two previous estimates of the diagrams [one from visual observation, the other one from WAXS data, see DiMasi *et al*. (2001) and Fossum *et al*. (2005)], it is evident that the main features are consistent. The anisotropic gel found here is the nematic gel phase as identified from WAXS data. Fig. 2(*b*) is a typical SAXS image recorded from this phase; the orientation of the elliptic iso-intensity lines is consistent with the previous WAXS analyses, according to which the platelet-shaped clay particles are standing on average with their short dimension along the horizontal (DiMasi *et. al.*, 2001). The rightmost region in the diagram (Fig. 4*a*) corresponds to what DiMasi *et al*. (2001) denote as a small nematic domain phase (SD). We believe that this region contains in fact many small nematic regions. At the scale of the scattering volume, this results in SAXS data with a moderate anisotropy, the magnitude and preferential orientation of which are not fixed for the whole region.

Two discrepancies between the current phase diagram and the previous estimates can be spotted. One of them is that the phase boundaries are not exactly at the same vertical position. This is expected since the samples in the different experiments were allowed to settle for unequal times, and the phase boundaries are known to change position for several months before they stabilize. The other evident new observation compared to our previous studies concerns the boundary of the two gel phases at low salt concentrations. Its first two points in the previous estimates are much higher than what is observed here (around two times higher), with respect to the rest of that boundary. The behavior observed in the present experiment is systematic and is observed for five different concentrations here, whereas it was observed for only two concentrations in the other works. Currently, one may suggest several alternative explanations for this difference, and this will be subject for future work.

3.2.2. Spectra along the principal axes

For a given SAXS image, the scattered intensity as a function of the scattering vector q was also plotted along the two principal directions of the image, as determined by the fitting of ellipses to iso-intensity lines. Fig. 6 presents such q-

plots for a SAXS image in the isotropic phase and another one in the nematic phase of the sample with saline concentration of 1 mM.

The q-plots in Fig. 6 appear as consisting of several power law regimes. This is expected in SAXS data from systems of aggregated particles (Schmidt, 1991). On all plots, a smooth crossover is noticed. It corresponds to a characteristic length scale of approx. 150 nm, which possibly could be related to the average thickness of the stacks of clay platelets. This is the only characteristic length of the particles that can be probed in the q-range investigated with SAXS. It is smooth due to polydispersity in the particle thicknesses. Note that this characteristic length scale does not correspond to a regular periodicity in the meso-structure, since no peak is visible in the data at the corresponding q-value. Hence, none of the phases exhibits positional order at the length scales probed by the SAXS experiment. In particular, the lower gel phase is ordered with respect to particle orientations but not positions.

The values for the exponents of the power laws, as estimated from slopes in the log-log plots in Fig. 6 are presented in Table 2. We notice that at higher q-values, the slopes seem to approach -4, possibly indicating crossover into a regime of scattering from smooth surfaces (Porod regime) as the probed length scales become smaller than the typical particle size. We also notice that at lower q-values, the slopes approach -2. This is expected for mono-disperse platelets with no correlations between particle- positions and orientations, either (i) nematically-oriented, provided that q is pointing along the normal to the platelets, or (ii) randomly-oriented (Ramsay, 1990). For nematically-oriented mono-disperse platelets with no correlations between positions and orientations, a slope of -3 is expected when q points perpendicular to the short plate direction (Ramsay, 1990). Note that our observations in terms of power-law exponents may be influenced by the fact that our platelets are not mono-disperse, and that positions and orientations of particles may be correlated.

4. Conclusion

SAXS experiments have allowed a precise characterization of the phase diagram of suspensions of Na-fluorohectorite platelet-shaped particles in saline solutions. The characterization was done based on transmission data, and on two-dimensional SAXS images.

Ellipses were fitted to iso-intensity lines of the SAXS images. The phase boundaries were obtained through joint analysis of the transmission data and of results for the ellipses' eccentricities and tilt angles. Among the different phases observed, one is a gel phase exhibiting a high degree of orientational order, while the other one is an isotropic gel. This phase diagram is consistent with our previous estimates using other approaches. Moreover, plots of the integrated intensities versus the scattering vector along the principal axes of the ellipses for both gel phases exhibit power law behaviors with a smooth crossover at a length scale corresponding to the mean particle thickness, and exponents that approach those of well-known configurations at the lower and higher q-values. These q-plots confirm that no positional order exists in any of the phases.

X-ray Scattering techniques have proved to be a technique appropriate for discriminating between different phases in these samples. A prospect of the study

concerns further understanding of the differences between the different phases, in terms of the geometry of the porous space between the particles (Knudsen *et al*., 2004), focusing on the power law behavior of q-plots. The ultimate goal is to understand the underlying mechanisms responsible for the formation of the different phases.

Acknowledgements The authors acknowledge the European Synchrotron Radiation Facility for provision of synchrotron radiation facilities and we would like to thank Dr. Igor Dolbnya for assistance in using beamline BM26B. This work has received partial financial support from the Research Council of Norway (RCN) through the NANOMAT Program: RCN project numbers 152426/431, 154059/420 and 148865/432, as well as through 138368/V30 and SUP154059/420.

References

Bates, M. A. (1999). *J. Chem. Phys.* **111**, 1732-1736.
Bonn, D., Tanaka, H., Kellay, H., Wegdam, G. & Meunier, J. (1999). *Langmuir* **15**, 7534-7536.
DiMasi, E., Fossum, J. O., Gog, T. & Venkataraman, C. (2001). *Phys. Rev. E* **64**, 61704.
Fossum, J. O. (1999). *Physica A* **270**, 270-277.
Fossum, J. O., Gudding, E., Fonseca, D. d. M., Méheust, Y., DiMasi, E., Gog, T. & Venkataraman, C. (2005). *Energy* **30**, 873-883.
Gabriel, A. & Dauvergne, F. (1982). *Nucl. Instr. and Meth.* **201**, 223-230.
Israelachvili, J. (1992) *Intermolecular and Surface Forces*. London: Academic Press.
Kaviratna, P. D., Pinnavaia, T. J. & Schroeder, P. A. (1996). *J. Phys. Chem. Solids* **57**, 1897-1906.
Knudsen, K. D., Fossum, J. O., Helgesen, G. & Haakestad, M. W. (2004). *Physica B* **352**, 247–258.
Lemaire, B. J., Panine, P., Gabriel J. C. P. & Davidson, P. (2002). *Europhys. Lett.* **59**, 55-61.
McBride, M. B. & Baveye, P. (2002). *Soil Sci. Soc. Am. J.* **66**, 1207-1217.
Mourchid, A., Lecolier, E., van Damme, H. & Levitz, P. (1998). *Langmuir* **14**, 4718-4723.
Ramsay, J. D. F. (1990). *J. Chem. Soc. Faraday* **86**, 3919-3926.
Schmidt, P. W. (1991). *J. Appl. Cryst.* **24**, 414-435.
van der Beek, D. & Lekkerkerker, H. N. W. (2003). *Europhys. Lett.* **61**, 702-707.
Van der Kooij, F. M., van der Beek, D. & Lekkerkerker, H. N. W. (2001). *J. Phys. Chem. B* **105**, 1696-1700.

Figure 1 Na-Fluorohectorite sample with a particle concentration of 3 % (w/w) and a salt (NaCl) concentration of 4.5 mM. The 4 four phases are easily identifiable.

Figure 2 SAXS images recorded in the upper (*a*) and lower (*b*) gel phases. The anisotropic image in (*b*) indicates a preferential orientation of the clay crystallites in the lower phase.

Figure 3 (*a*) The 3D scattering profile. The arrow indicates a range that could be used to generate the cloud of points. (*b*) The blue circles represent the cloud of points inside the range of the scattering profile. The green ellipse is the initial guess for the fitting procedure. The red ellipse is the evaluated best fit to the cloud of points.

Figure 4 (*a*) Greyscale map for the eccentricity values computed from the SAXS data, as a function of the salt concentration and vertical position in the sample tubes. (*b*) Idem, but computed from the transmission data.

Figure 5 Phase diagram created from the greyscale maps for eccentricity and transmission. The displayed regions are sediment (S), nematic gel (NG), isotropic gel (IG), and region containing small domains (SD).

Figure 6 Integrated intensities plots along the principal axes of the ellipse for both a point in the isotropic phase and also for a point in the nematic phase. The smooth crossover is positioned at a length scale corresponding to the mean particle thickness.

Table 1 Vertical positions at which SAXS data was recorded, for each sample.

Table 2 Power law exponents determined from Fig. 6.

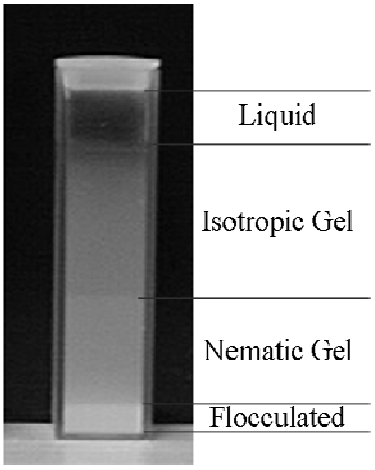

Figure 1.

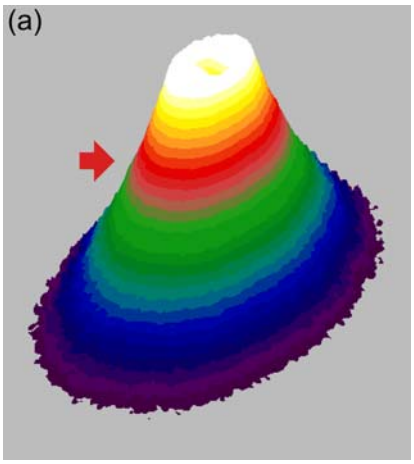

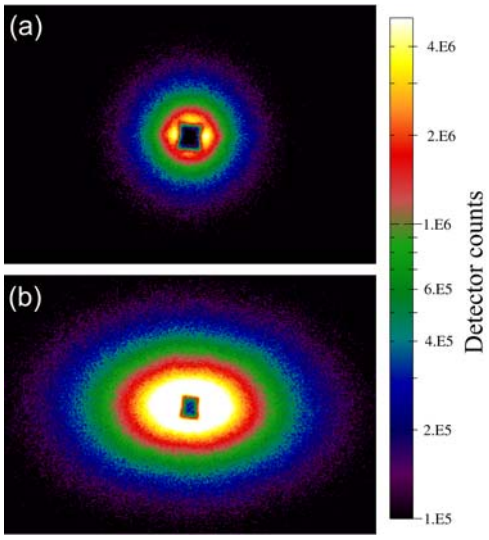

Figure 2.

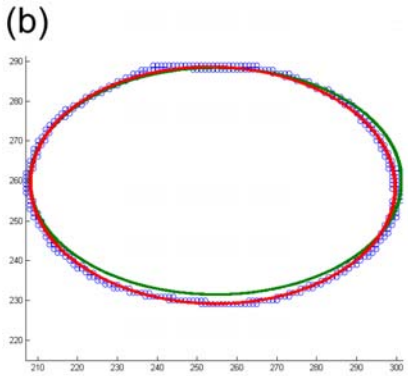

Figure 3.

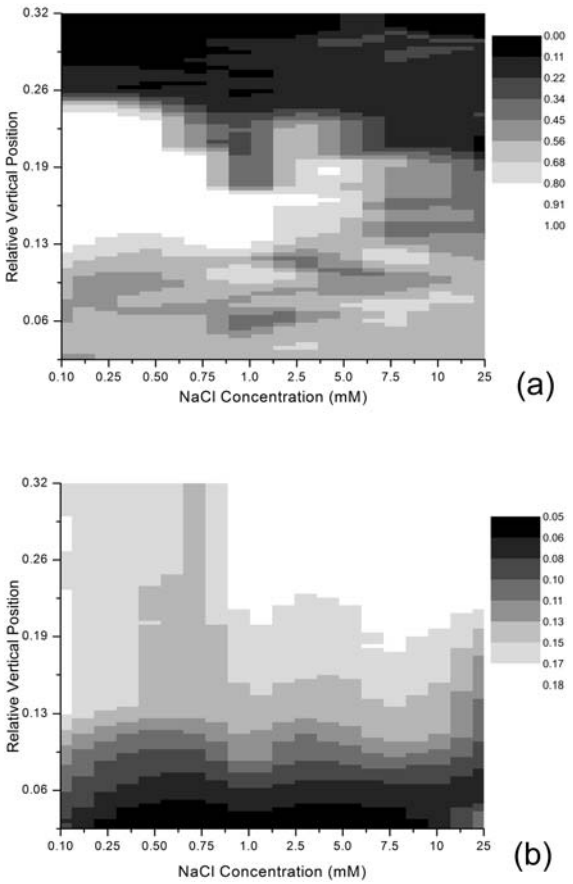

Figure 4.

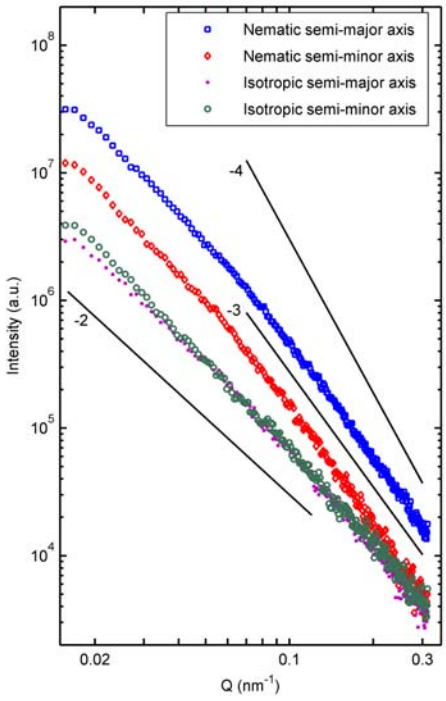

Figure 6.

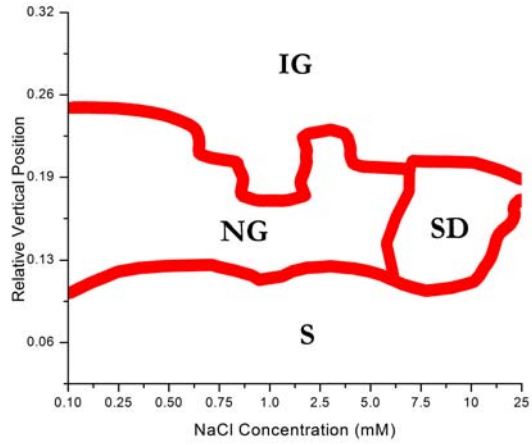

Figure 5.

Sample Concentration (mM)	Starting position[a] (mm)	Step size (mm)	Number Of steps
0.1	0	1	14
0.25	0	1	22
0.5	0	1	22
0.75	0	0.5	44
1.0	0	0.5	44
2.5	1	0.5	44
5.0	1	0.5	44
7.5	1	0.5	44
10	1	0.5	44
25	1	0.5	54

[a] – above the bottom of the sample

Table 1.

	Slope left of crossover	Slope right of crossover
Nematic along semi-major axis	–2.16 ± 0.16	–2.84 ± 0.07
Nematic along semi-minor axis	–2.34 ± 0.05	–2.90 ± 0.04
Isotropic along semi-major axis	–2.19 ± 0.08	–2.43 ± 0.04
Isotropic along semi-major axis	–2.45 ± 0.14	–2.41 ± 0.17

Table 2.